# Primary Drainage Capillary Pressure Curves in Heterogeneous Carbonates with Ultracentrifuge and NMR

**By**
**Karl-Erik Holm Sylta**


**Master's Thesis in**
**Petroleum Technology - Reservoir Physics**

**Centre for Integrated Petroleum Research**

**Department of Physics and Technology**

**University of Bergen**

**2010**

uniCIPR

# Abstract

Capillary pressure is one of the most fundamental rock-fluid characteristics in multi-phase flow, critically influencing both the initial reservoir fluid distribution and the dynamic processes of oil recovery. Thus, it is of great importance to obtain accurate capillary pressure-saturation relationships when examining reservoir rocks. This work investigates a new method for obtaining the primary drainage capillary pressure curve for heterogeneous carbonates in air-brine and oil-brine systems. The method uses an ultracentrifuge to create a distribution of fluids and capillary pressures in a rock core before a NMR method is used to measure the saturation profile within the rock. In order to widen the application of the method, a diffusion-weighted profile sequence is used for NMR measurements in oil-brine systems. The method is able to provide a primary drainage capillary pressure curve in 3 days, and is therefore considered as a rapid alternative to other methods.

By comparing results obtained for a relatively homogeneous Berea sandstone with that of more heterogeneous carbonate samples, the effects of heterogeneity are evident. The complexity of the studied material is reflected in the resulting capillary pressure curves, illustrating how heterogeneities violate classical concepts and assumptions within core analysis. However, these effects can provide valuable additional information for further studies. In particular, in-depth studies of a highly complex vuggy carbonate material questions the validity of assumptions made in numerous studies. It is also suggested that a capillary pressure curve representing the matrix porosity of the vuggy carbonate is obtainable. Since it is able to measure the actual fluid saturations within the rocks, NMR is proved to be a valuable tool for core analysis in heterogeneous material, visualizing both internal structures and their specific properties.

In an attempt to verify the current method, several uncertainties concerning the procedures are addressed, including the prospects of fluid evaporation and redistribution. Studies indicate that fluid evaporation can be neglected within the time needed to perform the measurements with the new method. The rate of fluid redistribution is decreasing with permeability and the type of fluids present. Thus, it does occur to some extent in air-brine measurements, but can be neglected for the oil-brine measurements in the low permeable limestones. Due to its low uncertainties, the investigated method is considered to be a very accurate and reliable technique.

# Acknowledgements

I would like to especially acknowledge my main supervisor, Associate Professor Jan R. Lien and my co-advisor Dr. Ketil Djurhuus for their invaluable assistance and feedback during the experimental work and the writing process.

Special thanks also go to Professor Arne Skauge, Tina Pavlin, Sverre Hetland, Bartek Vik and Geir H. Sørland and for their excellent assistance and support throughout the process. I also want to acknowledge Edin Alagic and Jonas Solbakken for their contributions along the way.

All experiments in this thesis were performed at the Centre for Integrated Petroleum Research (CIPR) at the University of Bergen. I would like to thank CIPR as an organisation for giving me general assistance. I am also thankful to Terje Finnekås for all his help as a student advisor during these years at UiB.

Finally, I have to thank my family, Elisabeth and all my friends that made my 5 years at UiB into a memorable experience. In particular, Steffen Barka deserves recognition for his cooperation skills and cheerful mood.

Karl-Erik Holm Sylta,
Bergen, May 2010

# Nomenclature

| | |
|---|---|
| $A$ | Cross-sectional area |
| *AH* | Amott-Harvey |
| $\mathbf{B}_0$ | Static magnetic field |
| $\mathbf{B}_1$ | Oscillating magnetic field (RF-field) |
| *BVI* | Bound volume irreducible |
| *BVM* | Bulk volume movable |
| *BVW* | Bulk volume water |
| *CBW* | Clay bound water |
| *CPMG* | Carr, Purcell, Meiboom, Gill |
| $\chi$ | Magnetic susceptibility |
| $D$ | Diffusion coefficient |
| $d$ | Diameter |
| $\delta$ | Surface layer in a pore volume |
| $\delta$ | Gradient length |
| *EOR* | Enhanced oil recovery |
| *FID* | Free induction decay |
| *FW* | Fractionally wet |
| *FWL* | Free water level |
| $f_L$ | Larmor frequency |
| $\varphi$ | Porosity |
| $\varphi_{eff}$ | Effective porosity |
| $\varphi_{res}$ | Residual porosity |
| $G$ | Gradient strength input value |
| $\mathbf{G}_{\mathbf{read}}$ | Readout gradient |
| $g$ | Gravity |
| $\mathbf{g}$ | Applied gradient strength |
| $\gamma$ | Gyromagnetic ratio |
| $h$ | Height |
| *HC* | Hydrocarbon |
| *IFT* | Interfacial tension |
| $I_{AH}$ | Amott-Harvey index |

| | |
|---|---|
| $I_{USBM}$ | USBM-index |
| $\mathbf{J}$ | Angular momentum |
| $K$ | Absolute permeability |
| $L$ | Core length |
| $L1$ | Limestone plug 1 |
| $L2$ | Limestone plug 2 |
| $\mathbf{M}$ | Magnetization |
| $M_0$ | Intensity measurement at 100% water saturation |
| $M_a$ | Intensity measurement after centrifugation |
| $MW$ | Mixed wet |
| $MWL$ | Mixed wet large |
| $MWS$ | Mixed wet small |
| $m$ | Mass |
| $m_z$ | Magnetic quantum number |
| $\mu$ | Viscosity |
| $\boldsymbol{\mu}$ | Magnetic moment |
| $N$ | Number of measurements |
| $NMR$ | Nuclear magnetic resonance |
| $OWC$ | Oil water contact |
| $\omega$ | Angular velocity |
| $P$ | Pressure |
| $P_c$ | Capillary pressure |
| $PFGSE$ | Pulsed field gradient spin echo |
| $PV$ | Pore volume |
| $Q$ | Volume flow |
| $R$ | Radius |
| $r$ | Radius |
| $RF$ | Radio frequency |
| $rpm$ | Revolutions per minute |
| $\rho$ | Density |
| $S$ | Signal strength |
| $S_g$ | Gas saturation |
| $S_o$ | Oil saturation |
| $S_{or}$ | Residual oil saturation |

| | |
|---|---|
| $S_w$ | Water saturation |
| $S_{wi}$ | Irreducible water saturation |
| $SD$ | Standard deviation |
| $SNR$ | Signal to noise ratio |
| $\sigma$ | Interfacial tension |
| $T_1$ | Longitudinal relaxation time |
| $T_2$ | Transversal relaxation time |
| $T_{2co}$ | $T_2$ cut-off value |
| $\tau$ | Echo spacing |
| $\boldsymbol{\tau}$ | Torque |
| $\theta$ | Wetting angle |
| $U$ | Potential energy |
| $USBM$ | United States Bureau of Mines |
| $V_p$ | Pore volume |
| $V_t$ | Total volume |
| $VC$ | Vuggy carbonate plug |
| $VC2$ | Vuggy carbonate plug 2 |
| $\Delta x$ | Resolution of x-axis |

# Table of contents

# 1 Introduction

Recently, research into Enhanced Oil Recovery (EOR) has returned to the top of the agenda for most large international oil and gas companies. A vital part of this research is to provide quality data for reservoir studies. Creating ever-more accurate reservoir models based on heterogeneous material is one of the main challenges for the future in the oil industry. Hence, simulations and models rapidly evolve in the direction of more details and greater precision, and the underlying petrophysical data should evolve accordingly. Many different measurements are needed to build-up a picture of the petrophysical properties and producibility of a reservoir rock. One factor that critically influences the initial fluid distribution and the processes of oil recovery is the capillary pressure. Capillary pressure is defined as the difference in pressure across the interface between two immiscible fluids. In evaluating hydrocarbon reservoirs, laboratory capillary pressure curve measurements on rock cores are directly applied to determine many basic petrophysical properties, e.g. pore size distributions, irreducible water saturation, residual oil saturation and wettability. Due to its importance, numerous techniques to obtain the capillary pressure-saturation relationship have been suggested over the years. Three techniques are widely accepted in the industry today, namely the mercury injection method [1], the porous plate method [2] and the centrifuge method [3]. The latter creates the basis of the technique investigated in this thesis.

Since nuclear magnetic resonance (NMR) was first introduced as a measurement technique more than 50 years ago, it has received increasing interest from the petroleum industry. Low field NMR is a rapid, non-destructive measurement technique based on the behaviour of nuclei in the vicinity of magnetic fields. By sampling of the full length of the rock it can provide a wealth of information about the fluids in oil- and water-saturated cores.

In the 1980's, constructing facies models became the principal method for characterizing carbonate reservoirs. However, these simple petrophysical models turned out to be insufficient to describe production from these rock formations. To improve this, reservoir engineers saw the necessity of implementing heterogeneity into the models. Today, there still are significant challenges in terms of recovery due to the highly complex internal structure and specificity of carbonate reservoirs. In the past, core analysis has mainly been focused on more homogeneous material. Now, as the demand for more accurate data arises, the importance of understanding more heterogeneous materials is recognized. The heterogeneity

of rocks often violates the fundamental assumptions behind classical concepts of fluid flow in porous media and causes the petrophysical properties to vary within a sample. This complicates both the acquisition and evaluation of data in heterogeneous core samples. Nevertheless, the fact that carbonate reservoirs hold 60 % of the world's oil and 40 % of the world's gas demonstrate the importance of thorough examination of carbonate materials [4].

This thesis investigates a new method for obtaining the primary drainage capillary pressure curve in heterogeneous carbonates. Studies by Baldwin et al. [5] in 1991 reported that it was possible to combine the well-known subjects of centrifuge experiments and NMR in order to obtain the capillary pressure-saturation relationship. The technique has recently been confirmed and further investigated by several studies [6-9]. A core plug is spun in a centrifuge at different rotational speeds to create a distribution of fluids and capillary pressures. In between each speed increment, the fluid saturations within the core plug are measured with various NMR sequences. The resulting capillary pressure curves are found by utilizing equations well-established in the literature.

The objective of this thesis work is to establish experimental procedures and to verify the application of the new method in both air-brine and oil-brine systems. It is desirable to provide accurate and valuable information applicable for further reservoir studies. The work presented stands out from previous studies in that it is conducted on heterogeneous carbonate materials, introducing several experimental challenges. In order to expose these challenges, a homogeneous sandstone sample is used as a reference throughout all measurements. As opposed to techniques applied in earlier studies, a diffusion-weighted NMR sequence is used to discriminate fluid signals in oil-brine systems. The basic theory behind the current method is discussed in the following chapters.

# 2 Basic petrophysical properties

## *2.1 Porosity, φ*

The *porosity* of a rock is defined as the void part of the total volume of the rock [10]. The void part is found in between grains in a sedimentary rock and it is in these pores liquids like water and oil will accumulate. Thus, the porosity is a measure of the fluid storage capacity of a rock. It will vary as a function of grain size, shape and distribution. *Absolute porosity* is defined as the ratio of pore volume $V_p$ and total volume $V_t$ of the rock or the sum of the *effective* and the *residual porosity*.

$$\varphi = \frac{V_p}{V_t} \times 100\% = \varphi_{eff} + \varphi_{res} \tag{2.1}$$

In order to produce hydrocarbons from a reservoir rock, some pores in the rock must be connected so that fluid flow can be maintained. The effective porosity $\varphi_{eff}$ is defined as the ratio of the total volume of these interconnected pores $V_{pi}$ to the bulk volume of the rock $V_t$. The residual porosity $\varphi_{res}$ represents those pores that are not connected. Since our interest is to produce hydrocarbons, it is obvious that the effective porosity is the parameter of primary interest in reservoir engineering. Hence we define:

$$\varphi_{eff} = \frac{V_{pi}}{V_t} \times 100\% \tag{2.2}$$

Two main types of pore can be defined according to their time of formation [11]. *Primary pores* are those formed when sediments are deposited, while *secondary pores* are developed in a rock some time after deposition. Secondary porosity is often caused by solution or cementation during diagenesis.

## *2.2 Permeability, K*

The *permeability* of a porous medium is the medium's capability to transmit fluids through its network of interconnected pores [10]. Since permeability is related to porosity, all factors controlling the latter will also affect the former. The permeability is a constant property of a

porous medium only if there is a single fluid flowing through the medium. In that case, the absolute permeability $K$ is described in the Darcy equation

$$Q = \frac{KA}{\mu}\left(\frac{\Delta P}{\Delta L}\right) \tag{2.3}$$

where $\mu$ is the viscosity of the flowing fluid, $Q$ is the volume flow through a porous medium core and $\Delta P$ is the pressure drop across the core. $A$ is the cross-sectional area of a core with length $L$.

If there is more than one fluid flowing in the porous medium, one fluid will obstruct the free flow of the other fluid. As a result of this, the medium will have an *effective permeability* for each of the fluids. The effective permeability depends on fluid saturation, pore size and pore throat size distribution, wettability and the wettability history of the rock. For a multiphase flow, the Darcy equation can be defined for each of the flowing fluids (e.g. water, oil and gas).

$$q_i = \frac{K_i A}{\mu_i}\frac{dp_i}{dx} \tag{2.4}$$

The unit of permeability is called darcy (D), which is 0.987 x $10^{-12}$ $m^2$, but millidarcy (mD) is commonly used when discussing permeability in reservoir rocks. Rocks can have a wide spectrum of permeabilities, ranging from 0.1 mD to more than 30 D.

## *2.3 Wettability*

When two immiscible fluids coexist near a surface, a cohesive force will arise between the fluid molecules and the molecules in the surface [12]. The fluid with the strongest force is the *wetting fluid*, while the other fluid is the *non-wetting fluid*. The wetting fluid will spread onto the surface. The different forms of wettability are described by the wetting angle $\theta$, the contact angle between the solid surface and the fluids in a system.

$\theta = 0 – 30^o$: Strongly water-wet

$\theta = 30 – 90^o$: Preferential water-wet

$\theta = 90^o$: Neutral

$\theta$ = 90 – 150$^o$: Preferential oil-wet

$\theta$ = 150 – 180$^o$: Strongly oil-wet

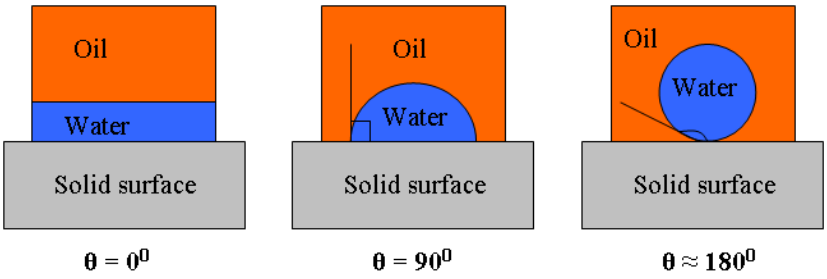


**Figure 2.1** *The relation between wetting angle and wettability[12].*

Most oil reservoirs are water-wet, meaning that water will be situated at the pore walls while the oil is in the middle of the pore. It is important to note that reservoir rocks are rarely strongly water-wet or strongly oil-wet and that the wettability can vary within a rock. A porous media can also be of *mixed wet (MW)* or *fractionally wet (FW)* nature. MW rocks can be divided into two subdivisions: Mixed wet large (MWL) and mixed wet small (MWS) where respectively the large pores and the small pores are oil-wet. Rocks with a FW nature have no correlation between pore size and wettability; both small and large pores can be oil-wet.

## *2.4 Saturation*

A porous medium normally contain more than one fluid phase, e.g. water, oil and gas. *Saturation* is the part of the total pore volume $V_p$ containing the fluid in question.

- Water saturation: $$S_w = \frac{V_w}{V_p} \quad (2.5)$$

- Oil saturation: $$S_o = \frac{V_o}{V_p} \quad (2.6)$$

- Gas saturation: $$S_g = \frac{V_g}{V_p} \quad (2.7)$$

As a general rule, the whole pore volume is filled by one of the fluids. Therefore

$$S_w + S_o + S_g = 1 \tag{2.8}$$

The irreducible water saturation $S_{wi}$ is an important property within the concept of oil recovery. This is the lowest value of water saturation obtainable in the reservoir, since water is trapped in small pores due to capillary forces.

Imagine an oil production scenario where water is injected to produce more oil from a water-wet rock. It will not be possible to obtain a recovery factor of 100%. The residual oil saturation $S_{or}$ is the lowest possible oil saturation in a reservoir. At this value, the oil is unable to flow and cannot be produced. The mechanisms for residual oil saturation may be illustrated through two simplified models shown in Figure 2.2. In the *pore doublet* model, oil is trapped by bypassing water in a pore doublet. The *snap-off* model illustrates a scenario where the oil phase snaps off into globules that are localized in the pore bodies of the flow path. Most of the residual oil in a water-wet media is considered to be trapped according to the snap-off model [13].

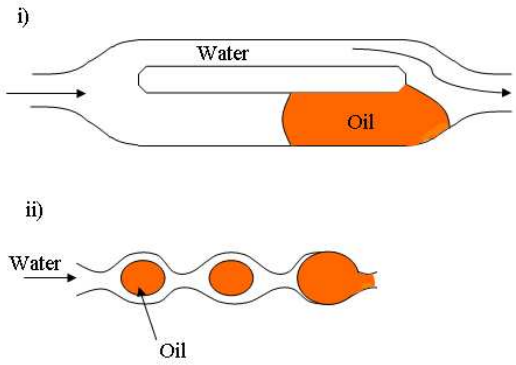


**Figure 2.2** *Trapping of oil in i) a pore doublet model and ii) a snap-off model*

## *2.5 Capillary pressure, $P_c$*

*Capillary pressure* critically influences the initial reservoir fluid distribution and the processes of oil recovery. It results from the interaction between a wetting fluid and a non-wetting fluid and is defined as the difference in pressure across the interface between the two immiscible fluids [12]. Laboratory experiments have shown that the capillary pressure $P_c$ depends upon interfacial tensions, wetting angles, porosity, permeability and fluid saturations.

Capillary pressure can be illustrated by imagining a thin capillary tube with radius $R$ in a vessel containing oil and water. Figure 2.3 illustrates the interaction between the fluids when the tubes are i) water-wet and ii) oil-wet. As mentioned earlier, the wetting fluid spreads onto the surface and so is the case for the surface of the capillary tube. If the glass of the vertical tube is water-wet, the water will displace the oil in the tube to some height until equilibrium is reached between the pressure difference and the fluid gravity. In the oil-wet case, the process is reversed, i.e. the oil drags itself down into the water phase. This illustrates the capillary pressure effect. The curved interface between the two fluids is called a meniscus, and it will always be convex towards the wetting fluid.

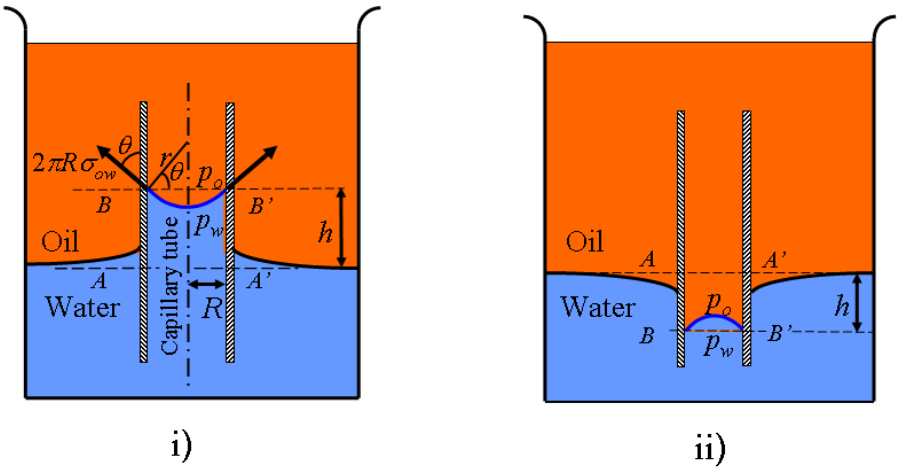


**Figure 2.3** *A capillary tube is placed in a vessel filled with oil and water. i) The glass of the tube is water-wet. ii) The glass is oil-wet [12].*

The interfacial tension (IFT) $\sigma$ is described as force per unit of length along the interface between the two fluids [12]. This force is perpendicular to the interface as shown in Figure 2.3 and its vertical component is

$$F_{ow} = 2\pi R\sigma_{ow}\cos\theta \tag{2.9}$$

$\theta$ is defined in Figure 2.3 and is previously described as the wetting angle in Chapter 2.3.

There is another force working downwards from the meniscus due to the pressure difference in water and oil. By examining the small surface area $dA$ and its downward working force $d\boldsymbol{F}_c$ in Figure 2.4 it is possible to obtain an expression for capillary pressure. The vertical component of this force is

$$dF_c = (p_o - p_w)dA\cos\alpha \tag{2.10}$$

$\alpha$ is defined in Figure 2.4. $dA_\perp$ is the size of the horizontal projection of $dA$ and it is given by $dA \cdot cos\alpha$. In order to find the total vertical component of the force it is necessary to integrate across the meniscus surface $A$.

$$F_c = (p_o - p_w)\int_A \cos\alpha dA = (p_o - p_w)\int_A dA_\perp = (p_o - p_w)\pi R^2 \tag{2.11}$$

When the meniscus has stabilized, the fluids are in static equilibrium. This condition implies that $F_c = F_{ow}$. Hence, Equation (2.9) and (2.11) can be written:

$$(p_o - p_w)\pi R^2 = 2\pi R\sigma_{ow}\cos\theta \tag{2.12}$$

This gives an expression for the capillary pressure $P_c$, the pressure difference in a non-wetting and a wetting fluid.

$$P_c = P_{non-wetting} - P_{wetting} = \frac{2\sigma\cos\theta}{R} = \Delta\rho gh \tag{2.13}$$

$\Delta\rho$ is defined as the density difference between the two fluids; $\Delta\rho = \rho_{wetting} - \rho_{non\text{-}wetting}$.

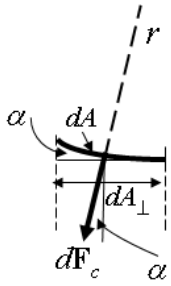


**Figure 2.4** *A small surface area dA of the meniscus [12].*

A porous media consists of a very complex network of pores, each with a representative capillary pressure. In order to show a relation between the capillary tube and a porous media, the vessel filled with water and oil in Figure 2.5 is considered. The oil will place itself on top of the water due to the difference in density. A collection of capillary tubes with varying radii $R$ are placed in the vessel. Due to the water-wet nature of the tubes, the water will rise to a height $h$ which is in inverse ratio to the radius $R$ of the tube. As seen in the figure below and

in Equation (2.13), the greatest elevation of the water is found in the tube with the smallest radius, while lower elevations are found as $R$ increases.

From these observations the *capillary pressure curve*, shown in Figure 2.5ii, can be constructed. This is a plot of capillary pressure ($P_c$) vs. water saturation ($S_w$). It is based on the assumptions that $S_w$ is proportional to the tube radius $R$ and the height $h$ is proportional to $P_c$. Hence, a relationship between the different parameters can be seen by comparing the two sketches in Figure 2.5. $P_c$ is largest in the tubes with the smallest $R$. These tubes also hold the lowest water saturation.

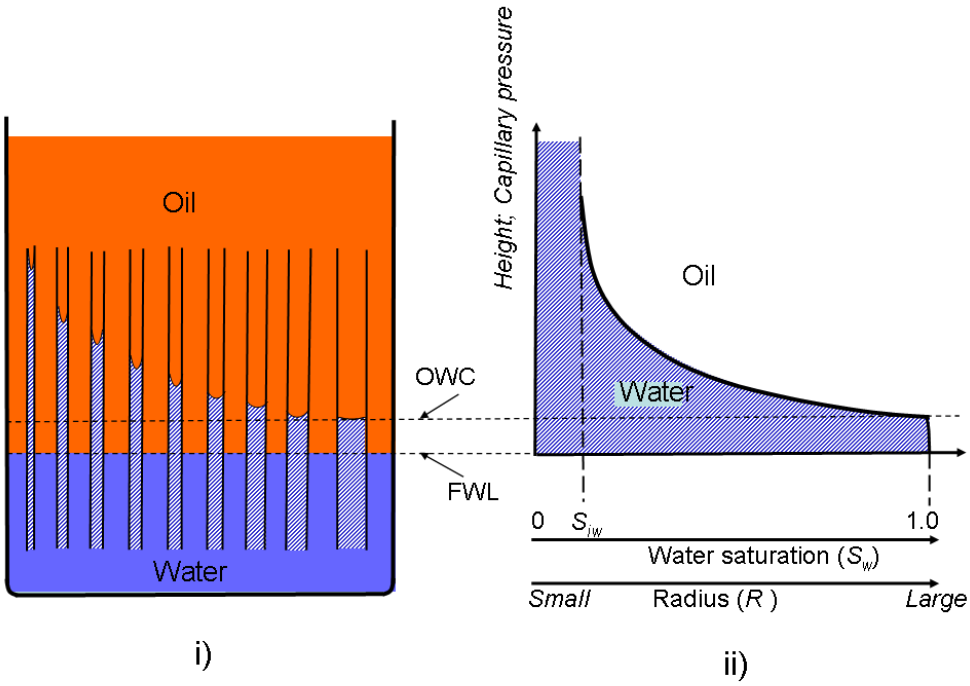


**Figure 2.5** *The relationship between capillary pressure, reservoir height, water saturation and radius illustrated by i) capillary tubes in water and ii) a primary drainage capillary pressure curve [12].*

Like the vessel with capillary tubes, a porous medium is a capillary system. Thus, the observations made for the vessel also holds in a reservoir rock. A large tube radius corresponds to a large pore throat radius. In order to fill the biggest pores in a porous rock with water, the pressure needs to reach a threshold pressure. To fill the smaller pores, the pressure must be increased even further. As you move upwards in a reservoir, the water filled

pores get smaller and smaller. Below the *free water level (FWL)* only water is present and the capillary pressure is zero.

The capillary pressure curve in Figure 2.5 represents a primary drainage process. A drainage process is when the saturation of the non-wetting fluid is increasing, while the saturation of the wetting fluid is decreasing [10]. If a wetting fluid is displacing a non-wetting fluid, it is an imbibition process. In this particular drainage example, the oil is displacing the water. Thus, the oil saturation ($S_o$) is increasing, while the water saturation ($S_w$) is decreasing towards the irreducible water saturation ($S_{wi}$). At this stage, water is trapped and kept stationary by the capillary forces of the small pores.

The displacing process mentioned above can illustrate what happens in a real large-scale reservoir. Initially, a reservoir rock is water-wet and filled with water, $S_w = 1$. Depending on the geological setting, hydrocarbons can migrate into the reservoir rock from a source rock. Oil droplets amalgamate with each other into progressively longer filaments, until their increased buoyancy allows them to overcome the threshold pressure and displace the water. Because of the water-wet nature of the reservoir rocks the capillary pressure will inhibit water displacement in the small pores. The oil will displace the water in the large pores first in a primary drainage process and eventually move to the top of the reservoir.

In order to find out more about a rock's wettability, the capillary pressure curves in Figure 2.6 and their associated displacing processes may be studied more closely.

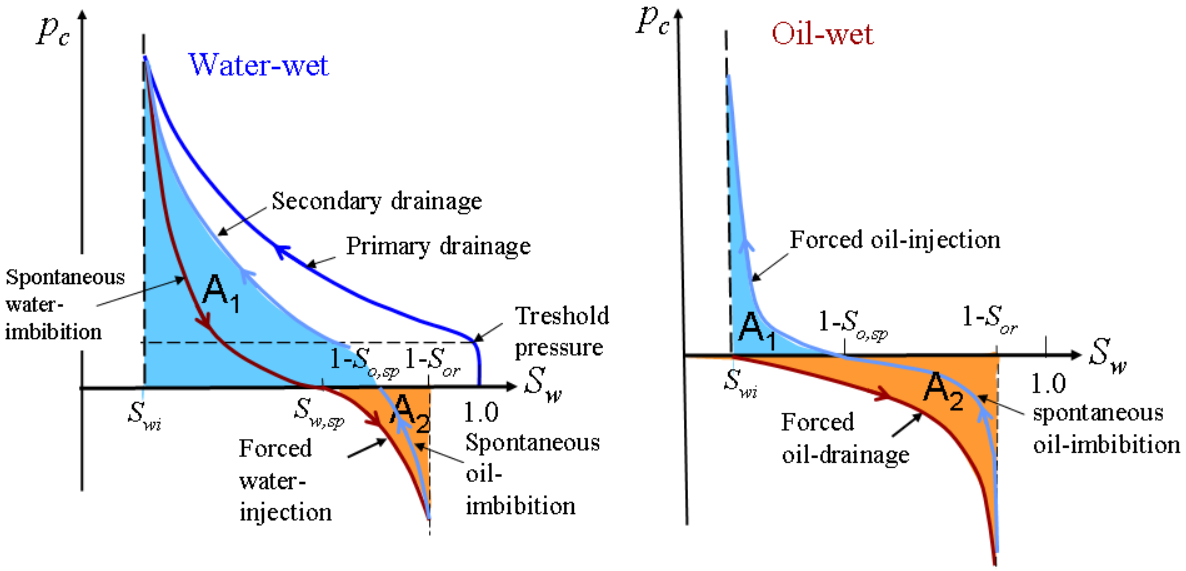


**Figure 2.6** *Capillary pressure curves for a water-wet and an oil-wet rock [12].*

The capillary pressure curve for a *water-wet* rock demonstrates many displacing processes:

- **Primary drainage process:**

  Imagine a water-wet core fully saturated with water ($S_w$ = 1). By injecting oil, water is displaced in a drainage process. As the injection pressure exceeds the threshold pressure, the largest pores are first filled with oil. This is shown in the capillary pressure curve to the left in Figure 2.6. As more oil is injected at higher and higher injection pressure, the water saturation decreases towards the irreducible water saturation $S_{wi}$ where the oil saturation reaches its maximum value.

- **Spontaneous water-imbibition:**

  Due to the water-wet nature of the rock, water is sucked back into the core when the external pressure is lowered. The volume of oil spontaneously displaced from a region may vary from a fraction of a single pore space to an assembly of pores. When $P_c$ = 0, the water saturation has increased to $S_{w,sp}$.

- **Forced water-injection**

  In order to increase $S_w$ even further, water is injected. The pressure is reversed until the water saturation reaches $S_w = 1 - S_{or}$.

- **Spontaneous oil-imbibition**

  When the reversed pressure is lowered, some oil is sucked back into the core and the water saturation becomes $S_w = 1 - S_{o,sp}$. Note that the amount of oil spontaneously

imbibed is less than the amount of spontaneously imbibed water due to the water-wet nature of the rock.

- **Secondary drainage**

Irreducible water saturation $S_{wi}$ is once again obtained by injecting more oil.

In an *oil-wet* rock, other displacing processes occur as illustrated in the curve to the right in Figure 2.6.

- **Forced oil-drainage**

In this case, since oil is the wetting fluid, water injection is a drainage process. Water is injected into a oil saturated core plug until maximum water saturation $S_w = 1 - S_{or}$ is reached.

- **Spontaneous oil-imbibition**

A relatively large quantity of oil will spontaneously imbibe as the reversed pressure is reduced, resulting in a lower water saturation $S_w = 1 - S_{o,sp}$.

- **Forced oil-injection**

$S_{wi}$ is obtained by injecting oil.

Changes in the wettability of a rock core have been shown to affect capillary pressure, electrical properties, waterflood behaviour, relative permeability, dispersion, simulated tertiary recovery, irreducible water saturation $S_{wi}$, and residual oil saturation $S_{or}$ [14]. Notably, the curves for the drainage and imbibition processes are not the same, forming a loop. Likewise, the capillary pressure curves for primary drainage differs from the one for a secondary drainage. This inconsistency of the $P_c$-conditions illustrates the *capillary pressure hysteresis*. In a porous media, the capillary pressure hysteresis is identified as a permanent hysteresis because it is independent of experimental time [15].

Wetting angle hysteresis is one cause of capillary pressure hysteresis. During drainage, the non-wetting fluid displaces the wetting fluid from the core. The wetting fluid is being pushed back from surfaces it previously covered, creating a receding wetting angle $\theta_{rec}$ between the two fluids. The advancing wetting angle, $\theta_{adv}$, is important during imbibition. The concept of wetting angle hysteresis can be recognized by measuring $\theta_{rec}$ and $\theta_{adv}$ of an oil drop suspended between two horizontal plates of glass, submerged in water. The lower plate in Figure 2.7 is fixed while the other can move tangentially in either direction. The receding angle is smaller than the advancing angle.

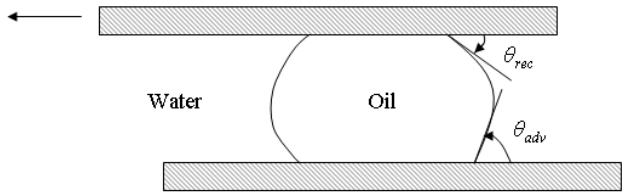


**Figure 2.7** *Measurement of wetting angle hysteresis*

The hysteresis phenomenon stabilizes the fluid interfaces in the pores, so that the fluid distribution in the porous medium is preserved. In addition, it is related to the snap-off effect as mentioned earlier, i.e. a differential dissipation of the interfacial tension near the pore walls cause a snap-off of small, immobile droplets.

The values where the curves in Figure 2.6 cross the $S_w$-axis, $S_{w,sp}$ and $1 - S_{o,sp}$, depend on the wettability. A high $S_{w,sp}$-value indicates a water-wet rock. Two ways to measure the wettability of the rock core is the USBM-index and the Amott-Harvey index [16].

### 2.5.1 USBM-index

When water is drained from the water-wet core in Figure 2.6 a work is performed against the capillary forces. The *USBM test* (United States Bureau of Mines) compares the work necessary for one fluid to displace the other [17]. The total work executed during the secondary drainage process is proportional to the area $A_1$ below the secondary drainage curve.

$$A_1 = -\int_{1-S_{o,sp}}^{S_{wi}} P_c(S_w)\,dS_w \tag{2.14}$$

The minus sign in Equation (2.14) is needed since the change in water saturation, $dS_w$, is negative.

The area under the forced water injection curve $A_2$, is proportional to the work needed to displace the oil.

$$A_2 = \int_{S_{w,sp}}^{1-S_{or}} P_c(S_w)\,dS_w \tag{2.15}$$

Because of the favourable free-energy change, the work required for the wetting fluid to displace the non-wetting fluid from the core is less than the work required for the opposite displacement. So, in a strongly water-wet porous medium, a great work is required in order to drain the water with oil. This results in a large area $A_1$. For an oil-wet core, drainage is easily executed resulting in a small area $A_1$. The same analysis can be executed for $A_2$, a small area indicates a water-wet core and a large one indicates an oil-wet core.

The *USBM-index* is used to classify the average wettability of a rock.

$$I_{USBM} = log\left(\frac{A_1}{A_2}\right) \tag{2.16}$$

The different classifications of wettability are

- $I_{USBM} > 0$: water-wet
- $I_{USBM} \approx 0$: neutral
- $I_{USBM} < 0$: oil-wet

The USBM test is favourable because of its sensitivity near neutral wettability. A minor disadvantage is that the index can only be measured on plug-sized samples because the samples must be spun in a centrifuge.

### 2.5.2 Amott-Harvey index

The *Amott-Harvey index* (AH) is an alternative way to classify the wettability [18]. This technique is based on the fact that the wetting fluid will imbibe spontaneously into the core, displacing the non-wetting fluid. In other words, the AH test focus on where the capillary pressure curves cross the $S_w$-axis. If $S_{w,sp}$ moves to the right on the $S_w$-axis, the water saturation increases as more water has imbibed spontaneously into the core. We define the "displacement-by-oil ratio"

$$\delta_w = \frac{V_{o,sp}}{V_{ot}} = \frac{S_{w,sp} - S_{wi}}{1 - S_{or} - S_{wi}} \tag{2.17}$$

where $V_{o,sp}$ is the volume of the oil displaced during the spontaneous water imbibition and $V_{ot}$ is the total volume of oil displaced in both the spontaneous imbibition and the forced water injection.

If $(1 - S_{o,sp})$ has moved to the left in the oil-wet curve in Figure 2.6, the oil saturation has increased, more oil have imbibed spontaneously into the core. In this case, we define the "displacement-by-water ratio"

$$\delta_o = \frac{V_{w,sp}}{V_{wt}} = \frac{(1-S_{or})-(1-S_{o,sp})}{1-S_{or}-S_{wi}} = \frac{S_{o,sp}-S_{or}}{1-S_{or}-S_{wi}} \tag{2.18}$$

where $V_{w,sp}$ is the volume of the water displaced during the spontaneous oil imbibition and $V_{wt}$ is the total volume of water displaced. The wettability can be defined by the Amott-Harvey index

$$I_{AH} = \delta_w - \delta_o = \frac{V_{o,sp}}{V_{ot}} - \frac{V_{w,sp}}{V_{wt}} = \frac{(S_{w,sp}-S_{wi})-(S_{o,sp}-S_{or})}{1-S_{or}-S_{wi}} \tag{2.19}$$

For this method, the different wettability classifications are

- $0.3 < I_{AH} < 1$: water-wet
- $-0.3 < I_{AH} < 0.3$: neutral
- $-1 < I_{AH} < -0.3$: oil-wet

The main problem with the AH test is that it is insensitive near neutral wettability since neither fluid will spontaneously imbibe when the contact angle is in the range of $60^o$ to $120^o$ [16].

## *2.6 Sandstones*

One of the core samples used in this thesis is an outcrop *Berea sandstone*, a commonly used rock in petroleum research. In general, sandstones are common reservoir rocks containing a relatively large percent of the world's petroleum reserves. A sandstone is defined as a sedimentary rock with grains in the size range of 63 μm to 2 mm [19]. The sand grains are formed by the breakdown of pre-existing rocks by weathering and erosion, and from material

which forms during transport and deposition. A common term for this material is siliciclastic sediments. The Berea sandstone is a sedimentary rock whose well-sorted and well-rounded grains are predominantly sand-sized and composed of quartz sand held together by silica [20]. Since the porosity and permeability of a porous media is affected by grain shape, size, sorting and fabric [21], Berea sandstones possess good reservoir qualities. This is why it is considered as relatively homogeneous and suitable for laboratory experiments.

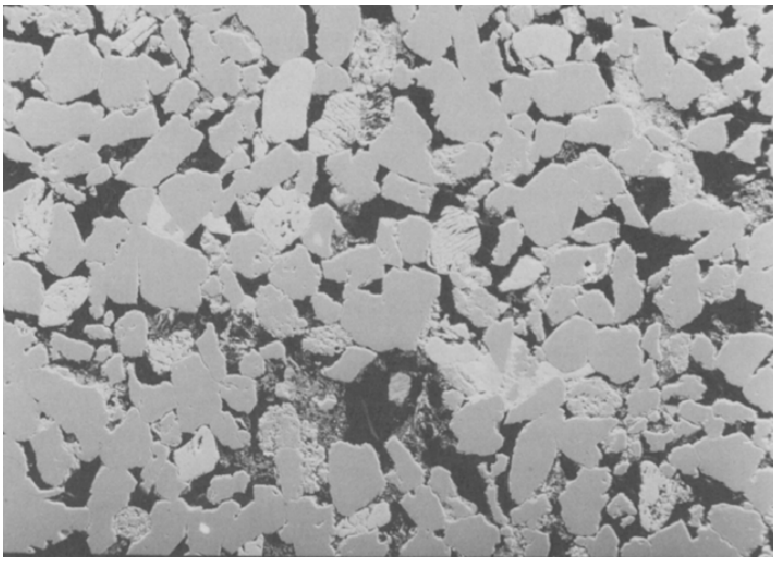

**Figure 2.8** *Scanning Electron Microscope (SEM) image of a typical Berea sandstone at 50x magnification [22].*

## *2.7 Carbonates*

The work in this thesis is partly performed on outcrop limestones. By definition, a limestone is any sedimentary rock containing over 50 % calcium carbonate ($CaCO_3$) [19]. Hence, it is generally referred to as a carbonate rock. Carbonate rocks are well known for their complex petrophysical behaviour where, in contrast to siliciclastic rocks, different parameters, including porosity and permeability, usually are not directly related. The complex carbonate microstructure reflects their origin. The hard parts of dead organisms constitute a principal source of calcium carbonate, making this biogenic material a main component of most carbonates. Carbonate sediments may build up in any location where there is a supply of biogenic carbonate and a restriction on the amount of clastic sediments, typically in coastal and shallow marine environments.

As reservoirs, carbonates hold around 60 % of the oil and 40 % of the gas in the world [4]. Thus, they are as important as sandstones, but their development and production present a different set of problems. Since silica, a material present in most sandstones, is chemically more stable than calcium carbonate, the effects of diagenesis are more marked in carbonates than in sandstones. During diagenesis the primary porosity of carbonates is thoroughly reorganized. Repeated cementation, dissolution and fracturing result in the heterogeneities and complex structures that is a combination of primary and diagenetic pores. The porosity of carbonate rocks can be further categorized into intragranular porosity, intergranular porosity and vugs [11, 21]. Intragranular porosity is the porosity inside the grains, while intergranular porosity is found between the grains. A vug is defined as a pore space that is significantly larger than the grains and crystals of a rock, and is easily visible to the naked eye [23]. Leached grains, fossil chambers, cavernous, breccias, fractures and cavities are mainly the origin cause of these vuggy pore structures. The image to the left in Figure 2.9 shows a vug with a diameter of 1 mm, while intragranular and intergranular porosity is illustrated to the right.

In reservoir characterization, the heterogeneity of the reservoir rock specifically affects fluid flow. Hence, reservoir rocks with a secondary pore system, like vuggy porosity, have flow properties different from other rocks. These heterogeneities often cause large variations in the petrophysical properties of the rock, violating the classical concepts of fluid flow in porous media.

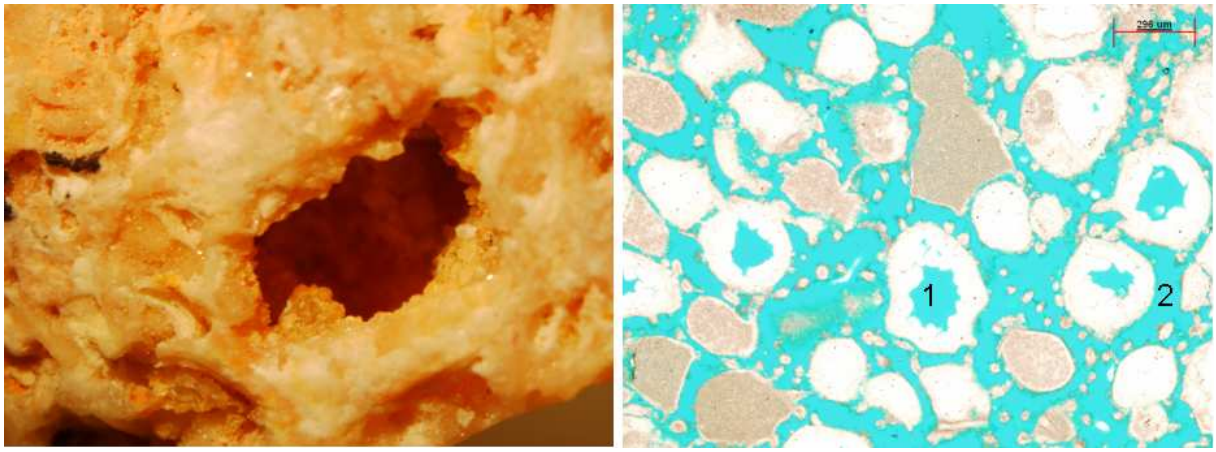


**Figure 2.9** *Left: A vug with a diameter of 1 mm, illustrating the large heterogeneity caused by vuggy porosity. Right: Image indicating 1) intragranular and 2) intergranular porosity.*

The effects of vugs on the petrophysical characteristics of the rock are related to the type of vug interconnection. Lucia [24] found that the vuggy pore space was divided into separate and touching vugs. Separate, or isolated, vugs are defined as pore space that is connected only through the intergranular porosity, whereas touching, or connected, vugs are defined as pore space forming an interconnected system independent of the intergranular porosity. The intergranular porosity is often referred to as matrix porosity in the literature. While the addition of separate vugs increases the total porosity, it does not significantly increase the permeability of the rock. The presence of touching vugs, on the other hand, increases the permeability well above what would be expected from the matrix porosity [24]. Figure 2.10 illustrates the categorization of vuggy pore space. Overall, the predictability of petrophysical properties of carbonate rocks is mainly hampered by this great variability of the connectivity of different pore types.

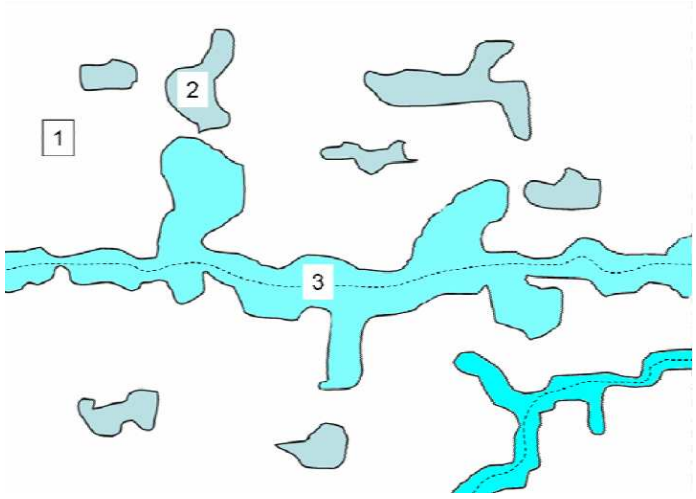


**Figure 2.10** *Illustration of the categorization of vuggy pore space. 1) Matrix pore space 2) Isolated vugs 3) Touching vug network [25].*

# 3 Methods for capillary pressure curve measurements

A porous medium is much more complex than capillary tubes. Nevertheless, capillary pressure has a great effect on how fluids fill the pores of a rock. In evaluating hydrocarbon reservoirs, laboratory capillary pressure measurements on reservoir cores are directly applied to determine basic petrophysical properties such as pore size distribution, irreducible water saturation, residual oil saturation and wettability of reservoir rocks.

At least three methods of capillary pressure measurements are widely accepted in the industry today. These are the mercury injection, porous plate and centrifuge methods. By utilizing these methods, capillary pressure curves can be established for both gas-liquid and liquid-liquid systems. Experimental work [26] has shown that in a gas-liquid system, e.g. an air-brine system, the porous plate and centrifugation technique give close results. This is indicated in Figure 3.1. The same study also proved that capillary pressures for a gas-liquid system are not transposable to a liquid-liquid system. Hence, oil-brine capillary pressure measurements are necessary to study oil-brine interactions in particular. The three methods for obtaining capillary pressure curves are further explained in the following sections.

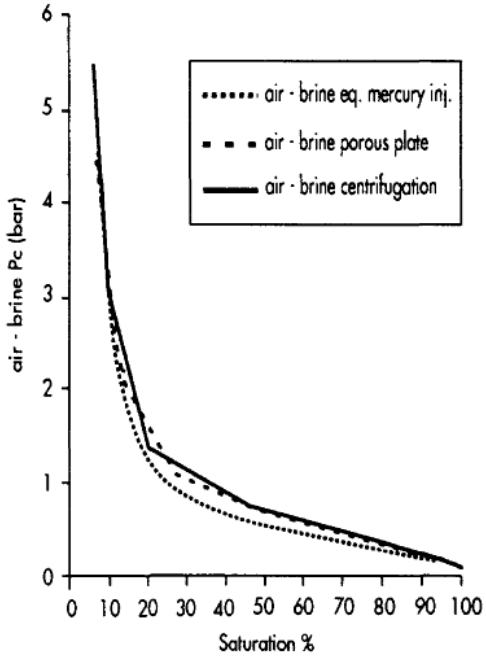


**Figure 3.1** *Capillary pressure curves, for a air-brine drainage in a sandstone rock core, comparing the three methods [26].*

## *3.1 Mercury injection method*

This technique involves forcing mercury under pressure into the evacuated pores of a porous media [1]. The amount of mercury injected under various pressures is determined and used to produce the capillary pressure curve. It is a fairly quick method and it can also be used to determine the pore size distribution. However, there are several disadvantages with the mercury injection method. It cannot be used to find the irreducible water saturation nor the reservoir wettability. In addition, mercury is an unnatural fluid which has a destructive effect on the core sample and it is used to a lesser extent due to the pollutive nature of mercury.

## *3.2 Porous plate method*

This method uses a porous plate, a diaphragm, to measure the capillary pressure curves [2]. The relation between the capillary pressure and the saturation can be found for a small core by starting with 100 % saturation. The plate is saturated with the wetting fluid and put under high displacement pressure. A core, saturated with the same fluid, is placed on top of the porous plate. On the upper side of the plate, non-wetting fluid is added, while the lower chamber is filled with wetting fluid. Successively greater suctions can be applied from the lower chamber to the wetting fluid in the plate. The saturation of the core can be found by measuring the quantity of fluids removed from the core when equilibrium is obtained at each value of suction. It is important that the suction does not exceed the displacement pressure of the porous plate as this will cause air to enter the plate and end the measurements.

The porous plate method is very satisfactory in the region of low capillary pressures. It is limited by the low displacement pressures of the plate and the fact that the measurements can be very time consuming.

## *3.3 Centrifuge method*

The centrifuge method was introduced by Hassler and Brunner in 1945 [3]. Since then, it has been extensively investigated and increasingly used in the petroleum industry. This method involves rotating fluid bearing rock cores at variable speeds in a centrifuge. The centrifugal force will counterbalance the capillary pressure so that fluids are produced from the core. The quantity of expelled fluids as a function of increasing rotational speed can be converted into

the capillary pressure as a function of fluid saturation. The method has several technical advantages; including the absence of semi-permeable filters, the ability of analyzing several samples using a single machine, and that the experimental time is short compared to other methods. However, there are some problems concerning the basic theory and the experimental set up. These disadvantages will be discussed shortly before the end of this chapter. The fluid saturation of the core is not a constant throughout the core, but varies with the distance from the rotation axis. Also, the capillary pressure cannot be read directly, but must be calculated from centrifuge speeds and other known parameters.

Hassler and Brunner made several experimental assumptions [27]:

a) A homogeneous sample is considered to have fluid continuity all along the sample.
b) Within the sample, the $P_c$ saturation function is smooth and differentiable.
c) Gravity is negligible compared to the centrifuge field.
d) A small sample is used, i.e. $r_1 \approx r_2$ and $(r_1/r_2)^2 \approx 1$.
e) The capillary pressure at the outlet face of the core, near the produced fluid container in Figure 3.2, is zero.

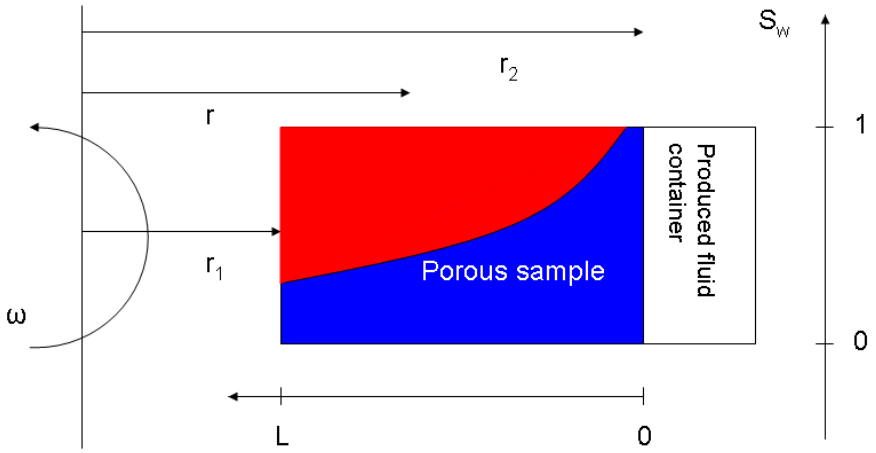


**Figure 3.2** *Saturation profile within a porous sample rotated in a centrifuge. The non-wetting phase (red) is displacing the wetting phase (blue) at a constant angular velocity ω, and the effluent from the core is collected in the produced fluid container.*

The cylindrical core sample in Figure 3.2 is saturated with a wetting fluid of density $\rho$, e.g. water, and placed in a centrifuge after its dry and saturated weights have been measured. The centrifuge is then run at successively greater speeds and the wetting fluid is produced. The speeds are held constant until equilibrium is obtained, i.e. when there is no more additional fluid production observed. A stroboscopic light is used to read the quantity of produced fluid in the container before the centrifuge speed is increased further.

An equation for capillary pressure as a function of radius $P_c(r)$ can be estimated by considering a small fluid volume of mass $\Delta m$ contained within a pore in the core. $\Delta m$ can be considered as a small disk of volume $dV = \Delta A\, dr$, where $\Delta A$ is perpendicular to the radius as shown in Figure 3.3.

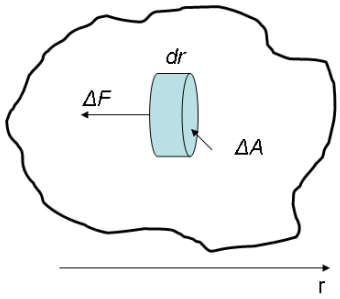


**Figure 3.3** *A small fluid volume of mass Δm within a pore.*

When the core is put in the centrifuge the fluid volume will rotate at an angular velocity $\omega$. This means that it is subjected to a centripetal force:

$$\Delta F = \Delta m \omega^2 r \tag{3.1}$$

This force is acted upon $\Delta m$ from the neighbouring fluid elements; hence there is a pressure difference across the fluid element $\Delta m$.

$$\begin{aligned} &[P(r+dr) - P(r)]\Delta A = \Delta F = \Delta m \omega^2 r = \rho \Delta A dr \omega^2 r \\ &\frac{P(r+dr) - P(r)}{dr} = \rho \omega^2 r \end{aligned} \tag{3.2}$$

In the limit $dr \rightarrow 0$ we find:

$$\frac{dP}{dr} = \rho \omega^2 r \tag{3.3}$$

Assuming there is only one fluid in the core, the pressure at radius $r$ can be found by integration.

$$\int_{P(r)}^{P(r_2)} dP = \int_{r}^{r_2} \rho\omega^2 r dr$$

$$P(r_2) - P(r) = \frac{1}{2}\rho\omega^2(r_2^2 - r^2) \tag{3.4}$$

$$P(r) = P_2(r_2) + \frac{1}{2}\rho\omega^2(r^2 - r_2^2)$$

$P_2$ is the pressure at the outlet end of the core, normally represented by the atmospheric pressure.

If there are two fluids present in the core, a wetting and a non-wetting fluid, the pressure difference function above is valid for both fluids.

$$P_w(r) = P_{2,w}(r_2) + \frac{1}{2}\rho_w\omega^2(r^2 - r_2^2) \tag{3.5}$$

$$P_{nw}(r) = P_{2,nw}(r_2) + \frac{1}{2}\rho_{nw}\omega^2(r^2 - r_2^2) \tag{3.6}$$

Since capillary pressure is defined as the difference in pressure across the interface between the two immiscible fluids and assuming that the outlet pressure is the same for both fluids, the following equation can be obtained:

$$P_C(r) = P_{nw}(r) - P_w(r) = \frac{1}{2}\Delta\rho\omega^2(r_2^2 - r^2) \tag{3.7}$$

An important observation in this equation is that the capillary pressure depends only on the radius $r$ from the rotation axis and the angular frequency $\omega$ of the centrifuge.

Now, the main purpose of the Hassler-Brunner method is to relate the capillary pressure and saturation $S_w$ for a given core. The average water saturation of the core $\overline{S}_w$ will be given by

$$\overline{S_w} = \frac{1}{r_2 - r_1}\int_{r_1}^{r_2} S_w(r,\omega)dr \tag{3.8}$$

In order to change the variables in the integral from $S_w(r)$ to $S_w(P_c)$, Equation (3.7) is used to find an expression for $dr$ and $1/(r_2 - r_1)$:

$$P_C(r) = \frac{1}{2}\Delta\rho\omega^2(r_2^2 - r^2) \Rightarrow dP_C = -\Delta\rho\omega^2 r dr \Rightarrow dr = -\frac{1}{\Delta\rho\omega^2 r}dP_C \tag{3.9}$$

$$\begin{aligned} P_{C1}(r_1) &= \frac{1}{2}\Delta\rho\omega^2(r_2^2 - r_1^2) = \frac{1}{2}\Delta\rho\omega^2(r_2 - r_1)(r_1 + r_2) \\ \Rightarrow \frac{1}{r_2 - r_1} &= \frac{1}{2P_{C1}}\Delta\rho\omega^2(r_1 + r_2) \end{aligned} \tag{3.10}$$

An expression for the radius $r$ can be found by dividing the capillary pressure at $r$ with the capillary pressure at the inlet face of the core $r_1$:

$$\frac{P_C}{P_{C1}} = \frac{r_2^2 - r^2}{r_2^2 - r_1^2} \Rightarrow r = \sqrt{r_2^2 - \frac{P_C}{P_{C1}}(r_2^2 - r_1^2)} = r_2\sqrt{1 - \frac{P_C}{P_{C1}}\left[1 - \left(\frac{r_1}{r_2}\right)^2\right]} \tag{3.11}$$

The expressions for $dr$, $1/(r_2 - r_1)$ and $r$ are put into Equation (3.8) to obtain an expression for the average saturation in the plug:

$$\overline{S_w} = \frac{1 + \left(\frac{r_1}{r_2}\right)}{2P_{C1}} \int_0^{P_{C1}} \frac{S_w(P_C)dP_C}{\sqrt{1 - \frac{P_C}{P_{C1}}\left[1 - \left(\frac{r_1}{r_2}\right)^2\right]}} \tag{3.12}$$

Since Hassler and Brunner failed to find an analytical solution to Equation (3.12), they favoured the simplifying assumption $r_1 \approx r_2$. This was considered reasonable for very short cores if the centrifuge diameter was sufficiently large. The equation above becomes:

$$\overline{S_w} \cong \frac{1}{P_{C1}} \int_0^{P_{C1}} S_w(P_C)dP_C \tag{3.13}$$

Finally, an equation for the saturation as a function of capillary pressure $S(P_C)$ is found by inverting the integral:

$$S_w(P_{C1}) = \frac{d}{dP_{C1}}(P_{C1} \times \overline{S_w}) \tag{3.14}$$

This means that the capillary pressure curve can be found by centrifuging a core with different angular rotations $\omega$. After the run, the cores are removed and weighed to check the saturation value obtained from the last reading of produced fluid. The values of $P_{c1}$ are computed from

Equation (3.7) and the average saturation $\overline{S}$ of each core is obtained from the dry and saturated weights and the corresponding container reading. A plot of $\overline{S}\,P_{c1}$ as a function of $P_{c1}$ can be prepared from the experimental data. The points indicated on the curve in Figure 3.4 are the first, second and third rotational speeds. The saturation that goes with each value of capillary pressure is obtained from this curve by graphical differentiation according to Equation (3.14).

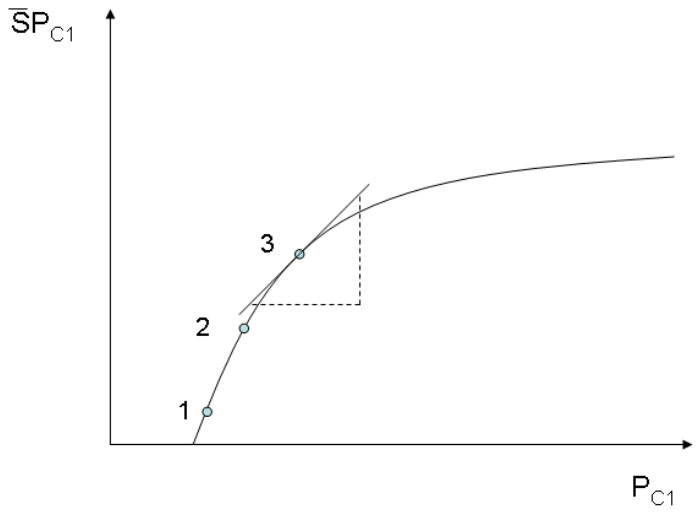


**Figure 3.4** *Graphical differentiation of $P_{c1}\overline{S}$ vs. $P_{c1}$ curve. Points indicate first, second and third centrifugation speed.*

It should be noted that Equation (3.14) is an approximate solution introduced by Hassler and Brunner. Many alternative solutions based on Equation (3.12) have been proposed by other scientists, collectively reviewed by Ruth and Chen [28]. Several scientists have questioned the assumptions made by Hassler and Brunner, including the assumption of zero-capillary pressure at the outflow boundary [29], the neglected effects of cavitations and radial effects [30-31], and the effect of a non-uniform centrifugal force field distribution [28].

A complete capillary pressure curve usually requires about 15 speeds and may take several days to acquire, depending on the wettability preference and permeability of the core samples. There exists no global, absolute requirement for the equilibrium states during the experiments [28]. Thus, the equilibrium state is often determined based on experience. If non-equilibrium data is used for processing, an unknown level of uncertainty is accepted in the resulting capillary pressure relationship. Hassler and Brunner [3] argued that the speed of the centrifuge

should never be allowed to decrease as this would spoil the run. This is because the fluids will tend to redistribute throughout the core when the centrifugal force is no longer present.

It should also be emphasized that at any given rotational speed, a wide range of capillary pressures exist, distributed within the core. Therefore, the capillary pressure distribution is connected to a fluid saturation distribution along the length of the core. Since this method only measures the average fluid saturation $\overline{S}$, it fails to produce the actual distributions. The Hassler-Brunner solution is now generally used as an initial guess to the correct solution. Centrifuge experiments must be carefully designed and performed in order to obtain useful information on capillary pressure curves.

## *3.4 Capillary end effect*

Figure 3.2 shows that there is a high saturation of the wetting phase at the outlet of the porous medium. This hold-up of the wetting phase is called *the capillary end effect*, or the boundary effect, and it comes about because of the discontinuity in capillary pressure when the flowing fluids leave the porous medium. The discontinuity makes it more difficult for the wetting phase than the non-wetting phase to leave the core. Leverett [32] concluded in his studies that the end effect is confined to a zone a few feet in diameter near the well, and therefore not an important factor in behaviour of large-scale reservoirs. However, they can significantly affect measured saturations and recoveries in laboratory-scale experiments, and must be accounted for.

## *3.5 Measurements at reservoir and ambient conditions*

Capillary pressure measurements are ultimately executed at reservoir conditions, i.e. at reservoir temperature and pressure. Since this is time-consuming and requires expensive equipment, it is often preferable to measure at ambient conditions, as is the case in this study.

Sinnokrot et al. [33] investigated the effect of temperature on the capillary pressure curve. They found that irreducible water saturation in a sandstone rock obtained under high temperature was higher than that obtained under low temperature for a refined oil/brine system. This was later confirmed when Søndenå et al. [34] compared capillary pressure

curves obtained by the porous plate method at ambient conditions and at reservoir conditions. They concluded that the differences between the curves from the two conditions resulted from temperature effects rather than pressure effects. The high temperature caused the wettability preference of the samples to change from intermediate to oil-wet when water was displaced with live crude oil, affecting the water saturation of the rock. This change in the rock's wettability preference is one of many challenges occurring when measuring at high temperatures and pressures, which is why measurements at room temperature are considered as an adequate solution. Søndenå et al. used sandstone core plugs from a North Sea reservoir in their research. Capillary pressure curves determined at both reservoir and ambient conditions are shown in Figure 3.5.

However, studies have also shown that the above statements are only valid for sandstones, and that the effect of temperature on capillary pressure of limestone rocks is negligible [33, 35-36].

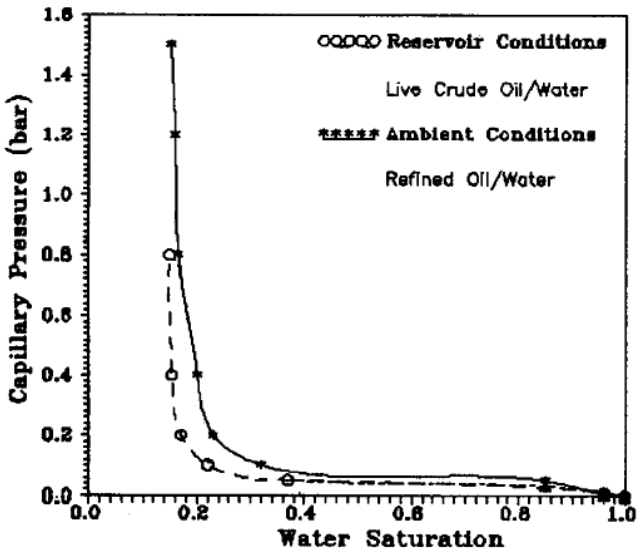


**Figure 3.5** *Capillary pressure curves measured at reservoir and ambient conditions [34].*

# 4 Nuclear Magnetic Resonance (NMR)

## *4.1 Introduction to the physical background of NMR*

Nuclear magnetic resonance was first observed in 1946 by scientists Edward Purcell and Felix Bloch at Harvard and Stanford Universities, respectively. Since then, there has been a rapid growth in the number of NMR applications. It has been used in petroleum exploration since the early 1950's.

NMR is a phenomenon which occurs when the nuclei of certain atoms are placed in a static magnetic field and exposed to a second oscillating magnetic field. Some nuclei experience this phenomenon, and others do not, depending upon whether they possess a nuclear spin. Systems of spinning charged particles will also possess magnetic moments (**μ**) which give rise to nuclear magnetism. An atomic nucleus will also rotate which gives it an angular momentum, **J**. Since they are parallel, the relation between these parameters is

$$\boldsymbol{\mu} = \gamma \mathbf{J} \tag{4.1}$$

where $\gamma$ is the gyromagnetic ratio unique for the nucleus in question. For hydrogen (a single proton $^1$H), $\gamma = 26.75 \times 10^7$ rad/T · s [37].

In NMR, the proton often is the nucleon in question due to its high $\gamma$-value. The magnetic moments of protons are originally randomly oriented. By placing the nucleus in a static magnetic field $\mathbf{B}_0$, the force from the field will try to align **μ** along the field by a torque **τ**

$$\boldsymbol{\tau} = \boldsymbol{\mu} \times \mathbf{B}_0 \tag{4.2}$$

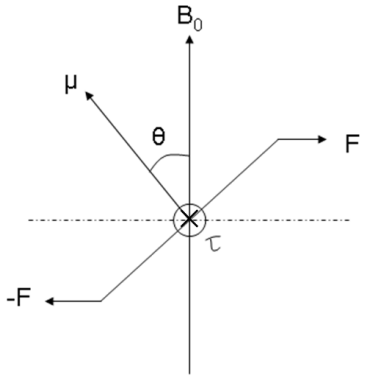


**Figure 4.1** *The torque* $\boldsymbol{\tau}$ *tries to align the magnetic moment* $\boldsymbol{\mu}$ *along the outer magnetic field* $\boldsymbol{B}_0$.

By applying an external force to rotate **μ** from its equilibrium position, the energy of the magnetic moment will change. Imagine the same proton in a magnetic field $\mathbf{B}_0$. The direction and magnitude of the magnetic moment will be quantized by

$$\mu_z = \gamma \hbar m_z \tag{4.3}$$

where $m_z$, the magnetic quantum number of hydrogen, can have two values, one parallel to the field $\mathbf{B}_0$ (positive) and one anti-parallel to $\mathbf{B}_0$ (negative). Thus, $m_z = \pm ½$. This implies that there will be two energy states with a potential energy given by

$$U = -\boldsymbol{\mu} \cdot \mathbf{B}_0 = -\mu_z B_0 = -\gamma \hbar m_z B_0 \tag{4.4}$$

where $\hbar$ is Planck's constant $h$ divided by $2\pi$. The two states are known as the *α- and β-state* [38]. They are also referred to as the parallel and anti-parallel states because of the alignment the magnetic moment will have compared to $\mathbf{B}_0$ in the two energy states. The α-state is the lower energy state, while the β-state is the higher. The distribution of protons is governed by Boltzmann statistics; and at room temperatures and field strengths the population is slightly higher in the lower energy state [39].

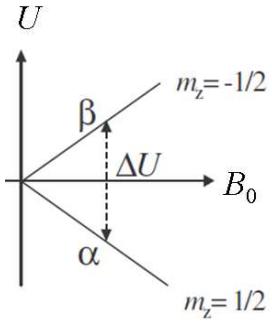


**Figure 4.2** *The two energy states of a proton as a function of the static magnetic field* $\boldsymbol{B}_0$ *[38].*

In order to excite protons from the α-state to the β-state, a photon must be absorbed. This photon is produced by an oscillating magnetic field $\mathbf{B}_1$, also known as the RF-field, which is perpendicular to $\boldsymbol{\mu}$ and $\mathbf{B}_0$. The photon must possess an energy given by Planck's law.

$$\Delta U = hf = \gamma \hbar B_0 \tag{4.5}$$

The new field $\mathbf{B}_1$ has to precess perpendicular to $\mathbf{B}_0$ with the Larmor frequency $f_L$, which is the frequency with which $\boldsymbol{\mu}$ precesses around $\mathbf{B}_0$. This is the frequency at which the magnetic nuclei can absorb or emit energy, known as the resonance frequency.

$$f_L = \frac{\gamma}{2\pi} B_0 \tag{4.6}$$

The equation above states that the precession frequency of the individual nuclei is proportional to the strength of the static magnetic field.

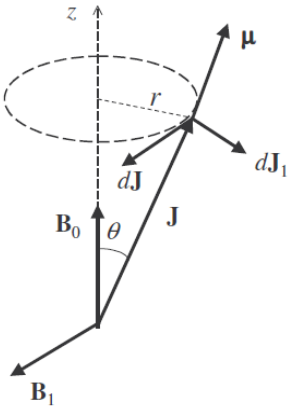


**Figure 4.3** *The RF-field* $\boldsymbol{B}_1$ *is perpendicular to* $\boldsymbol{J}$ *and* $\boldsymbol{B}_0$ *and causes a movement of* $\boldsymbol{J}$, $\boldsymbol{dJ}_1$, *towards the β-state [38].*

The new field $\mathbf{B}_1$ will have an influence on the movement of **J** and the magnetic moment will be exposed to a new torque, $\tau_1$.

$$\tau_1 = \boldsymbol{\mu} \times \mathbf{B}_1 = \frac{d\mathbf{J}_1}{dt} \tag{4.7}$$

$d\mathbf{J}_1$ is the change in **J** caused by the RF-field $\mathbf{B}_1$. As shown in Figure 4.3, **J** will move into the β-state since it is tilted in the opposite direction of the static field $\mathbf{B}_0$.

The principle of a NMR-instrument is shown in Figure 4.4 [37]. This general sketch can be used to explain how the different fields actually are generated in the laboratory. The static magnetic field $\mathbf{B}_0$ is created by a powerful electromagnet. Two coils are oriented around the sample tube, perpendicular to the static field. One of these, the transmitter coil, is generating the high frequency RF-field. It is the absorption of photons from this RF-field that causes the excitation of protons from the α-state to the β-state. This is only the case when $\mathbf{B}_1$ precesses with the Larmor frequency $f_L$, which is when the resonance condition is fulfilled. The other coil, the receiver coil, detects the photons emitted as the protons fall back into the lower energy state (α-state). In practice, there is no need for two separate coils, as one coil can operate as both transmitter and receiver at the same time.

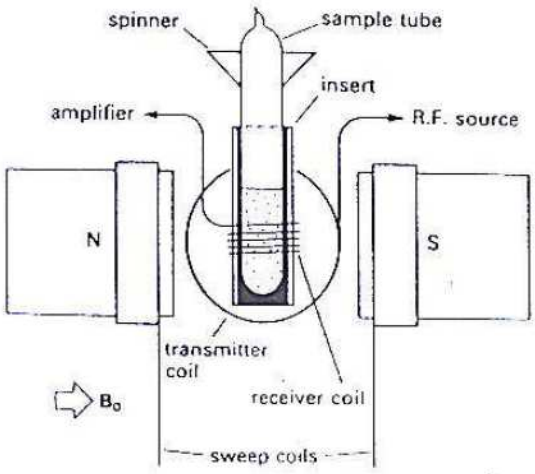


**Figure 4.4** *The principle and components of a NMR-instrument [37].*

With the orientation of the receiver coil in Figure 4.4, the signal strength $S$ is

$$S = \frac{a\gamma^4 N B_0^2 B_1 g(f)}{T} \tag{4.8}$$

where $a$ is a proportionality coefficient depending on the design of the instrument, $N$ reflects the amount of nuclei in the sample and $T$ is the temperature [37]. $g(f)$ is a Lorentzian signal shape factor.

In order to obtain a good NMR signal, according to Equation (4.8), the following conditions are of importance:

- Since the signal strength $S$ is proportional to $N$, the core should be enriched with as much of the isotope in question as possible.
- The strong dependence on the gyromagnetic ratio implies that nuclei with a high resonance frequency, and thus a high $\gamma$, yield a stronger NMR signal.
- Since the signal is inversely proportional to the temperature $T$, it is favourable to have as low temperatures as possible.
- Equation (4.8) also implies that the static magnetic field $\mathbf{B}_0$ should be as strong as possible.

It should be noted that low-field NMR is favourable when studying porous media. This is because a higher field strength, although improving the signal, also causes higher internal gradients, degrading the measurements [40].

The measured signal in NMR is called the Free Induction Decay (FID). The FID is induced by (i) allowing the magnetic nuclear spins to reach thermal equilibrium in a magnetic field; (ii) exciting the spins with an RF-pulse, and (iii) detecting and amplifying the weak RF-signal that is emitted as the spins resume their distribution among the α- and β-state. The FID is influenced by magnetic field uniformity and the presence of paramagnetic nuclei [41]. A long FID gives a sharp peak at the Larmor frequency when Fourier transformed to the frequency domain. A broad peak, obtained at short FID's, indicate a heterogeneous field distribution in the sample. This is typically what can be obtained in a rock sample. Multiple-pulse sequences can be used to separate out the different effects of the FID. Examples of these are the inversion recovery method and the CPMG sequence described in the following sections.

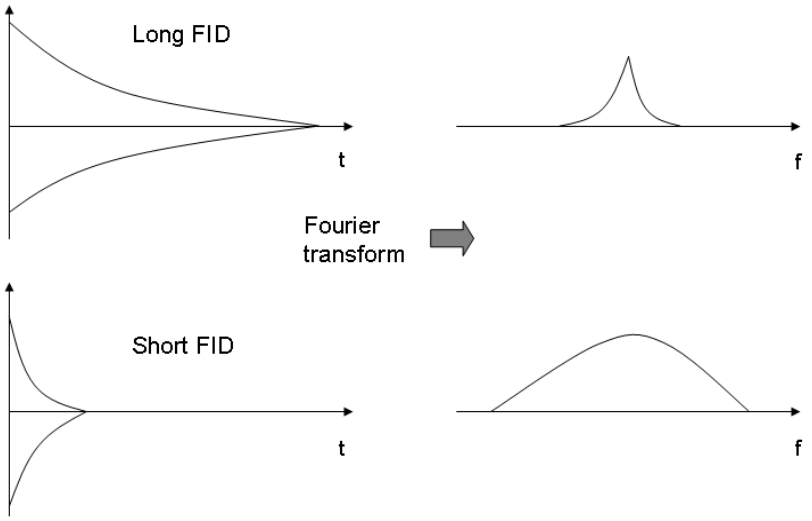


**Figure 4.5** *A long Free Induction Decay (FID) exhibits a sharp peak at the Larmor frequency, when Fourier transformed to the frequency domain. A short FID shows a broad peak [41].*

## *4.2 Relaxation*

As mentioned earlier, when the magnetic moments are placed in a static field $\mathbf{B}_0$ they will distribute themselves between the two energy states. As a result of this asymmetric distribution, a thermal equilibrium magnetization $\mathbf{M}_0$ will occur as shown in Figure 4.6. This is the sum of the magnetic moments of all the protons.

$$\mathbf{M}_0 = \sum_{i}^{N} \boldsymbol{\mu}_\mathbf{i} \tag{4.9}$$

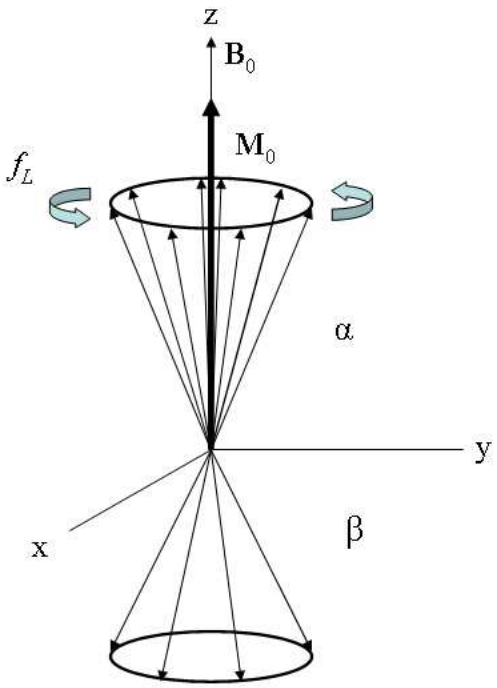


**Figure 4.6** *The thermal equilibrium magnetization* $\boldsymbol{M}_0$ *is created by the individual magnetic moments precessing around* $\boldsymbol{B}_0$.

$\mathbf{M}_0$ is, like the individual magnetic moments, precessing around $\mathbf{B}_0$ with the Larmor frequency $f_L$. Since the RF-field $\mathbf{B}_1$ is able to excite protons to the higher energy state, it is also able to change the direction of the magnetization **M**. This is used in the methods for measuring the relaxation phenomenon.

After the RF-field is turned off ($\mathbf{B}_1 = 0$) the excited protons fall back into the lower energy state and the system returns to thermal equilibrium. During this process an emitted photon will be detected in the receiver coil of the instrument and induce a pulse. Energy will be emitted to the surroundings while protons fall back to the α-state. The magnetization vector **M** will also return to its initial value $\mathbf{M}_0$ along the z-axis. This is known as the *relaxation process*. The magnetic signals associated with the relaxation process follow exponential growth and decay with time constants $T_1$ and $T_2$, respectively.

$T_1$ is the *longitudinal relaxation time*, or the *spin-lattice relaxation time*, and it reflects how effectively the magnetic energy of the system is transferred to or from its surroundings. As the name implies, the relaxation is due to the hydrogen interacting with its surrounding lattice-

structure. A large $T_1$-value corresponds to a slow approach to thermal equilibrium and vice versa. The value for hydrogen normally varies from 0.1 to 10 s [38].

The magnetization **M** will have components along each coordinate axis, $M_x$, $M_y$ and $M_z$, when it is tipped away from its equilibrium condition. Assuming the amount of relaxing nuclei per unit of time is proportional to $M_z$'s offset from its initial equilibrium position, the following equation, known as part of the Bloch equations [42], can be written:

$$\frac{dM_z}{dt} = -\frac{M_z\text{-}M_0}{T_1} \tag{4.10}$$

In order to make it easier to understand the changes and movements of **M**, the fields and magnetizations are placed in a rotating co-ordinate system (x', y', z'), rotating about the z-axis.

Assume that $\mathbf{M}_0$ is tilted into the (x', y')-plane by a $90^{o}_{x'}$ pulse. Thus, the initial condition is that $M_z = 0$ when $t = 0$. Equation (4.10) can be solved by integration:

$$\int_0^{M_Z} \frac{dM_z}{M_z - M_0} = -\int_0^t \frac{dt}{T_1}$$

$$M_z = M_0\left[1 - e^{-t/T_1}\right] \tag{4.11}$$

An analogous solution can be found by assuming that $\mathbf{M}_0$ is tilted by a $180^{o}_{x'}$ pulse. If this is the case, the initial condition is that $M_z = -M_0$ when $t = 0$. By integrating Equation (4.10), another relaxation expression is found.

$$\int_{-M_0}^{M_Z} \frac{dM_z}{M_z - M_0} = -\int_0^t \frac{dt}{T_1}$$

$$M_z = M_0\left[1 - 2e^{-t/T_1}\right] \tag{4.12}$$

The two relaxation processes described by Equations (4.11) and (4.12) will produce different exponential relaxation curves as shown in Figure 4.7. $T_1$ can be measured by the inversion recovery method [41].

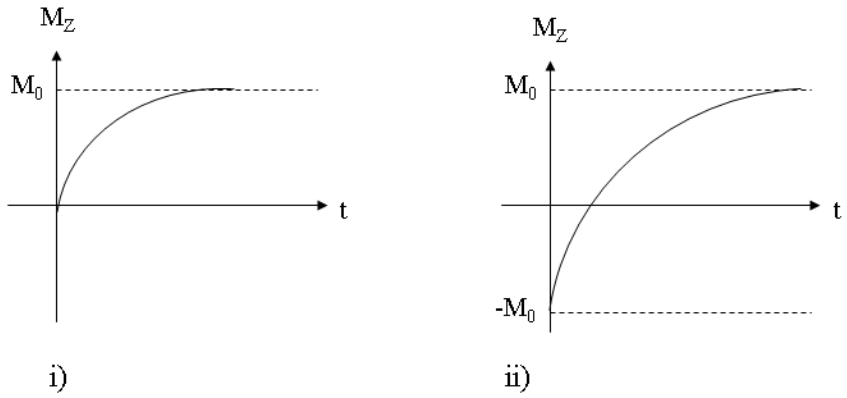


**Figure 4.7** *The relaxation curves of $M_z$ after i) a $90^o_{x'}$ pulse and ii) a $180^o_{x'}$ pulse [38].*

After an RF-pulse, the individual magnetic moments can only be parallel or anti-parallel to the z-axis [38]. Despite of this, a net magnetization can be observed in the (x', y')-plane. Figure 4.8 shows that a net magnetization is created in the y'-direction, $M_{y'}$. This is because the magnetic moments lump together as they precess around $\mathbf{B}_0$, a process called *phase coherence*. Since this process occurs in the (x', y')-plane, it is assumed that the change of $M_{x'}$ and $M_{y'}$ per unit of time is proportional to the instantaneous value. This is described by the following Bloch equations [42]:

$$\frac{dM_{x'}}{dt} = -\frac{M_{x'}}{T_2} \tag{4.13}$$

$$\frac{dM_{y'}}{dt} = -\frac{M_{y'}}{T_2} \tag{4.14}$$

which have the solution

$$M_{x'} = M_{y'} = M_0 e^{-t/T_2} \tag{4.15}$$

where $T_2$ is *the transversal relaxation time*. The phase coherence that occurred as a result of the RF-pulse will dissipate with time. The transversal relaxation process then represents the dephasing of the phase coherence. The relaxation time can vary from 10 µs in solids to 10 s in liquids. Many methods can be used to measure $T_2$, including the CPMG-sequence [43] described in subsection 4.3.2.

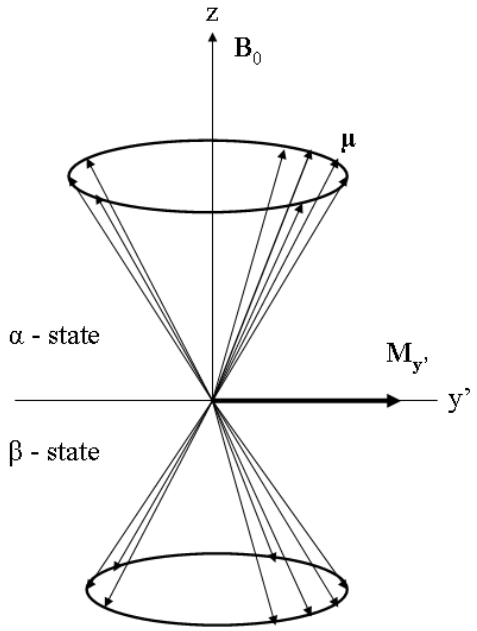


**Figure 4.8** *The magnetic moments are in phase coherence while they precess around* $\boldsymbol{B}_0$*, causing a net magnetization in the y'-direction,* $M_{y'}$ *[38].*

The main difference between the two time parameters is that $T_1$ refers to the exponential growth or recovery of magnetization in the z-direction while $T_2$ refers to the decay of the phase coherence in the (x', y')-plane. $T_2$ is always less than or equal to $T_1$.

## *4.3 NMR in porous media*

The relaxation processes happens as a result of interactions with the surroundings. A single pore volume can be divided into two parts; the thin surface layer *s* of thickness $\delta$ and the bulk volume $V_b$ within the pore, see Figure 4.9. A molecule in the surface layer will have a faster relaxation process than a molecule in the bulk area, as explained in the next subsection. In general, the nuclear magnetic relaxation behaviour of a fluid in a porous media tends to be quite different from that of the fluid in the bulk phase. The values of $T_1$ and $T_2$ are affected by

the properties of the rock fluids, the uniformity of the static magnetic field, variations in pore sizes, differences in magnetic susceptibility, fluid viscosity, diffusion and the presence of paramagnetic impurity ions on the pore walls or in the fluids [41].

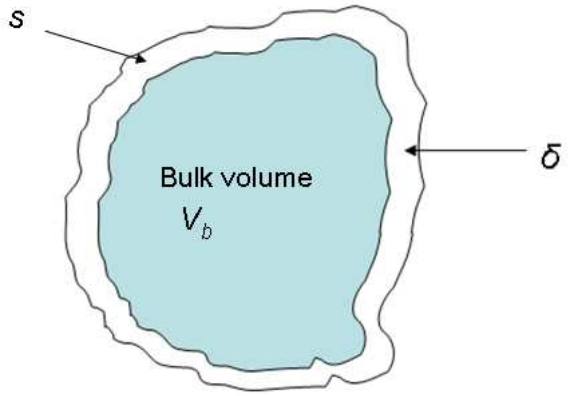


**Figure 4.9** *A pore volume is divided into two parts; the surface layer s of thickness δ and the bulk volume $V_b$. (Not to scale)*

### 4.3.1 Surface relaxation

As mentioned above, the relaxation process of a molecule situated in the surface layer *s* is faster than for a molecule in the bulk area. In order to explain this, the magnetic behaviour of ions must be considered.

The electrons in a material form microscopic current loops that produce magnetic fields of their own. In many materials these currents are randomly oriented and cause no net magnetic field. But in some materials an external magnetic field can cause these loops to become oriented preferentially with the field, so their magnetic fields add to the external field. In this case, the material is magnetized. The atoms of these materials can be diamagnetic, paramagnetic or ferromagnetic.

When electrons orbit a nucleus, their orbital motion produces a magnetic moment. If an external magnetic field $\mathbf{B}_0$ is applied to the system, these electrons can produce a magnetic field in the opposite direction of $\mathbf{B}_0$ [41, 44]. This is the electronic magnetization as opposed to the nuclear magnetic magnetization dealt with in NMR. Since the magnetization is $\mathbf{M}=\chi\mathbf{B}_0$, where $\chi$ is a negative value of the magnetic susceptibility, the magnetization is negative. Such atoms are called *diamagnetic*. Most elements in the periodic table, including copper, silver and gold, are diamagnetic.

If the atoms have unpaired electrons, their net magnetic moment tends to align with the external field $\mathbf{B}_0$ since this is the state of minimum potential energy. If this net increase of magnetic moment more than compensates the diamagnetism, the magnetic susceptibility of the atom will be positive. In this case, the atoms are *paramagnetic*. Examples of paramagnetic materials are magnesium, aluminium and lithium.

When the temperature is lowered below a threshold temperature, the paramagnetic atoms tend to align their magnetic moments with each other and form magnetic domains [41]. Such materials are called *ferromagnetic*, and include iron, cobalt and nickel. When there is no externally applied field, the domain magnetizations are randomly oriented. But when an external field $\mathbf{B}_0$ is present, the different domains tend to orient themselves parallel to the field. The domains that are magnetized in the field direction grow, while those oriented in other directions shrink. The torques that induce these alignments are much stronger than those occurring with paramagnetic materials [44]. A ferromagnetic material is strongly magnetized by the field from a permanent magnet and is attracted to the magnet. A paramagnetic material is also attracted, but not to the same extent.

The magnetic behaviour of the ions will have an impact on the relaxation process, whether they are dia-, para or ferromagnetic. Since the magnetic moments of electrons are stronger than that of nucleus, para- and ferromagnetic ions, such as iron, nickel and manganese can cause a strong surface relaxation. They are collectively referred to as *paramagnetic impurity ions* since they make spins relax very efficiently [45].

### 4.3.2 $T_2$ relaxation measurements

A problem during FID-measurements is that the acquired data is affected not only by the rock properties, but also by the inhomogeneity of the magnetic field over the rock sample. Since magnetic fields in general are not perfectly uniform over the whole system, some spin precessions can get out of phase. Those isochromats that "feel" a stronger field than $\mathbf{B}_0$ will rotate faster than the Larmor frequency, while others will have a slower rotational speed. Thus, the isochromats will disperse and fan out in the (x', y')-plane, causing an unwanted decrease in $M_{x'}$ and $M_{y'}$ as shown in Figure 4.11.

The *CPMG-sequence* (after Carr, Purcell, Meiboom and Gill [43, 46]) can be used to remove these effects of field inhomogeneities on static spins and thus to measure the intrinsic $T_2$ relaxation. This pulse sequence is described by

$$[90^{o}_{x'} - \tau - (180^{o}_{y'} - 2\tau)_n]$$

As seen in Figure 4.10, a CPMG sequence involves applying a series of $180^{o}_{y'}$ pulses to the sample. These pulses produce echoes due to re-phasing of the isochromats. The magnetization **M** will be smaller than the initial magnetization $\mathbf{M}_0$. This phenomenon is called spin echo (or Hahn's echo [47]) and the echo sequence is repeated *n* times to improve statistics. The $180^{o}_{y'}$ pulses are separated by $2\tau$, known as the echo time. Each time an $180^{o}$ pulse is applied, the signal decay due to magnetic inhomogeneity is removed and a single data point is acquired. Echo amplitudes will decrease in time with a characteristic decay rate of $1/T_2$.

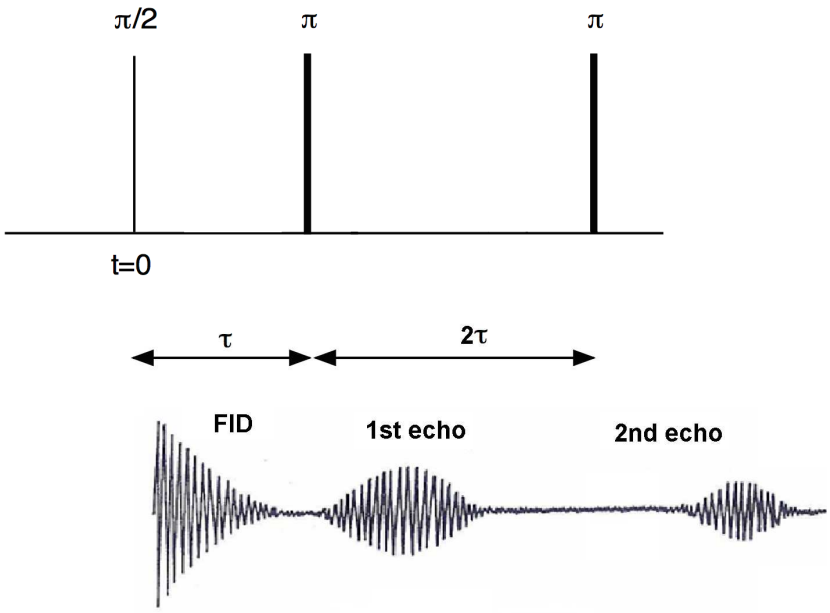


**Figure 4.10** *The CPMG pulse sequence and its associated echoes.*

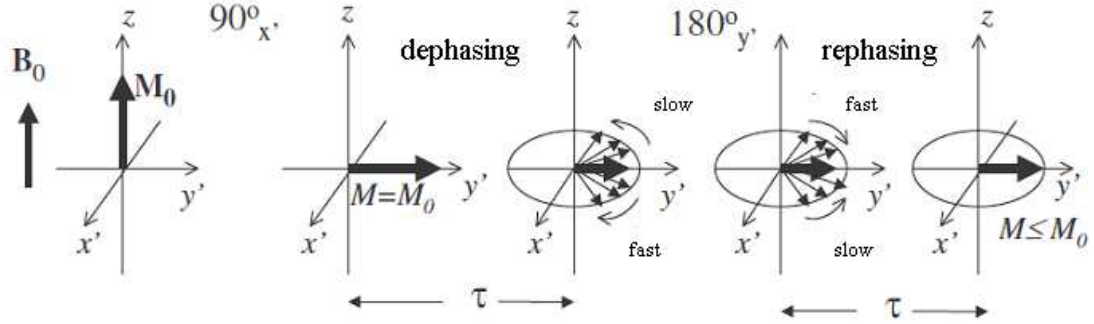


**Figure 4.11** *The CPMG sequence. A* $90^{o}_{x'}$ *pulse tilt* $\boldsymbol{M}_0$ *into the (x', y')-plane. The isochromats will disperse until they are united at* $t = 2\tau$ *by an* $180^{o}_{y'}$ *pulse. This is repeated n times and the magnetization* $\boldsymbol{M}$ *can be measured each time [38].*

### 4.3.3 Self-diffusion

*Self-diffusion* causes molecules to travel during the relaxation time. The average diffusion distance $x$ in three dimensions during $t$ is given by Einstein's diffusion relationship

$$\langle x \rangle = \sqrt{6Dt} \tag{4.16}$$

where $D$ is the molecular self-diffusion constant. This constant reflects the molecule's ability to undergo random Brownian motion. Since $D = 2\text{x}10^{-9}$ $m^2/s$ for water at room temperature [48], the diffusion distance is 110 µm during 1 s for a water molecule. This means that a molecule can travel a significant distance, often a distance of a few pores, during an NMR measurement. Molecules can make contact with the pore walls several times due to their self-diffusion, and each collision can cause an interaction between the water molecules and the paramagnetic ions. This implies that a spin is more likely to relax when travelling through narrow pore throats due to high frequency of surface collisions.

Because the bulk $T_1$ and $T_2$ values for water are long, they usually contribute very little to the measured relaxation rate of brine in a porous medium. The relaxation rates of rocks are dominated by the surface relaxation.

As an example, the effect of diffusion on the spin-echo method in the CPMG-sequence is considered. Spin dephasing due to diffusion causes additional magnetization decay besides the normal $T_2$ relaxation. As the spins diffuse in the pore space of a porous media, they

encounter the pore walls of the solid grains and redirect their random walk path to other directions in the pore space, a process known as *restricted diffusion*. For short diffusion times, corresponding to a diffusion length, $(Dt)^{1/2}$, significantly less than the typical pore size, only molecules within a distance $(Dt)^{1/2}$ from the pore wall will experience the restricted diffusivity [39, 49]. Hence, only a small layer in the pore space is responsible for the reduction in the apparent diffusion coefficient $D$. Figure 4.12 shows an illustration of a restricted diffusion system at short diffusion times. If an internal or external field gradient is present, molecules that moves during the inter-echo time experience different fields in the dephasing and rephasing parts of the sequence, affecting the measured $T_2$.

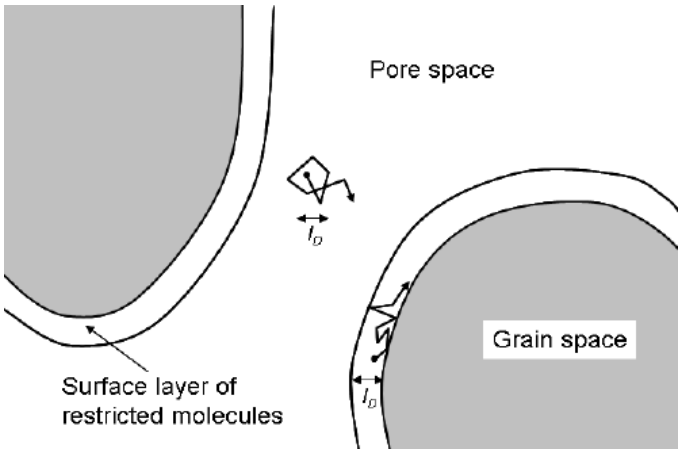


**Figure 4.12** *Illustration of a restricted diffusion system at short times. In the figure,* $l_D = (Dt)^{1/2}$ *[39].*

Imagine a constant field gradient in the z-direction, causing the static field in this direction to be a function of the position

$$B = B_0 + gz \tag{4.17}$$

where $g$ is the strength of the constant field gradient. For non-diffusing spins, the rephasing of the spin-echo will remain unaffected by the field gradient. The deviation from the resonance field felt by the isochromats results in an extra phase angle $\phi$ in the precessing motion of **M** around $\mathbf{B}_0$:

$$\phi = \gamma gzt \tag{4.18}$$

where $\gamma$ is the gyromagnetic ratio.

The phase development of 5 isochromats with different resonance frequency is illustrated in Figure 4.13. The dephased isochromats are exposed to an $180^{o}_{y'}$-pulse at $t = \tau$, causing a rephasing at $t = 2\tau$. This results in a strong spin-echo signal.

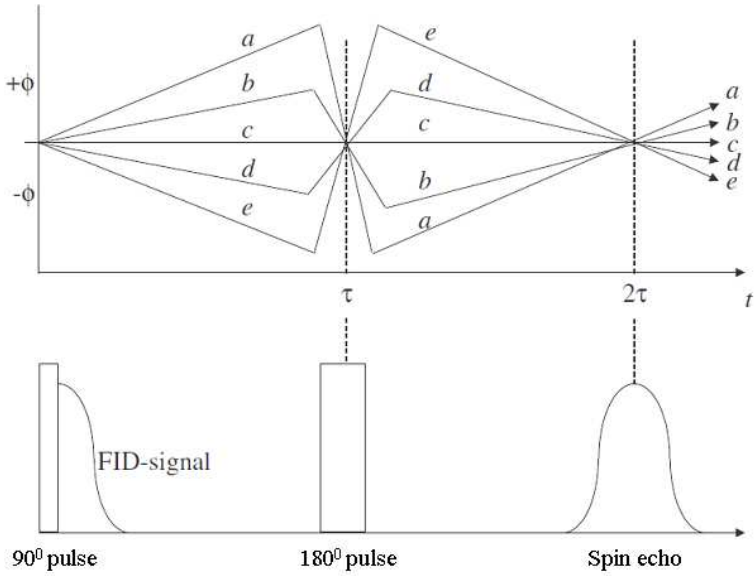


**Figure 4.13** *The development of 5 isochromats as a function of time without diffusion [38].*

The scenario described above changes if diffusion is taken into consideration. Assume that the movement of the molecules causes the two isochromats denoted *a* and *c* in Figure 4.14 to change position at a time $t_1$. The phase correction of isochromats *a* and *c* will terminate, hindering their rephasing at $t = 2\tau$. The net diffusion effect is that less isochromats return to their initial phase at $t = 2\tau$, causing a decrease in the total magnetisation and consequently a weaker spin-echo signal, a process called *echo attenuation*. This affects the exponential relaxation curve, Equation (4.15), and thus the measured $T_2$.

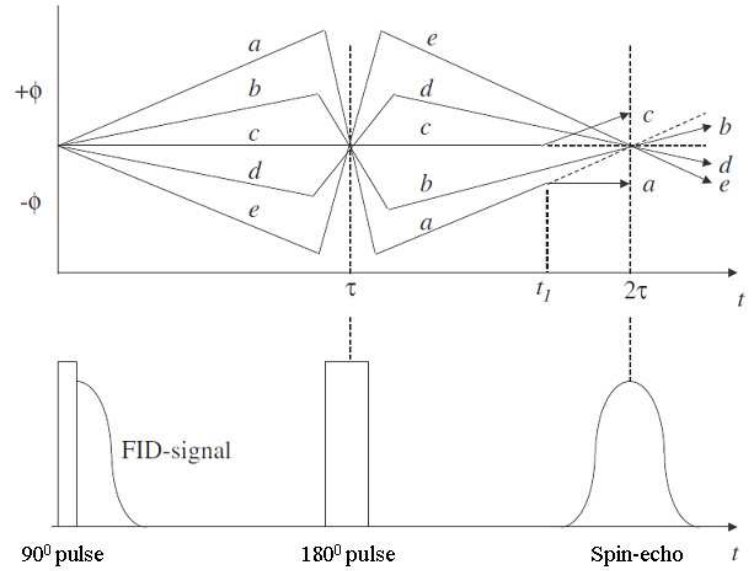


**Figure 4.14** *The development of 5 isochromats with time under the influence of diffusion [38].*

The diffusion involves an additional degradation factor to the transversal relaxation time. This is not the case for the longitudinal relaxation, i.e. diffusion only affects $T_2$, not the $T_1$ measurement, because there are spin-dephasing and rephasing processes involved in the former [41].

The net reduction of the magnetization **M** after the first echo at $t = 2\tau$ can be given by

$$M(z,2\tau) = M_0 \, exp\left[ -\frac{2\tau}{T_2} - \frac{2}{3}\gamma^2 g^2 D\tau^3 \right] \tag{4.19}$$

where $M_0$ is the initial magnetization vector and $D$ is the molecular self-diffusion constant [41]. Equation (4.19) states that the echo pulse is reduced by both the $T_2$ relaxation, the first term of the exponent, and the diffusion represented by the second term. It also states that the effect of diffusion can be controlled through the instrumental parameters $\tau$ and $g$, making it possible to measure the diffusion coefficient. In reality neither a perfectly homogeneous field nor a non-diffusive spin is possible. Thus, when both field gradient and diffusion are present, dephasing will occur and cause further degradation in the $T_2$ magnetization decay as described for CPMG measurements in Equation (4.19). In other words, the NMR signal is attenuated, and the greater the diffusion, the larger the attenuation of the echo signal. Similarly, as the gradient strength is increased in the presence of diffusion, the echo signal attenuates [50]. We often talk about the apparent $T_2^*$ which is the measured $T_2$-value including both effects.

### 4.3.4 Diffusion measurements

As mentioned in the preceding subsection, it is possible to measure the diffusion coefficient $D$ using NMR. The basis for diffusion measurements is provided by the Larmor equation. Equation (4.6) states that the precessing frequency of the individual nuclei is proportional to the strength of the static magnetic field $\mathbf{B}_0$. By applying external gradients, the precession frequency becomes dependent on both the static magnetic field as well as the field gradient [50]. The frequency of the spins becomes

$$\omega(\mathbf{r}) = \gamma \mathbf{B}_0 + \gamma \mathbf{g} \cdot \mathbf{r} \tag{4.20}$$

where the first term is due to the static field $\mathbf{B}_0$ and the second term is due to the applied gradient **g**. As shown in Figure 4.14, diffusing spins do not come back into phase with the

stationary spins, diminishing the echo height. The function of the gradient pulses is to dephase the magnetization from spins that have diffused to a new location.

Since measurements of spin diffusion coefficients with a constant magnetic field gradient had several experimental limitations [50], Stejskal and Tanner [51] proposed the use of pulsed field gradients in 1965. In this technique, known as the pulsed field gradient spin echo (PFGSE) technique, the gradient was considerably reduced during the times at which the RF-pulses were applied and when the echo appeared, i.e. during acquisition. Figure 4.15 shows the PFGSE sequence, containing identical rectangular magnetic field gradients **g** of duration $\delta$. The first gradient pulse produces a precessional phase shift, while the second has the effect of refocusing. If the spins have not undergone any translational motion, the effects of the two applied gradients cancel and all spins refocus. However, if the molecule containing the spin changes position, e.g. because of diffusion, the refocusing is incomplete. The result is a net phase shift of the spin and additional attenuation of the spin echo [45]. This can be used to calculate the diffusion coefficient. Based on the principles of Stejskal and Tanner, spin echo sequences have further developed to avoid several potential experimental errors.

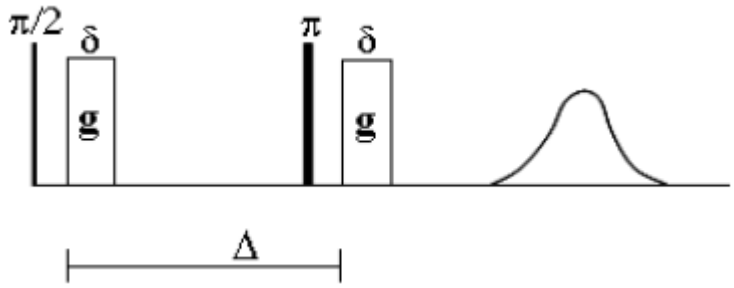


**Figure 4.15** *The basic pulsed field gradient spin echo (PFGSE) sequence proposed by Stejskal and Tanner. δ is the width of the applied gradient pulses [39].*

One of the most important developments was made by Cotts et al. in 1989 [52], stating that the use of bipolar pulsed gradients can greatly reduce the effects of background gradients on the echo attenuation. This assumption is used in the 11-interval bipolar PFGSE sequence created by Sørland et al. [53]. The profiles obtained from this sequence can be used to calculate the diffusion coefficient.

### 4.3.5 Fluid phase discrimination

In order to study multiphase flow in a porous media with NMR, it is necessary to distinguish between the fluids present. Several approaches to distinguish oil from water in porous rocks have been investigated, including techniques based on chemical shift contrasts or spin relaxation contrasts [45]. The use of chemical shift contrasts is beyond the scope of this thesis, and will not be further discussed.

A relaxation-weighted measurement for fluid phase discrimination in porous rocks relies on the difference in $T_1$ or $T_2$ values of the fluids. This difference can be used to eliminate or suppress the signal from one phase, while detecting the signal from the other phase. A relatively straightforward way to distinguish two fluid phases is by introducing substances that enhance proton relaxation contrasts, provided that the substance is soluble in one phase but not in the other. Several substances, mainly paramagnetic ions, have been used to dope water in earlier studies, including $Mn^{2+}$ [54] and $Ni^{2+}$ [55].

An alternative method is to use deuterium oxide, $D_2O$, instead of synthetic salt water [7]. Deuterium is an isotope of hydrogen and $D_2O$ has similar chemical properties as water. Because deuterons have small magnetic moments and thereby hold other resonance frequencies, only protons in the oil are measured during NMR measurements [38].

In this thesis, a diffusion-weighted profile sequence is used to distinguish water signals from oil signals. Equation (4.19) in subsection 4.3.3 demonstrated that the effect of diffusion on the echo attenuation is controllable through the strength of the applied gradient. It is assumed that water and oil used for measurements have significantly different diffusion coefficients $D$, and that $D_{water} > D_{oil}$. The suppression of water signals with increasing gradient strengths in a 100 % water saturated Berea sandstone is shown in Figure 4.16. The water signal is suppressed as the gradient strength $G$ is increased. Note that the gradient strength referred to here is a relative value corresponding to $G$ in Equation (5.2). At $G$ = 25000, the water signal becomes a part of the signal noise. With oil present, the oil signal would not be suppressed to the same extent as the water signal, hence the amount of oil in the core is found. Since the oil signal will be exposed to some degree of suppression, the measured oil intensity values have to be scaled to represent the actual oil saturation of the core.

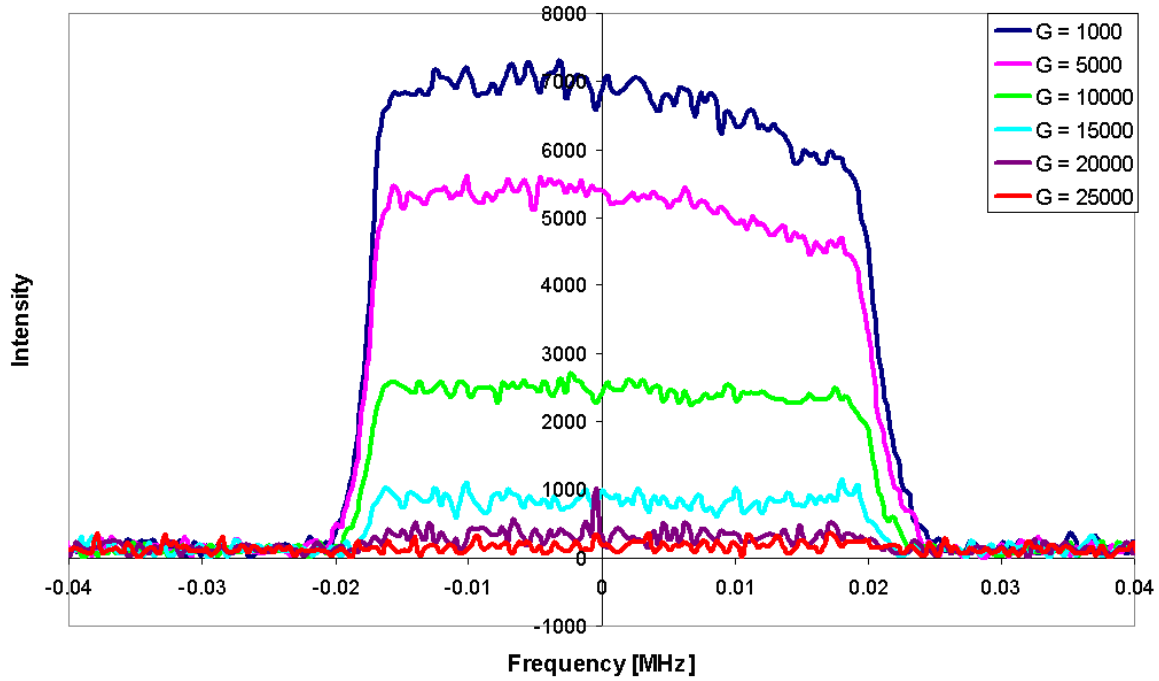


**Figure 4.16** *Suppression of water signals with increasing gradient strengths in a 100 % water saturated Berea sandstone.*

### 4.3.6 Pore size distribution from NMR

The surface relaxation mechanism provides a link to the pore size distribution of rocks [41]. The relaxation rate is inversely proportional to the relaxation time, and it is assumed to be composed of contributions from both the bulk (*b*) and the surface (*s*) area of the pores (see Figure 4.9).

$$\frac{1}{T_i} = \left(1 - \frac{\delta \cdot S}{V}\right)\frac{1}{T_{ib}} + \frac{\delta \cdot S}{V}\frac{1}{T_{is}} \tag{4.21}$$

where the contributions from volume and surface relaxation have been weighted by their respective surface to volume ratios. $T_{is}$ and $T_{ib}$ are the representative relaxation times for the two regions of a pore and $i$ is corresponding to 1 or 2. Since the thickness of the surface layer $\delta$ is considered to be very small, it can be neglected in the first term. Hence, the equation becomes

$$\frac{1}{T_i} \cong \frac{1}{T_{ib}} + \frac{\delta \cdot S}{V}\frac{1}{T_{is}} \tag{4.22}$$

Since the surface relaxation is much faster than the relaxation process in the bulk area ($T_{is} << T_{ib}$), the latter is neglected also. Equation (4.22) becomes

$$\frac{1}{T_i} \cong \frac{\delta \cdot S}{V} \frac{1}{T_{is}} \tag{4.23}$$

Relaxation times strongly depend on pore geometry, the self-diffusion constant $D$ and the strength of all the relaxation processes in the surface layer $\delta$, measured by the surface relaxation factor $\rho = \delta/T_{is}$. This factor is assumed to be independent of pore size [56]. In a fast diffusion regime, as described in detail by Brownstein and Tarr [57], the relaxation times measured represent the ratio of pore volume $V$ and surface $s$, i.e. the diameter of a pore $d$.

$$d = \frac{V}{s} = \rho T_i \tag{4.24}$$

Since each relaxation time is proportional to the pore size in the fast diffusion regime, this is the basis for measuring pore size distribution with the use of NMR. The relationships between pore size and $T_2$ for water are illustrated in Figure 4.17. As shown above, $T_2$ for a pore is proportional to the volume to surface ratio of the pore. A fluid in a large pore will have a longer relaxation time than a fluid in a small pore.

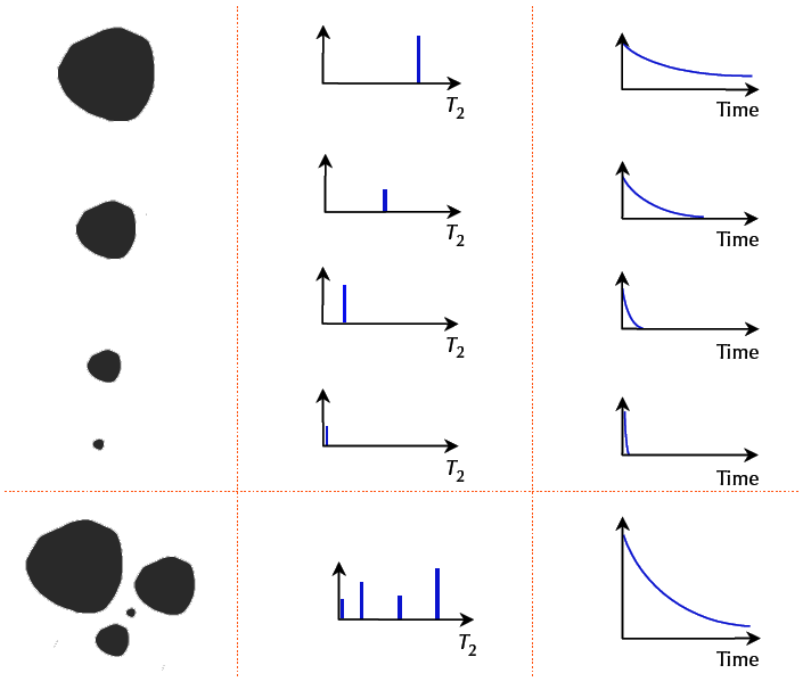


**Figure 4.17** *$T_2$ is proportional to the volume to surface ratio of the pore. A fluid in a large pore has a longer relaxation time than a fluid in a small pore [38].*

Different rock types show different NMR behaviour. In clastic rocks, the $T_2$ distribution is often highly correlated to the pore size distribution. The surface relaxation is lower in carbonates, causing a stronger diffusion coupling between the pores. This diffusion causes some $T_2$ measurements to merge to an intermediate state for different pores so that the total $T_2$ distribution is not reflecting the pore size distribution. Investigations also indicate that $T_2$ distributions for carbonates have a temperature dependent behaviour [41].

In a logging event, $T_2$ is normally measured since it requires less time for measurements than $T_1$ (inversion recovery method). The total magnetization *M(t)* of a porous medium is built up from pores of different sizes. Thus, the measured echo-spectrum from a CPMG-sequence will contain contributions from different $T_2$-values of the type in Equation (4.15).

$$M(t) = M_0 \sum_j^n a_j(T_{2j}) e^{-t/T_{2j}} \tag{4.25}$$

where $a_j(T_{2j})$ represents the contribution from pores with relaxation time $T_{2j}$ and $M_0$ is the initial magnetization. Solving this equation for $a_j$ when *M(t)* is known, is proven to be an inverse ill-posed problem, giving an unstable solution. Still, a linear inversion method has

gained wide acceptance in the NMR community as a solution to the ill-posed problem [41]. If the $T_2$ relaxation time is measured with the CPMG sequence, raw data from *M(t)* can be converted into a $T_2$ distribution as shown to the left in Figure 4.18. The short relaxation time components are frequently attributed to the water abundance in clays. This is shown to the right in Figure 4.18 where the components contributing to the $T_2$ relaxation process are listed.

The shortest $T_2$ values are related to the matrix and possible dry clay present in the rock. Clay Bound Water (CBW) gives higher values, followed by the irreducible water saturation $S_{wi}$ called Bound Volume Irreducible (BVI). The mobile water in the pore is called Bulk Volume Water (BVW) and forms the Bulk Volume Movable (BVM) together with the $T_2$ contribution from the hydrocarbons (HC). BVI and BVM are also marked in the $T_2$ distribution to the left in the figure below. These two areas are divided by a cutoff-value $T_{2co}$, which separates the distribution into the porosity containing the movable fluid (long $T_2$) and porosity containing the irreducible fluid (short $T_2$). In logging, the traditional cutoff-values are 32 ms and 96 ms for sandstones and carbonates respectively [38]. The $T_2$ cutoffs for carbonates are typically much larger than those for sandstones due to a much smaller surface relaxation.

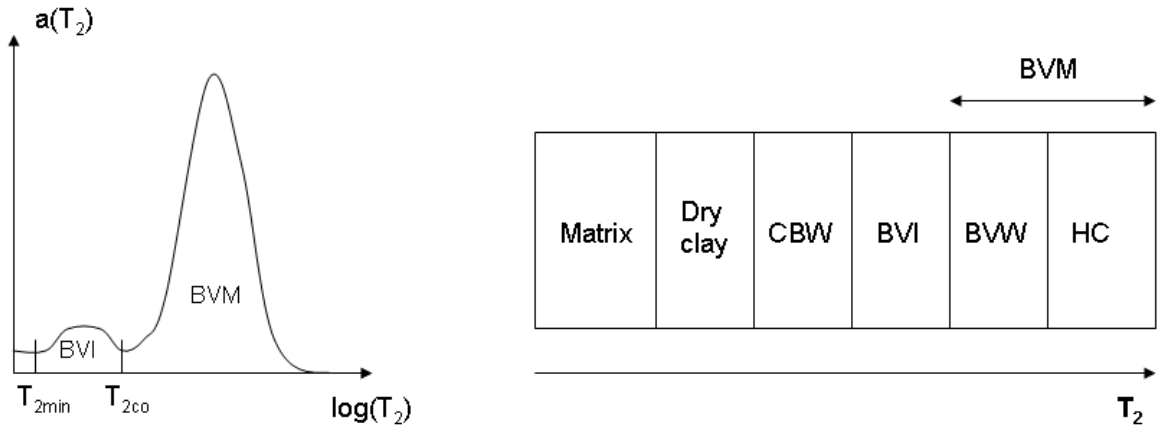


**Figure 4.18** *$T_2$ distribution representing pore size distribution (Left). The components that contribute to the $T_2$ relaxation process (Right).*

The porosity of the rock can be estimated by summing over the distribution of the $T_2$-values.

$$\phi_{nmr} = c \sum_{j=T_{2min}}^{n} a_j(T_{2j}) \tag{4.26}$$

$c$ in Equation (4.26) is a normalization constant. Note that a lower limit $T_{2min}$ is set since the lowest $T_2$-values from CBW are not to be part of the porosity calculation.

The components that contribute to the $T_2$ relaxation process can be used to estimate the absolute permeability by using the Coates equation [58]:

$$k = \left( \frac{\phi_{nmr}}{C} \right)^4 \left( \frac{BVM}{BVI} \right)^2 = \left( \frac{\phi_{nmr}}{C} \right)^4 \left( \frac{\phi_{nmr} - BVI}{BVI} \right)^2 \tag{4.27}$$

## *4.4 Pulse sequences*

### 4.4.1 1D profile sequence

1D profiles, i.e. imaging along one dimension, can be obtained using a *profile pulse sequence* [59]. Since it is based on a spin-echo sequence, described in subsection 4.3.2, the profile sequence produces a proton density and $T_2$-weighted profile. During measurements, a gradient is applied along the long axis of the core, providing a projection of the core plug along that axis.

In a homogeneous magnetic field all nuclear spins within a sample will resonate at the same frequency. Applying a pulsed magnetic field gradient to a sequence causes nuclear spins in different parts of the rock sample to resonate at different frequencies, providing important spatial information. This is illustrated in Figure 4.19, showing a sample containing different amounts of water in three different zones, A, B and C. The ratio of nuclei density in the zones is 3:2:1. The spins from all zones resonate at different frequencies as indicated in the figure, and the resulting signal is the sum of all three frequencies (A + B + C). If the frequency variation as a function of position is known, the spatial variation in spin density may be established via a process known as Fourier transform. This process yields the frequencies present in the time domain data, the amplitude variation reflects the variation in the number of spins in each zone. In practice, pulsed gradients are used instead of constant gradients to avoid that the RF-pulse becomes bandwidth limited or slice selective. The resolution of the 1D profile is dependent both on the gradient strength and the application time $\delta$.

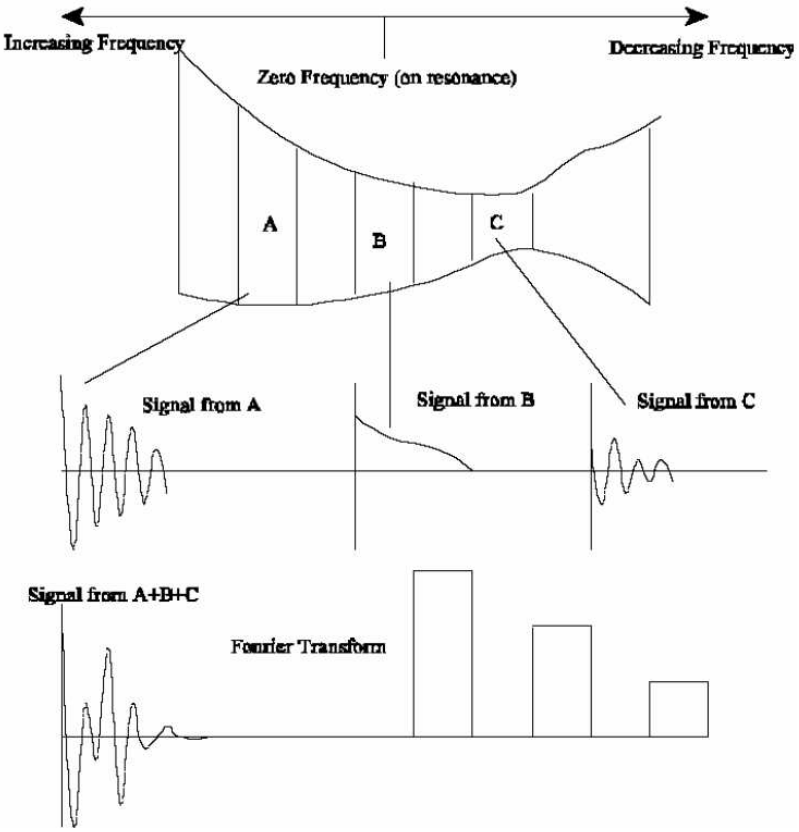


**Figure 4.19** *The result of applying a magnetic field gradient on a sample containing water in three different zones, A, B and C. The variation in spin density is found by Fourier transform [59].*

Since the 1D profile pulse sequence is based on a regular spin echo experiment, it consists of a 90$^{o}$ pulse followed by a gradient pulse **g**, an 180$^{o}$ pulse and a second gradient pulse, known as the readout gradient $\mathbf{G_{read}}$. The echo acquired during $\mathbf{G_{read}}$ is Fourier transformed to produce the final 1D profile.

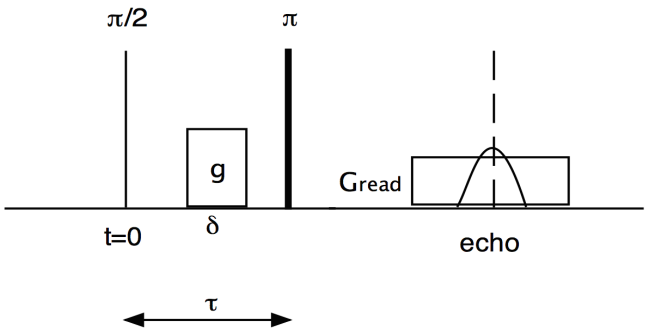


**Figure 4.20** *The 1D profile sequence. $G_{read}$ is the readout gradient.*

### 4.4.2 Diffusion-weighted profile sequence

In order to separate oil and water in the measured profiles, a *diffusion-weighted profile sequence* is used. Water normally has significantly higher self-diffusion than oil. By applying sufficiently large gradients the water signal may be suppressed and the signal from oil remains. Hence, the signal from water is obtainable by subtraction from the total signal [60]. It should be noted that the oil signal will also be suppressed with increasing gradient strengths, but not to the same extent. The diffusion-weighted spin echo profile sequence used in this thesis consists of two parts, one profile part and one diffusion part. A schematic representation for the pulse sequence is shown in Figure 4.21.

As indicated in subsection 4.3.1, the magnetic susceptibility tends to change throughout a sample. Thus, a distribution of background gradients may cause excessive echo attenuation. Bipolar gradients can be applied to reduce these cross term effects [52]. The profile part of the current diffusion weighted sequence is the same as in the simple spin-echo case, while the diffusion part is based on the 11-interval spin echo sequence with bipolar gradients introduced by Sørland et al. [53]. During measurements, it is assumed that all molecules are experiencing a constant internal magnetic field gradient. The validity of this assumption is at its highest when the pulse sequence is applied with the shortest duration. The 11-interval sequence is the shortest bipolar pulsed field gradient spin echo (PFGSE) sequence which is possible to construct when the aim is to reduce the effects of diffusion in the presence of strong internal magnetic field gradients. Thus, the assumption mentioned above is at its highest validity, the diffusion time is reduced to a minimum, and less unwanted echo signal is generated.

The 11-interval sequence is, as mentioned in subsection 4.3.4, an extension of the Stejskal Tanner spin echo diffusion sequence [51]. The difference is that each diffusion gradient is split into a pair of bipolar gradients and separated by a $180^{o}$ pulse. This has the effect that the polarity of the bipolar gradient pair remains the same. However, the above-mentioned constant internal background gradient is also split in two parts by the $180^{o}$ pulse. Thus, the decay due to diffusion in the internal gradient is cancelled out.

The sequence can be seen as the spin echo analogue to the 13-interval stimulated echo sequence given by Cotts et al. [52] and the associated echo attenuation, corrected for

sinusoidal shaped gradients, is given in Equation (4.28) [53]. Since $D_{water}$ is significantly larger than $D_{oil}$, the water signal undergoes a higher degree of attenuation as the gradient strength $g$ is increased. Hence, the two fluid signals are discriminated.

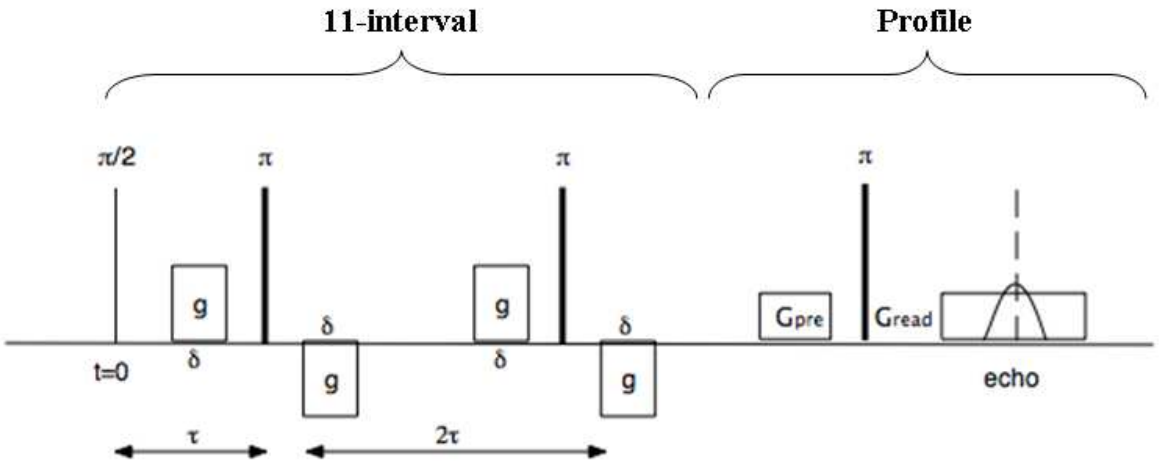


**Figure 4.21** *The diffusion-weighted profile sequence is based on the 11-interval spin echo sequence and the profile sequence.*

$$ln\left(\frac{M}{M_0}\right) = -\gamma^2\left(\frac{16}{\pi^2}\right)Dg^2\delta^2\left(\frac{3\tau}{2}-\frac{\delta}{8}\right) \tag{4.28}$$

# 5 Capillary pressure curve from centrifuge and NMR

Nuclear magnetic resonance has provided an additional means of measuring saturation in conjunction with capillary pressure determination. Studies by Baldwin et al. [5] in 1991 reported that it was possible to obtain capillary pressure curves by combining our knowledge of NMR and the centrifuge method. This was later confirmed by Chen & Balcom [6]. Recent studies by Green et al. [7] present the first attempts at a commercial application of the technology. The technique uses a centrifuge to create a distribution of fluids and capillary pressures in a rock core before a NMR method is used to accurately measure the saturation in the rock. In order to obtain successful results, it is necessary to combine our knowledge of conventional fluid flow experiments, centrifuge experiments and nuclear magnetic resonance.

## *5.1 Experimental descriptions*

The new method consists of a combination of three different experiments; conventional fluid flow and saturation methods, centrifuge and NMR. In order to unite these into one experiment, thorough preparatory work had to be done and all potential errors had to be considered. Both air-brine and oil-brine capillary pressures were measured, giving three experimental procedures for establishing the primary drainage capillary pressure curve. An alternative method, air-brine procedure II, was tested prior to the oil measurements in an attempt to lower the experimental time. This was later implemented in the oil-brine procedure. The procedures are explained in detail in the following subsections.

### 5.1.1 Air-brine procedure I:

1. Porosity and permeability were measured.
2. The sample core was cleaned and dried until constant weight was achieved.
3. The dry core was vacuumed and then saturated with synthetic salt water, i.e. brine. See Table A-1 in Appendix A for reference on the brine composition.
4. A reference NMR measurement with the 1D profile sequence was performed on the fully brine-saturated core plug. This reference measurement ($M_0$) was used to determine brine saturation after centrifugation.
5. All centrifuge bucket weights were measured. These had to be, according to the centrifuge requirements, within ± 0.3 g of each other, in order to avoid instability during rotation.

6. The core was centrifuged until an equilibrium brine distribution was obtained within the pores of the rock. It was assumed that an equilibrium condition was obtained after 24 hours of centrifugation.
7. The core was removed from the centrifuge, weighed and transported to the NMR instrument. Here, the hydrogen intensity ($M_a$) was measured by the same sequence as in step 4.
8. Steps 4 – 7 were repeated two times with various rotational speeds after the core was re-saturated with brine by conventional fluid flow procedures.
9. A primary drainage capillary pressure curve was obtained for the sample core by combining the NMR results of all three measurements.

### 5.1.2 Air-brine procedure II:

In an attempt to lower the experimental time, a second procedure was tested on one of the sample cores. This alternative method was very much the same as the original one, except for a change in step 8. Now, the plug was placed directly into the centrifuge after NMR measurements, i.e. it was not re-saturated for each rotational speed. In theory, this should also provide more accurate saturation values due to the consistency of the fully saturated profile. Hassler and Brunner [3] state that if the centrifuge is stopped and then brought up to its previous rotational speed, more liquid is expelled from the core due to redistribution of fluids. However, Green et al. [9] conclude that the redistribution is insignificant in the time required to acquire a NMR profile. The issue of fluid redistribution is further discussed in subsection 6.7.6.

### 5.1.3 Oil-brine procedure:

1. Porosity and permeability were measured.
2. The sample core was cleaned and dried until constant weight was achieved.
3. The dry core was vacuumed and then saturated with synthetic salt water, i.e. brine.
4. A reference NMR measurement with the 1D profile sequence was performed on the fully brine-saturated core plug. This reference measurement ($M_0$) was used to determine brine saturation after centrifugation.
5. The core was placed in the centrifugation bucket. The bucket was then filled with a mineral oil, Marcol 82. See Table A-2 in Appendix A for reference on the

properties of Marcol 82 [61]. Great care was taken to prevent the presence of air in the bucket.

6. All buckets were heated at a constant temperature of 35 $^{o}$C with open ventilators to prevent formation of cracks due to fluid expansion.
7. The bucket weights were measured. These had to be, according to the centrifuge requirements, within ± 0.3 g of each other to avoid instability during centrifugation.
8. The core was centrifuged at the lowest chosen rotational speed until an equilibrium oil-brine distribution was obtained within the pores of the rock.
9. The core was removed from the centrifuge, weighed and transported to the NMR instrument. Here, measurements were performed with both the 1D profile sequence ($M_{tot}$) and the diffusion-weighted profile sequence ($M_{oil}$).
10. Steps 7 – 9 were repeated with increasing rotational speeds. A refill of mineral oil was necessary in most cases to obtain constant weights.
11. A primary drainage capillary pressure curve was obtained for the sample core by combining the NMR results of all three measurements.

### 5.1.4 Cleaning process

Some of the cores used in this thesis had to be cleaned before any other measurements could be carried out. For this objective, *flow-through core cleaning processes* [62] were executed at room temperatures. Each core was placed in a Hassler-sleeve core holder and solvents were injected under pressure into the core. Anderson [63] found that toluene proved to be a very effective solvent when combined with methanol, which is why these solvents were selected for the current cleaning process. The solvents were injected in a three step process; first 7-8 PV of toluene at low injection rates, followed by a buffer consisting of a 50/50 mixture of toluene and methanol, before the system was reversed and flushed with 3 PV methanol. Finally, synthetic brine was injected until the production of methanol ceased. The cleaning process is an important part of any core analysis, and should not be underestimated. It has been proved that ineffective cleaning has two effects on the capillary pressure curves [64]; the shape of the curve is altered due to a change in the wetting angle and the curve is shifted towards higher water saturation $S_w$ due to water trapping.

### 5.1.5 Porosity measurements

After the cleaning process, all cores were dried in a heat oven until constant weights were measured. Then, the dry cores were evacuated in a vacuum chamber. Water was introduced into the chamber when a pressure below 1 mbar was reached and pressured to ensure complete saturation. By measuring the dimensions of the cores and the weights before and after saturation, the pore volumes were obtained by the *saturation method* [12]. Hence, porosities could be estimated from Equation (2.1).

### 5.1.6 Permeability measurements

As described in Chapter 2.2, the absolute permeability *K* of a porous media is defined through Darcy's equation (see Equation (2.3)). Since all other parameters are known, the permeability was estimated by flowing synthetic brine at constant rates while measuring the differential pressure across the core. Darcy's equation is only valid when the following conditions are fulfilled [10]:

1) The flow angle must be constant, i.e. a horizontal position of the sample is essential.
2) The fluid must be incompressible.
3) No reactions, or ion exchange, can occur between the fluid and the rock solids.
4) The pore space must be 100 % saturated with one fluid.
5) Laminar fluid flow.

The instrument set-up for permeability measurement is shown schematically in Figure 5.1.

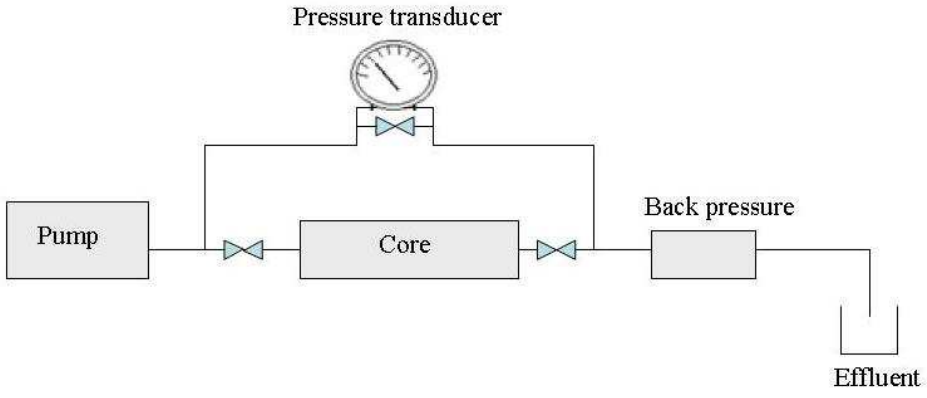


**Figure 5.1** *Experimental setup of permeability measurements.*

After centrifugation and NMR measurements, the cores were re-saturated by brine injection with back pressure. Great care was taken to prevent air in the sample, as this would result in a lack of fluid continuity. Khilar et al. [65] found that if the water salinity falls below a threshold value, clay particles are released from the pore walls resulting in a reduction in core permeability. This is why filtered synthetic salt water, or brine, was used in this thesis. See Table A-1 in Appendix A for further reference on composition of synthetic salt water.

To quantify the uncertainty of the measurements, the potential errors must be addressed. As mentioned above, air in the sample would result in a lack of fluid continuity followed by erroneous porosity estimations. To prevent this from happening, back pressure was used during all flow experiments and the saturated core weights were compared. A slide caliper was used to measure core dimensions. This, together with the fact that the cores were not always cylindrical, could cause errors concerning the measured dimensions. To avoid this, several measurements were done, before a mean value was calculated and used in the subsequent calculations.

### 5.1.7 Centrifuge

Prior to measuring a saturation profile by NMR, a fluid distribution was achieved by centrifuge. In this thesis, all centrifuge experiments were executed in a Beckman L8-55 M/P Ultracentrifuge equipped with a Type PIR 16.5 rotor designed to centrifuge three rock core samples. The outer rotation radius $r_2$ of the centrifuge was 9.11 cm. Custom made centrifugal procedures by Norsk Hydro [66] were closely followed to obtain good results and prevent instrument damage. The sample cores were kept at vacuum conditions and 35 $^{o}$C during centrifugation, which is the temperature of the NMR instrument. Standard and inverted buckets can be used for drainage and imbibition centrifugation, respectively. Figure 5.2 show cross sectional sketches of the two buckets, demonstrating their differences. The inverted bucket is, as the name implies, an inverted version of the standard bucket, i.e. the rock core is placed at the opposite end. Since drainage processes were performed in this thesis, the standard buckets were used. Only one of three buckets used during centrifugation contained a rock core sample. Great care was taken to ensure that all three buckets weighed within 0.3 g of each other, preventing instability during centrifugation.

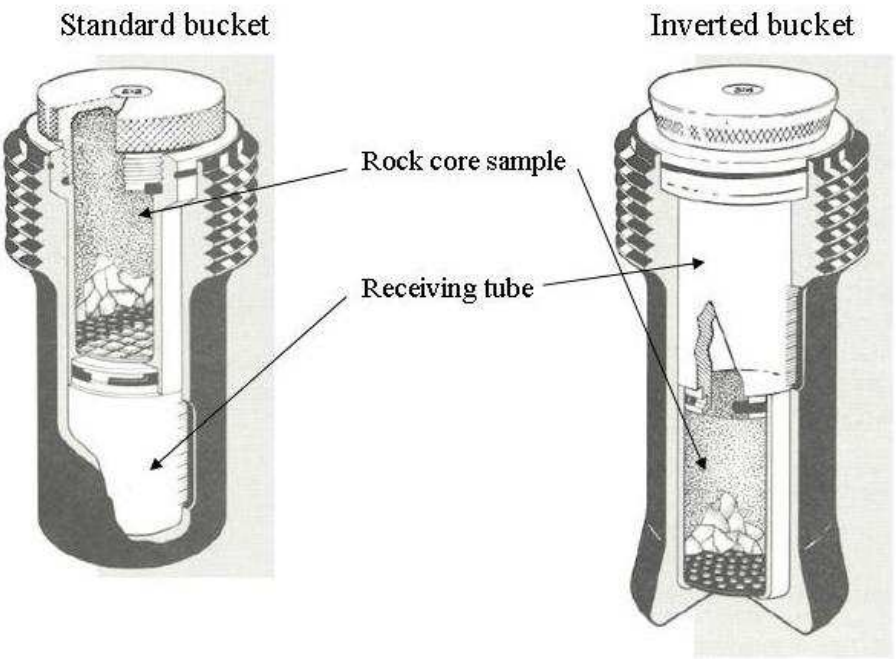


**Figure 5.2** *Cross sectional sketches of the standard and inverted buckets used during centrifugation. From Norsk Hydro [66].*

The ultracentrifuge is controlled by the *Centas Centrifuge Automation System* by Reslab, providing accurate measurements. It is also equipped with a stroboscope and a high-speed camera unit. The stroboscope consists of two parts; a flash unit and a control unit. Each time a rotor passes over a photocell it triggers a strobe flash lamp, positioned under the rotor chamber, emitting a flashing light observable from the quartz window at the chamber door. Simultaneously, the strobe control unit is used to "stop" a bucket directly under the window for each flash. At each flash, the camera unit photographs the receiving tube of the bucket and registers the amount of produced fluids. The information is transferred to a computer and processed by the Centas system before shown in a production profile. This automated data acquisition system provides high resolution data on the amount of produced fluids based on pixels, as shown in Figure 5.3, making it easier to predict whether the equilibrium condition is obtained or not during centrifugation.

As mentioned earlier, there is a high degree of uncertainty concerning the equilibrium time during centrifugation. Slobod et al. [67] concluded that samples with permeabilities in the range of 15 – 100 mD needed 1 to 2 hours to reach an equilibrium condition, while Omoregle [68] concluded that a minimum of 24 hours of centrifugation was needed. In this thesis, it is assumed that an equilibrium condition is obtained after 24 hours of centrifugation.

The centrifuge speeds used in this thesis were based on experience from both earlier and ongoing measurements and the permeability of the sample cores. In general, low permeability yield higher rotational speeds.

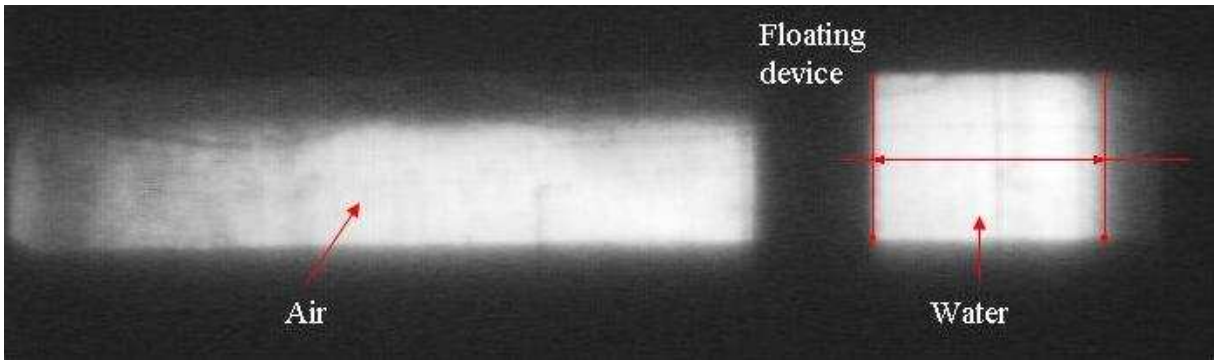


**Figure 5.3** *Example showing how the Centas system provides information about the amount of produced fluid (i.e. water in this case) from the high-speed photographs.*


**Figure 5.4** *The Beckman L8-55 M/P Ultracentrifuge equipped with the Centas camera unit.*

### 5.1.8 NMR measurements

All NMR measurements in this thesis were performed on a 12 MHz Maran DRX NMR instrument delivered by Resonance Instruments Inc. The spectrometer included a set of gradient coils, delivering up to 225 Gauss/cm in applied magnetic field gradient strength. The instrument was operating at 35 $^{o}$C and ambient pressure. The 1D profile sequence was utilized both in air-brine and oil-brine measurements, while the diffusion-weighted profile sequence was used exclusively for oil-brine systems. In addition, CPMG measurements were performed.

The resulting CPMG data was processed using Resonance Instruments Inverse Laplace software, WinDXP, which inverts the multiexponential attenuation data to a $T_2$ distribution data set.

A variety of system parameters were used during the NMR measurements. These parameters are system dependent, i.e. they vary from system to system. As the experimental work in this thesis progressed, it became evident that changes in parameters were needed. Hence, two sets of system parameters were used during air-brine measurements. For oil-brine systems, the 1D profile sequence was used both prior to and after centrifugation. In addition, the diffusion-weighted profile sequence was utilized after centrifugation. Some NMR parameters are summarized in Table C-1 in Appendix C.

To prevent fluid evaporation and other ways of fluid loss, all surfaces of the sample cores were wrapped in plastic foil after being removed from the centrifuge and weighed. The plastic foil was kept on during all NMR measurements. It was emphasized that the foil was wrapped so that the bottom end of the core remained flat; assuring that it was located correctly relative to the magnet centre in the NMR instrument.


**Figure 5.5** *The 12 MHz Maran DRX NMR instrument delivered by Resonance Instruments.*

## *5.2 Establishing the capillary pressure curve*

It is possible to use the achieved results to establish a capillary pressure curve for the core in question. This procedure consists of four main points; obtaining brine intensity values, verifying the position of the core in the NMR signals, calculating the capillary pressure and water saturations, and gathering the experimental data into one capillary pressure curve.

### 5.2.1 Obtaining brine intensity values

*Air-brine measurements*

Two NMR measurements were carried out on the cores for each centrifuge speed that the sample cores were exposed to; one reference intensity measurement $M_0$ at 100 % brine saturation and one measurement $M_a$ after centrifugation. Prior to the measurement of $M_0$, the core had to be placed in a heating cabinet at 35 $^{o}$C. The 1D profile sequence, as described in subsection 4.4.1, was used for both measurements in the air-brine experiments. It was emphasized that the same parameters were used at both occasions. For air-brine measurements, the brine intensity values were directly measured in the core sample. Hence, no further modifications were needed and the data was ready for further calculations.

*Oil-brine measurements*

The introduction of oil into the core leads to a more sophisticated approach to obtain the brine saturation of the core. In conformity with the air-brine measurements, a reference intensity measurement $M_0$ was measured with the 1D profile sequence. An analogous total intensity measurement $M_{tot}$ was performed after centrifugation. In addition, a diffusion weighted profile sequence with bipolar gradients was used to suppress the water signals from the sample core, as described in subsection 4.3.5. By doing this, the oil signal $M_{oil}$ was obtained. Since the oil intensity values were exposed to some degree of suppression, they had to be multiplied by a factor of 1.78. This factor was found by calibration on a Baskarp sand sample with known amounts of oil and water. The water intensity values after centrifugation $M_a$ was then calculated by subtracting the oil intensity values from the total intensity, i.e. $M_a = M_{tot} - M_{oil}$.

An example can be used to illustrate the method for obtaining the water signal. Figure 5.6 shows a loose sand sample containing water and oil in separate layers. The total signal $M_{tot}$ contains the intensity of both phases while the red curve indicates the amount of oil in the total signal. The oil signal has been calibrated to match the total signal in the layer where only oil exists. As mentioned above, the water signal $M_a$ is the remaining area below the total signal. The same procedure is used to obtain the water signals after oil-brine centrifugation.

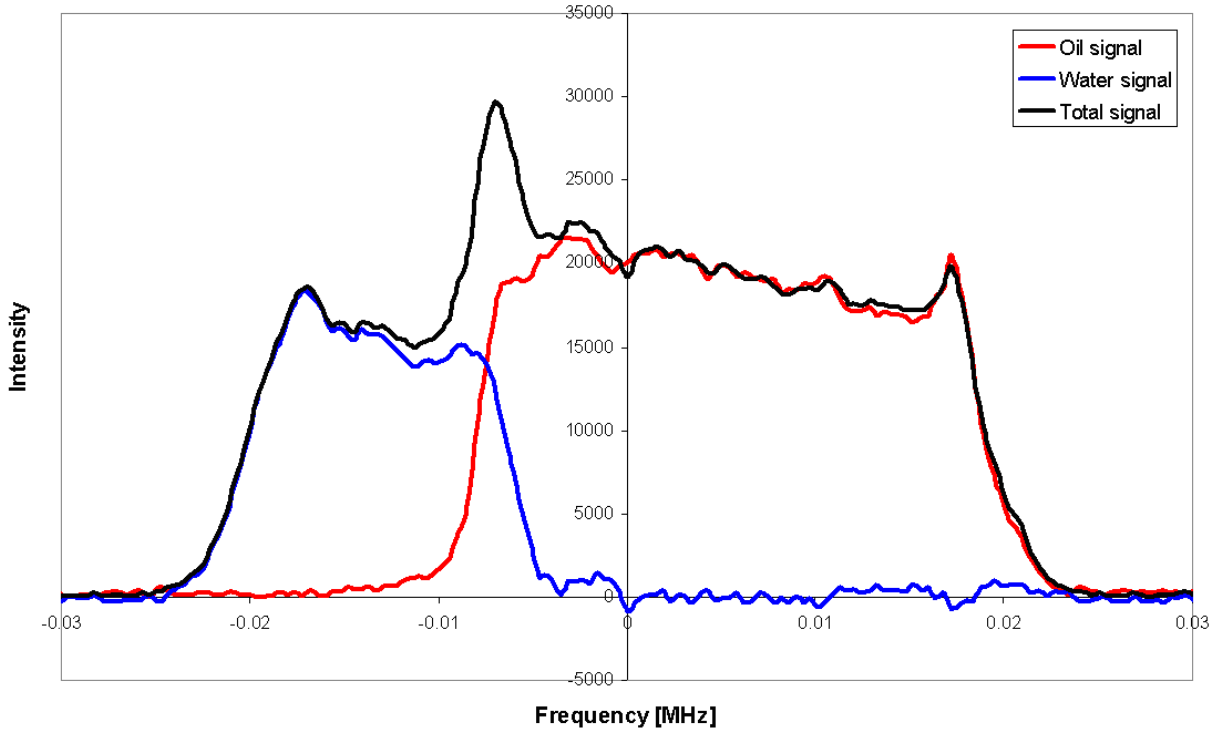


**Figure 5.6** *Measured signals of a sand containing separate parts of oil and water. The water signal is calculated from the total and the oil signal.*

### 5.2.2 Positioning of the core

Once the brine saturation values ($M_a$) are obtained, it is important to *locate the position of the sample core in the intensity profile*. Figure 5.7 shows a typical saturation profile obtained with the 1D profile sequence, described in subsection 4.4.1, on a Berea sandstone centrifuged with air and brine. In order to locate the position of the core in the saturation profile accurately, the x-axis must be converted into a known unit, e.g. centimetres (cm). A formula relating resolution, gradient strength and frequency can be deduced from the resonance condition in Equation (4.6).

$$\Delta f = \frac{\gamma}{2\pi}\Delta B = \frac{\gamma}{2\pi} g \Delta x \Rightarrow \Delta x = \frac{\Delta f}{(\gamma / 2\pi) g} \tag{5.1}$$

where $\Delta f$ is the incremental frequency on the x-axis (in Mhz) and $\Delta B = g\Delta x$. To illustrate the application of Equation (5.1), the air-brine centrifuged Berea sandstone is used as an example. Since $\Delta x$ is influenced by the NMR system parameters used during each measurement, the parameters in Table C-1 in Appendix C should be used as a reference. In the Berea case, $\Delta f$ is going from 488 to 488*SI, where SI is the number of points acquired following the pulse, i.e. SI = 2048. $\gamma/2\pi$ = 4256.7 Hz/Gauss is a constant containing the gyromagnetic ratio of hydrogen. The gradient strength $g$ is

$$g = \frac{G \times 225 Gauss \times cm^{-1}}{32768} \tag{5.2}$$

where $G$ represents the input strength of the applied gradient, e.g. $G$ = 260, and the maximum gradient field achieved by the NMR system is 225 Gauss/cm. 32768 is a constant value for a 16 bit system. The factors in the denominator in Equation (5.1) are calculated as $(\gamma/2\pi)*g$ = 7599.4 Hz/cm in the Berea measurements. Hence, the resolution of the x-axis is

$$\Delta x = \frac{488}{7599.4} cm = 0.0642 cm \tag{5.3}$$

The measured intensity can be plotted as a function of $\Delta x$ as shown in Figure 5.7ii. Since the length of the core is known, 5.04 cm in this case, it can be correlated with the measured

intensity values. Note that $\Delta x$ must be recalculated if a change is made in the system parameters.

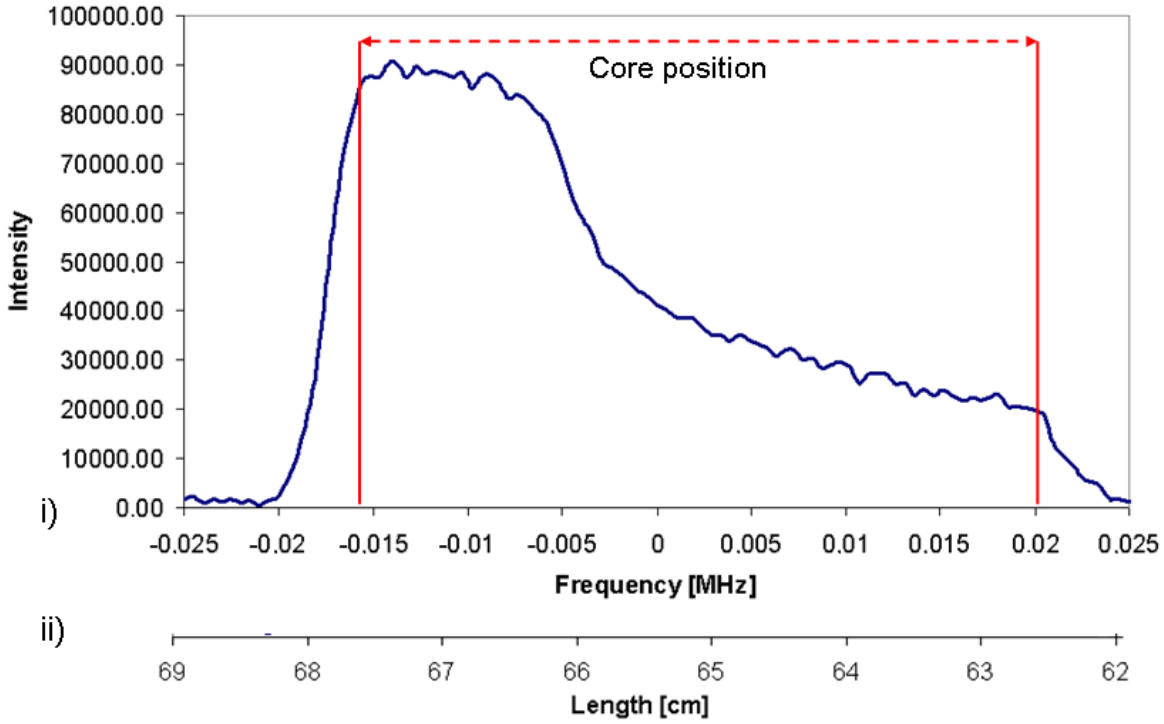


**Figure 5.7** *Typical saturation profile obtained by the profile sequence on a centrifuged Berea sandstone. The position of the core is confirmed by changing the unit of the x-axis from i) frequency to ii) relative length.*

### 5.2.3 Calculate capillary pressures and saturations

The main advantage of this method is that it allows for many capillary pressure-saturation points to be acquired for each centrifuge speed. Once the position of the core in the measured intensity profile is established, the intensity values to be used in further calculations are known. Based on Equation (3.7) derived in Chapter 3.3, the capillary pressure is found at each position down the rock at hydrodynamic equilibrium. It should be noted that $r$ and $r_2$ in the capillary pressure expression are, as illustrated in Figure 3.2, the radius from the centre of centrifugation to a gradual position $x$ in the core and the outlet end of the core, respectively. Thus, the radial distances used during calculation of capillary pressures are $r = r_1 + x$ and $r_2 = r_1 + L$, where $L$ is the length of the core. The increment of $x$ is $\Delta x$, as calculated in the previous subsection.

Prior to centrifuging, while the core is 100 % brine saturated, a reference saturation profile $M_0$ is measured. A 0 % saturation level will yield no NMR signal as there is no hydrogen present. Therefore, dividing the measured profile after centrifugation ($M_a$) by the 100 % saturated profile gives a quantitative saturation level versus position.

$$S_w = \frac{M_a}{M_0} \tag{5.4}$$

The capillary pressure at each point is plotted as a function of the saturation to create a capillary pressure curve.

### 5.2.4 Data collection

Although it would be ideal to acquire the complete capillary pressure curve at one centrifuge speed, operational and NMR resolution restrictions may prevent this. Thus, a minimum of two centrifuge speeds must be run [7].

Depending on the accuracy in determining $\Delta x$, a number of irregular saturation values can occur when the capillary pressure curve for a certain rotational speed is plotted. This is illustrated in Figure 5.8. These values originate from edge effects when $M_a$ is compared to $M_0$ and are omitted from the final $P_c$-curve.

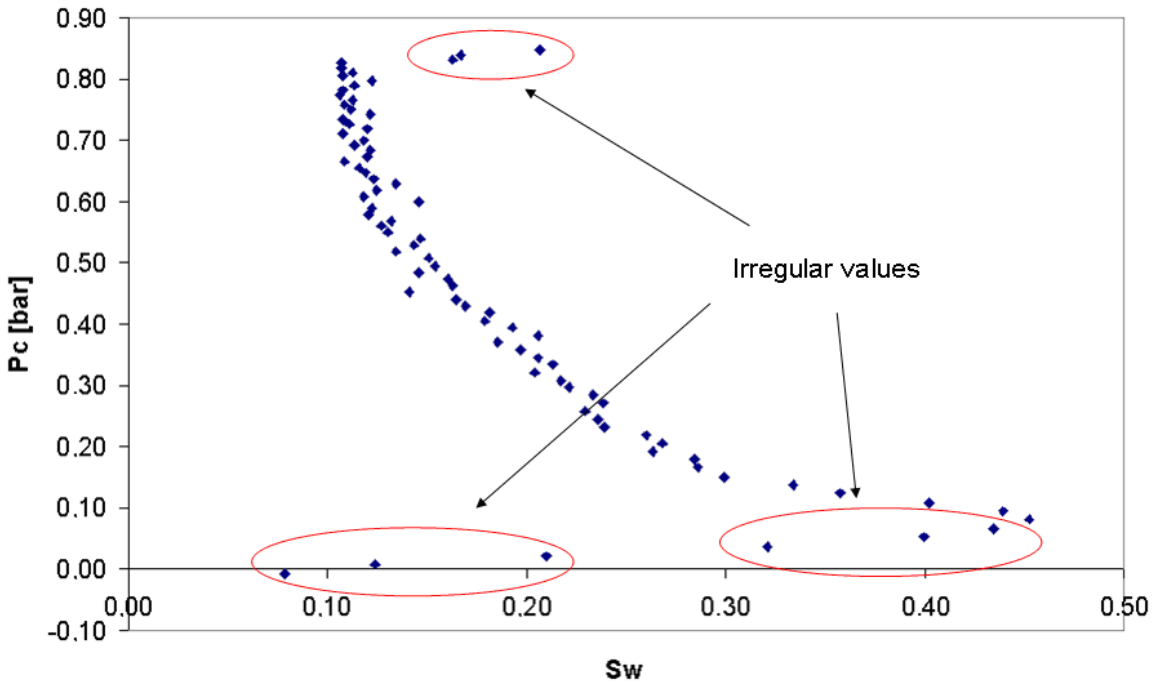


**Figure 5.8** *Capillary pressure-saturation plot based on raw data. Irregular values are observed at the edges of the curve.*

All values for capillary pressure, $M_0$ and $M_a$ were smoothened by a *5 point technique*, i.e. an average of 5 neighbouring values gave one point on the capillary pressure curve.

### 5.2.5 Calculation errors

The most important property of a system is the accuracy of its measurements. Thus, it is very important to estimate the uncertainties of the experiments. Two types of standard uncertainties are distinguishable:

- *Type A uncertainty* is based on statistical analysis of a series of repeated measurements.
- *Type B uncertainty* is all other uncertainties, e.g. uncertainties specified in data sheets, systematic errors and uncertainties based on personal experiences etc.

In this thesis, both types of uncertainties are present. Generally, uncertainties of the experimental equipment are much smaller compared to other errors.

In order to calculate uncertainties in functions of several variables, e.g. calculation of porosity and permeability, the *error propagation formula* was used [69]. This was utilized for Type B uncertainties. Suppose that the variables $x$, $y$ and $z$ are measured with uncertainties $\Delta x$, $\Delta y$ and $\Delta z$, and the measured values are used to compute a function $q(x,y,z)$. The error propagation formula states that if the uncertainties in $x$, $y$ and $z$ are independent and random, the most likely uncertainty in $q$ is

$$\Delta q = \sqrt{\left(\frac{\partial q}{\partial x}\Delta x\right)^2 + \left(\frac{\partial q}{\partial y}\Delta y\right)^2 + \left(\frac{\partial q}{\partial z}\Delta z\right)^2} \tag{5.5}$$

A factor not included in this formula is human errors and other errors based on experimental procedures. As an example, porosity calculation is considered. Here, only the uncertainties of the slide caliper and the weight, $\Delta r$ and $\Delta m$ respectively, are included in Equation (5.5). Since this equipment provides accurate measurement values, the resulting uncertainty is low. Still, if a failure during the saturation process of the sample core occurs and causes erroneous weight measurements, the resulting porosity estimation is wrong. Hence, experimental errors are superior to the calculated uncertainties and should be included, increasing the total uncertainty.

# 6 Results and discussions

## *6.1 Descriptions of the core samples*

A total of 4 rock core samples were used in this thesis, including one *Berea sandstone* (Berea), *two limestones* (L1 and L2) and one *vuggy carbonate* (VC). The Berea sandstone is considered to be the most homogeneous rock, while the carbonate rocks, especially VC, are more heterogeneous. The petrophysical properties of the core samples are shown in Table 6-1.

**Table 6-1** *Properties of the core samples*

| Sample | Diameter [cm] | Length [cm] | Unsaturated weight [g] | Saturated weight [g] | Pore volume [ml] | Porosity $\varphi$ | Permeability $K$ [mD] |
|---|---|---|---|---|---|---|---|
| | ± 0.01 | ± 0.01 | ± 0.01 | ± 0.01 | ± 0.1 | ± 0.2 | |
| Berea | 3.72 | 5.04 | 114.43 | 125.38 | 10.63 | 19.4 % | 127.5 ± 7 |
| L1 | 3.75 | 5.26 | 128.00 | 136.61 | 8.36 | 14.4 % | 22.0 ± 1 |
| L2 | 3.73 | 5.30 | 129.61 | 137.88 | 8.03 | 13.9 % | 15.0 ± 1 |
| VC | 3.72 | 4.38 | 89.92 | 104.85 | 14.49 | 30.5 % | Not measured |

The permeability of VC is not measured due to experimental difficulties concerning the heterogeneity of the core sample. Figure 6.1 shows the large variations in permeability with increasing core bulk volume for the vuggy material [70]. It is evident that the measured permeability values are a result of the unique properties of each core sample. Based on these observations, the permeability of VC is assumed to be within the range of 30–40 D.

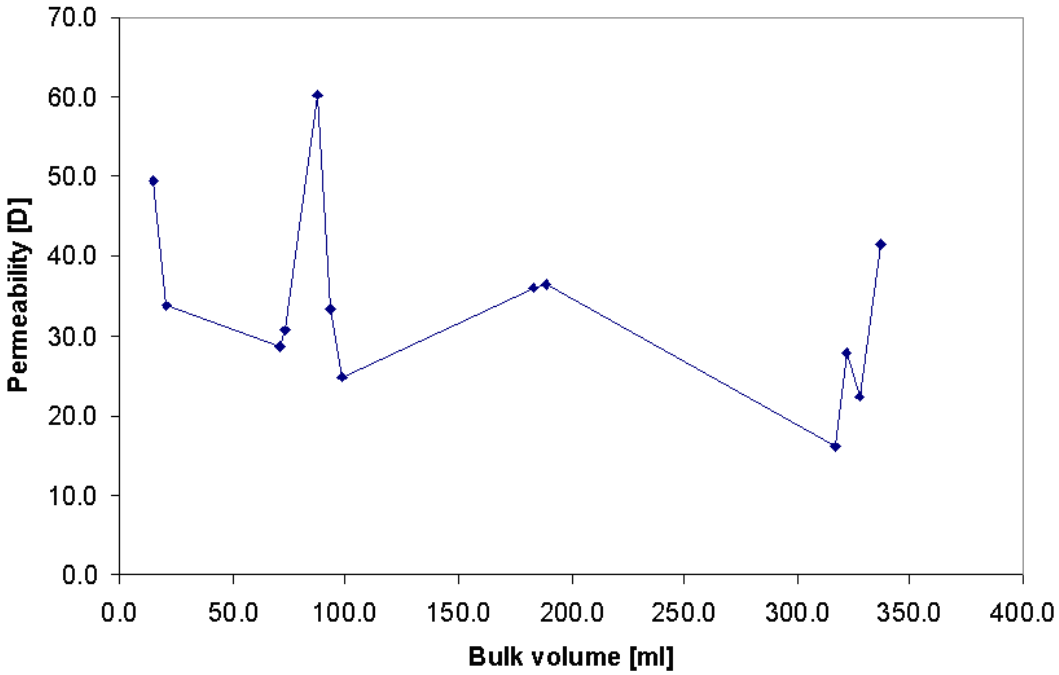


**Figure 6.1** *Measured permeability as a function of Bulk volume for the vuggy carbonate material [70].*

## *6.2 Air-brine drainage*

Primary drainage capillary pressure curves were obtained for all cores in this study by the air-brine procedure I, described in subsection 5.1.1. The relatively homogeneous Berea sandstone was examined first and then used as a reference for the more complex porous materials. Detailed information on time in the centrifuge and transport time, i.e. time to transport the core plug from the ultracentrifuge to the NMR instrument, is shown in Table B-1 in Appendix B. All measurements were performed with the 1D profile sequence described in subsection 4.4.1.

### 6.2.1 Berea Sandstone

Being the most homogeneous rock sample in this thesis, the Berea sandstone was expected to produce a relatively well-shaped capillary pressure curve. Figure 6.2 shows the saturation profiles obtained at 100 % brine saturation and after centrifugation at 1500, 1100 and 750 rpm. Note that a new fully saturated profile was obtained prior to every new rotational speed; the profile in the figure below is given as a reference since all these profiles were considered to be equal.

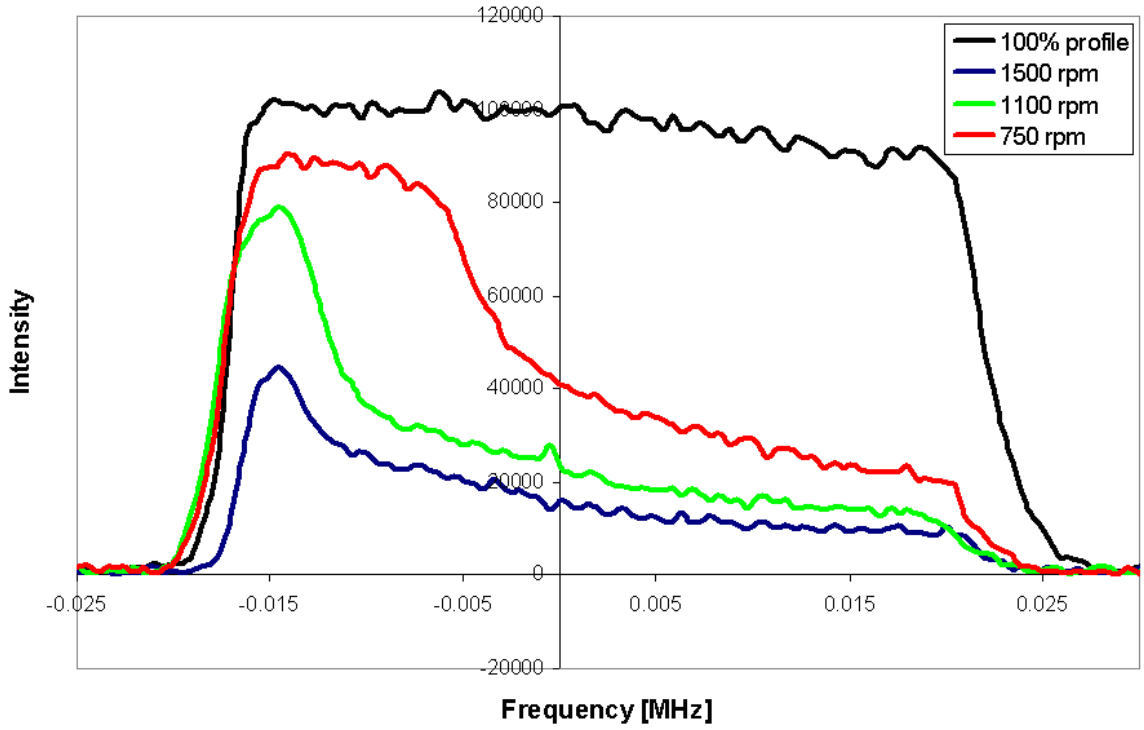


**Figure 6.2** *Measured saturation profiles in the Berea sandstone before (100 % profile) and after centrifugation at three different rotational speeds.*

As shown in Figure 6.3, the individual capillary pressure curves obtained at 1500, 1100 and 750 rpm fit together nicely. High rotational speeds give a higher amount of produced water, pushing the water saturation $S_w$ of the rock sample towards its irreducible water saturation $S_{wi}$. For the Berea sample, $S_{wi}$ = 0.11 is achieved after centrifugation at 1500 rpm. The steep shape of the curve at low water saturations indicate that a higher rotational speed would not result in a lower $S_{wi}$. Lower rotational speeds yield a higher amount of water remaining in the core after centrifugation. Thus, lower capillary pressures and higher $S_w$-values are achieved when $\omega$ = 750 rpm.

The assumption of 100 % water saturation at the outlet end of the core is apparently violated in Figure 6.2, resulting in an initial water saturation of 0.88 in the $P_c$-curve. A threshold pressure of approximately 0.05 bar had to be reached before the air filled the large pores of the sandstone. This relatively low value is due to the high permeability of the Berea sandstone. In general, high permeability yield low threshold pressures and vice versa.

It could be argued that the total capillary pressure curve in Figure 6.3 could be estimated from only two rotational speeds, namely 1500 and 750 rpm. Green et al. [7] also concluded that two

speeds were sufficient for providing good coverage of the primary drainage curve in homogeneous core samples. Nevertheless, the data after centrifugation at 1100 rpm shows a relatively good correlation to the data obtained from the other rotational speeds.

The well-shaped $P_c$-$S_w$ relationship obtained for the Berea sandstone proves the usability of the new method in air-brine systems, and at the same time demonstrating its advantages. The main advantage of the new method is that it allows for many capillary pressure-saturation points to be acquired for each centrifugation speed. The nature of the sandstone material is reflected in the curve, illustrating the advantages of using homogeneous porous material for experimental analysis.

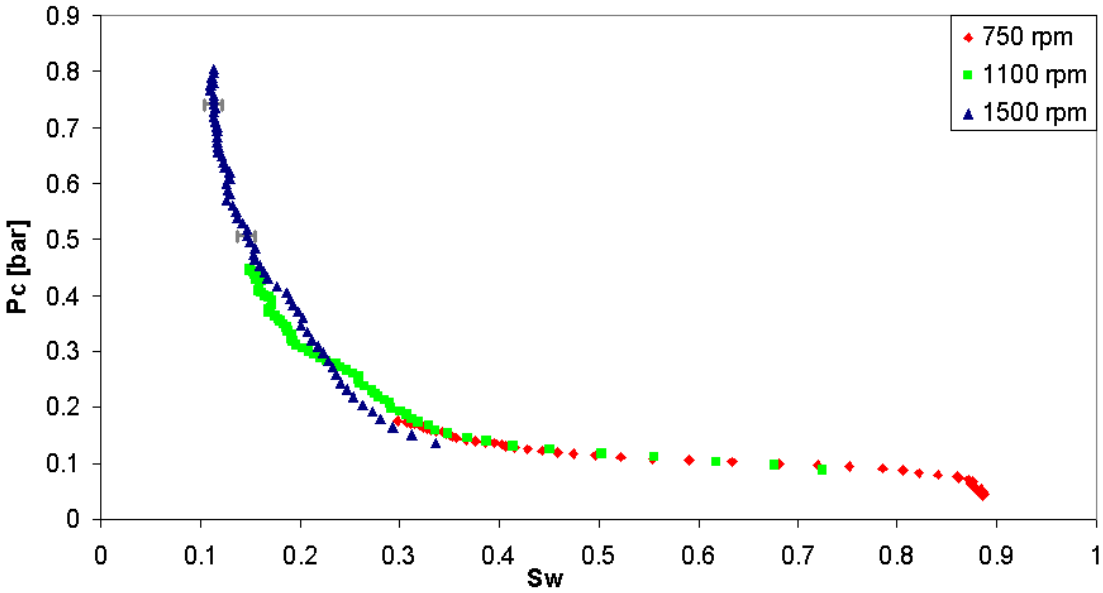


**Figure 6.3** *Air-brine drainage capillary pressure curves for the Berea Sandstone.*

### 6.2.2 Limestones L1 and L2

With the good results obtained for the homogeneous sandstone in mind, the method is tested on the two limestone samples, L1 and L2. Since they possess approximately the same petrophysical properties, it is expected that the capillary pressure distributions of the two core samples are more or less equal.

Due to the heterogeneity of the limestone samples, the saturation profiles are expected to have a higher degree of roughness than in the case of the Berea sandstone. Figure 6.4 and Figure 6.5 shows the measured saturation profiles in the two limestones, L1 and L2 respectively, at

100 % brine saturation and after centrifugation at three different rotational speeds. It is evident that the limestones yield less homogeneous fluid distributions than the Berea sandstone, i.e. the profiles are quite flat even after centrifugation. This will introduce problems when establishing the capillary pressure curve, since less of the saturation range is covered. Note that L2 was centrifuged at 1100 rpm, instead of 1500 rpm, to create a more favourable brine distribution.

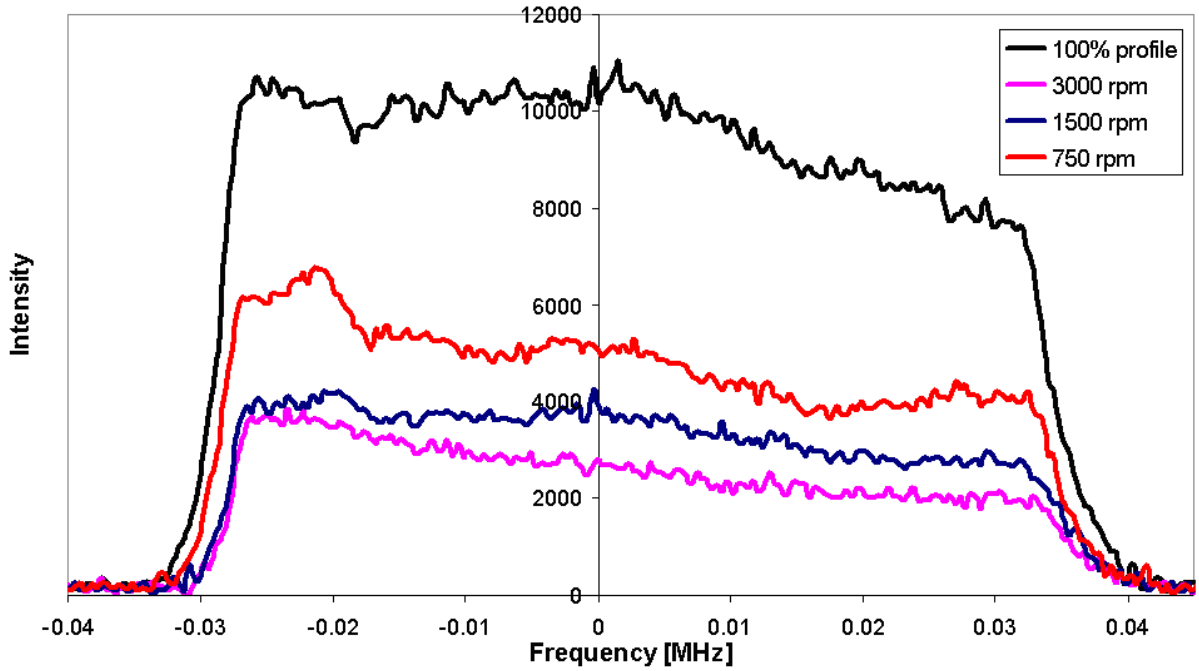


**Figure 6.4** *Measured saturation profiles in the limestone L1 before (100 % profile) and after centrifugation at three different rotational speeds.*

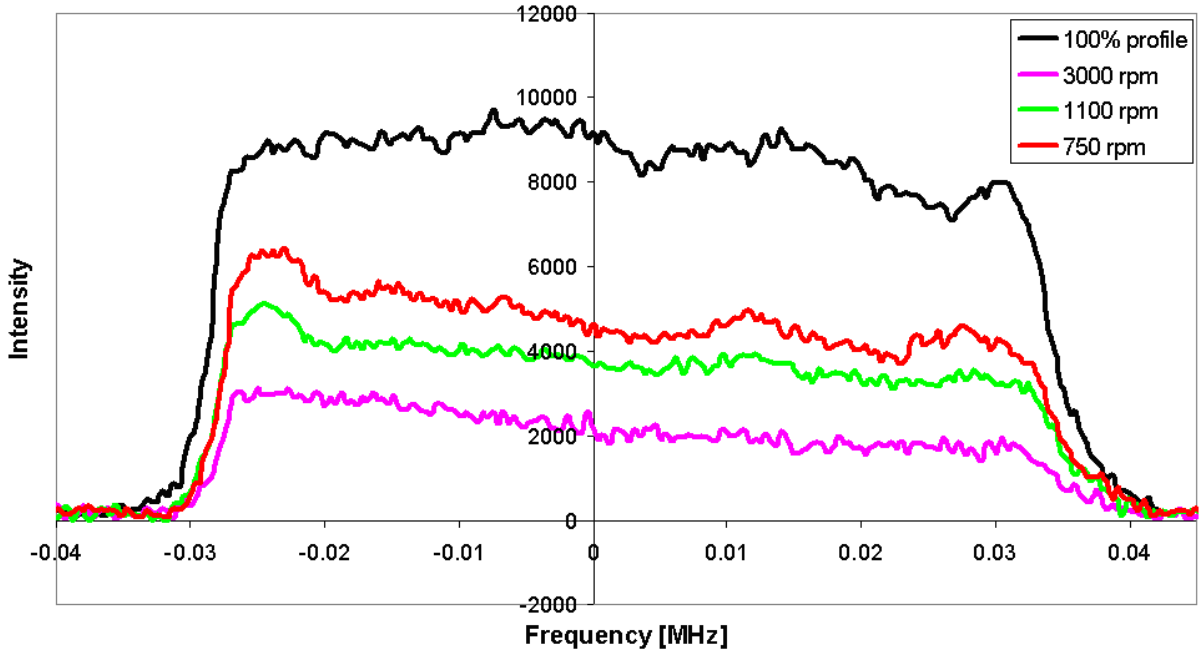


**Figure 6.5** *Measured saturation profiles in the limestone L2 before (100 % profile) and after centrifugation at three different rotational speeds.*

The air-brine primary drainage capillary pressure curve for L1 is shown in Figure 6.6. The curve is obtained by three different rotational speeds; 3000, 1500 and 750 rpm. Due to a relatively long transport time, L1 was centrifuged twice at 1500 rpm (see Table B-1 in Appendix B). A long transport time could have resulted in a change in the fluid distribution within the core plug because wetting fluids tend to redistribute after centrifugation. In spite of this, the second run yielded very similar results as the first one, demonstrating the reproducibility of the current experiment.

Since the capillary pressure curve for L1 obtained after centrifugation at 1500 rpm failed to fill the gap between the two other curves, L2 was centrifuged at 1100 rpm instead. The air-brine primary drainage capillary pressure curve for L2 is given in Figure 6.7. The change in rotational speed provided a better coverage of the saturation range.

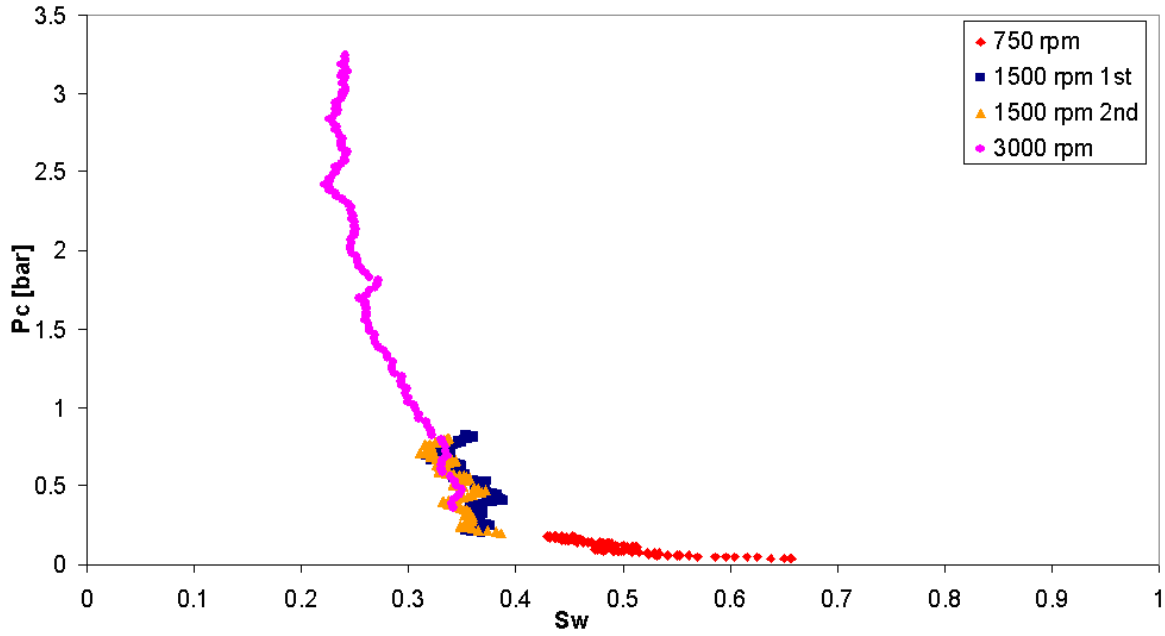


**Figure 6.6** *Air-brine drainage capillary pressure curve for the limestone sample L1.*

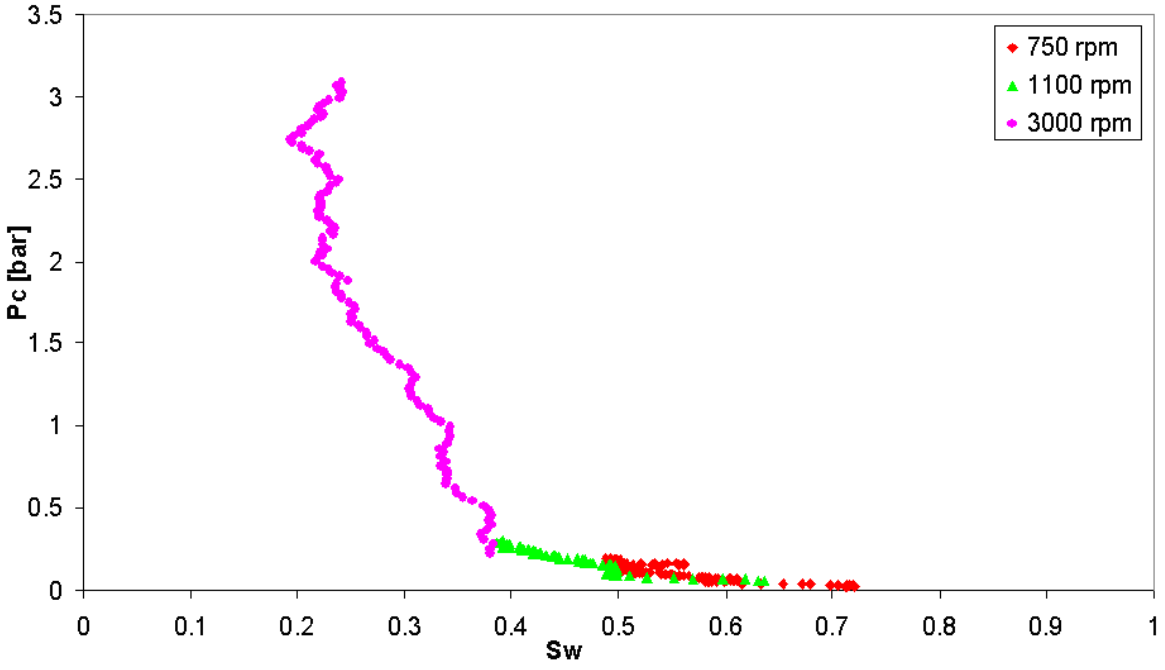


**Figure 6.7** *Air-brine drainage capillary pressure curve for the limestone sample L2.*

Studies have shown that the magnitude of $S_{wi}$ is largely dominated by the heterogeneity of the pore structures [36, 71]. Thus, heterogeneous rock samples yield higher $S_{wi}$-values than more homogeneous rocks. This is the case for the limestone samples used in this thesis, as the measured $S_{wi}$-values for both L1 and L2 are found to be higher than for the Berea sandstone.

Both limestones yield higher capillary pressure values than the Berea sandstone. This is explained from Equation (2.13). Since the interfacial tension $\sigma$ and the wetting angle $\theta$ are assumed to be the same in both rocks, the only factor left in the equation is the pore radius $R$. Limestones possess small pore throats; hence they also possess higher capillary pressures. The small pore throats are also related to the low permeability of the limestone rocks.

Overall, the new method successfully provides capillary pressure curves for the two limestone samples, and at the same time it reflects their complex internal structures. By comparison of the two $P_c$-curves, L2 seems to posses slightly stronger heterogeneous features. The repeatability of the method is considered to be very good since the two samples yield similar curves.

### 6.2.3 Vuggy carbonate VC

The determination of rock properties from laboratory experiments is not trivial for this very heterogeneous type of material. Hence, in many cases unusual results are observed. The VC core used in this thesis originates from the Prebetic subzone of the Betic range (Spain) and its vug sizes are in the range of 0.2-10 mm. The pore space of the material is divided into two main groups, matrix and vuggy. Earlier NMR studies have shown that the total porosity of the vuggy material is typically 29 %, where 65 % is attributed to vugs and 35 % is matrix porosity [25]. The porosity of the VC core plug was measured to be 30.5 %. This high amount of vuggy porosity, and especially touching vugs, indicates that most of the brine will drain from the plug due to gravity as soon as it is exposed to air, if no actions are taken.

In order to obtain the 100 % brine saturated NMR profile, the sides of the plug was fitted with a watertight heat-shrink tube, as recommended by O'Meara et al. [72]. This tube preserves the surface vuggy porosity, preventing fluid loss from the sides of the core plug. To prevent further loss of brine after saturation, one end of the plug was sealed with a plastic plate. These modifications made it possible to measure $M_0$, the 100 % brine saturated profile.

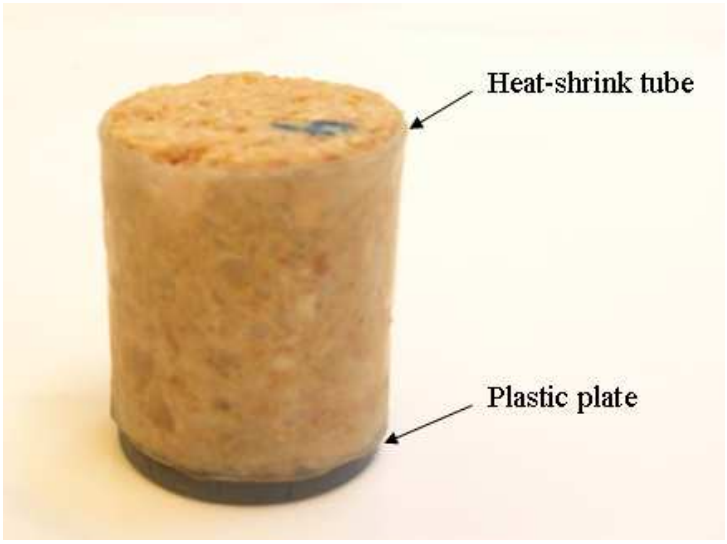


**Figure 6.8** *The vuggy carbonate VC fitted with a heat-shrink tube and a sealing plastic plate.*

When the plastic plate was removed from the bottom end of the core plug, it was assumed that the brine contained in the vugs was instantly removed by gravity drainage. Hence, only the matrix brine should remain in the vuggy carbonate. By centrifuging the core plug in this state, a brine distribution in the matrix porosity was obtainable.

Figure 6.9 shows the measured saturation profiles obtained from VC. Due to the heterogeneity of the core sample, the fully brine saturated profile (100 % profile) shows a strong variation in intensity strength. The peak at the left end of the profile, i.e. the outlet end of the core plug, is considered as a result of accumulation of water at the plastic plate. Hence, these values are excluded from the saturation calculations.

The large loss of intensity after centrifugation supports the theory that the water situated in the vugs is instantly drained from the core and a brine distribution is obtained in the matrix porosity.

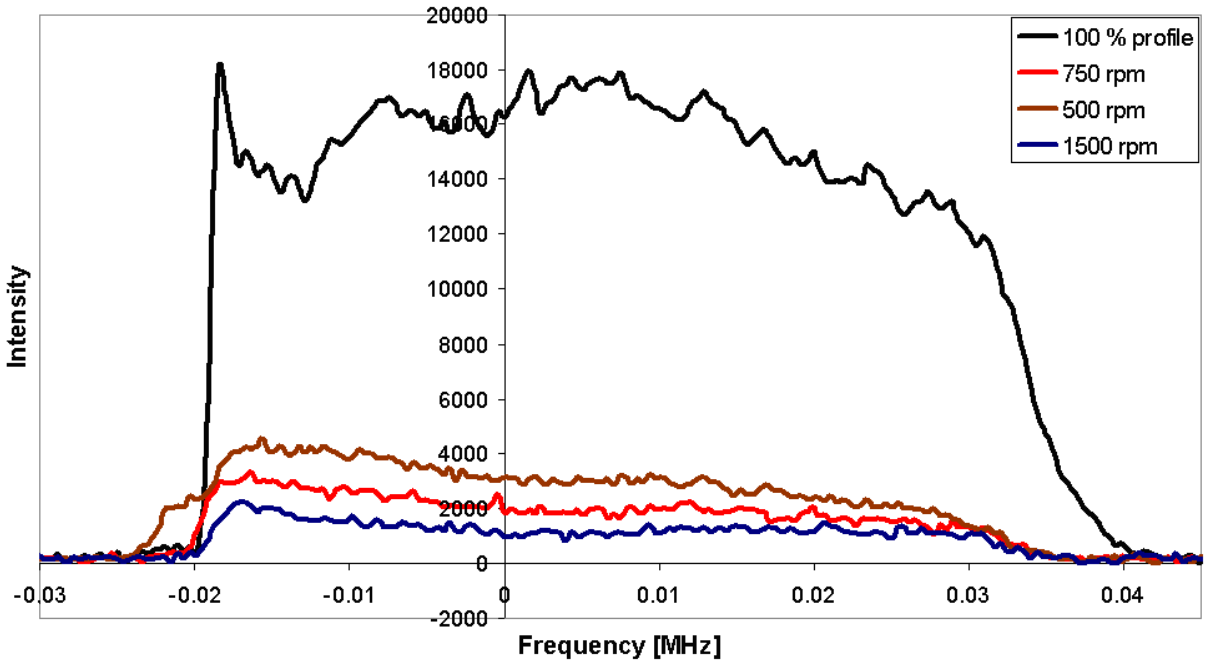


**Figure 6.9** *Measured saturation profiles in the vuggy carbonate VC before (100 % profile) and after centrifugation at three different rotational speeds.*

Since most of the water is drained from the core after centrifugation, it is natural to assume that the primary drainage capillary pressure curve for VC will hold a low initial value of brine saturation. This is confirmed in the capillary pressure curve in Figure 6.10, indicating an initial brine saturation value of approximately 0.3. Although the very heterogeneous nature of the porous material influences the result, a relatively well-defined curve covering a short saturation range is established.

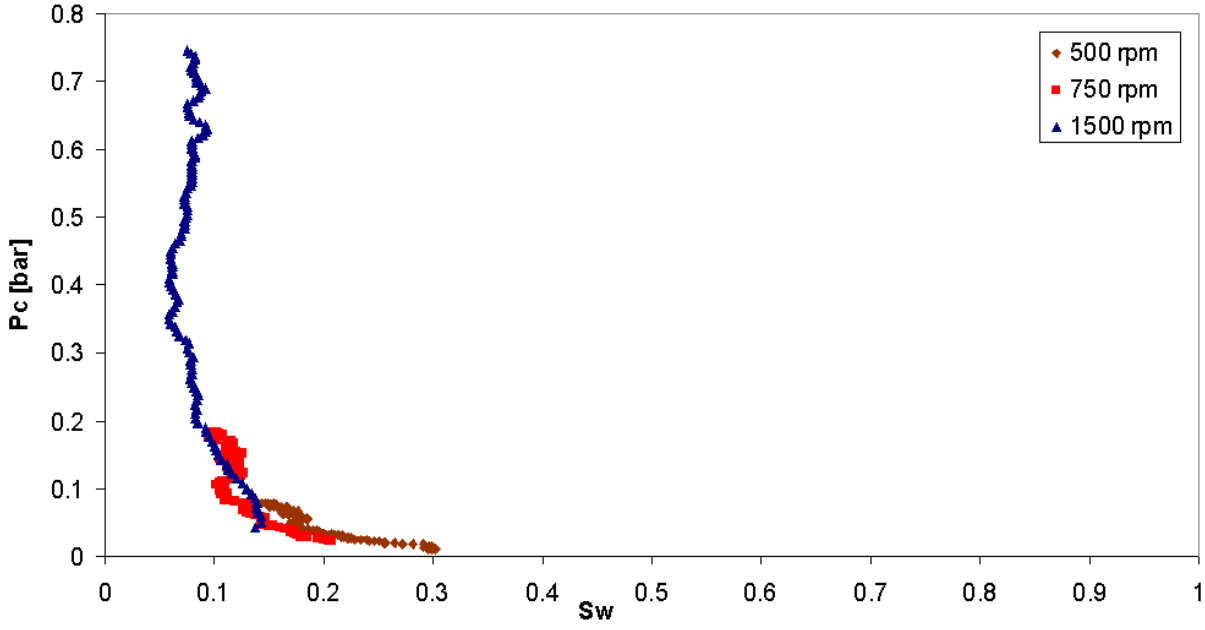


**Figure 6.10** *Air-brine drainage capillary pressure curve for the vuggy carbonate sample VC.*

## *6.3 Alternative air-brine drainage method II*

The *alternative air-brine drainage procedure*, described in subsection 5.1.2, was tested prior to the involvement of oil in an attempt to decrease the total measurement time. The test was performed on the Berea sandstone. In this alternative method, it is important to emphasize the stoppage time between the two centrifuge speeds, i.e. the time it takes to transport the plug to the NMR instrument, perform measurements and transport it back to the centrifuge. It is vital that this period is as short as possible to prevent redistribution of fluids within the rock core. In the current test measurement, the stoppage time was 12 minutes and 49 seconds.

Figure 6.11 shows the saturation profiles obtained before and after centrifugation at 750 and 1500 rpm. It is important to emphasize that the core had to be centrifuged at the lowest rotational speed first, before progressing to higher speeds. This is important because the plug is not re-saturated with brine between each centrifugation. The level of brine saturation is at its lowest after 1500 rpm; hence this speed is the last to be run.

Since the core was fully brine saturated prior to the centrifugation at 750 rpm, the resulting capillary pressure curve should be equal to the one obtained earlier (see Figure 6.3). Thus, the results from the centrifugation at 1500 rpm are the data of main interest.

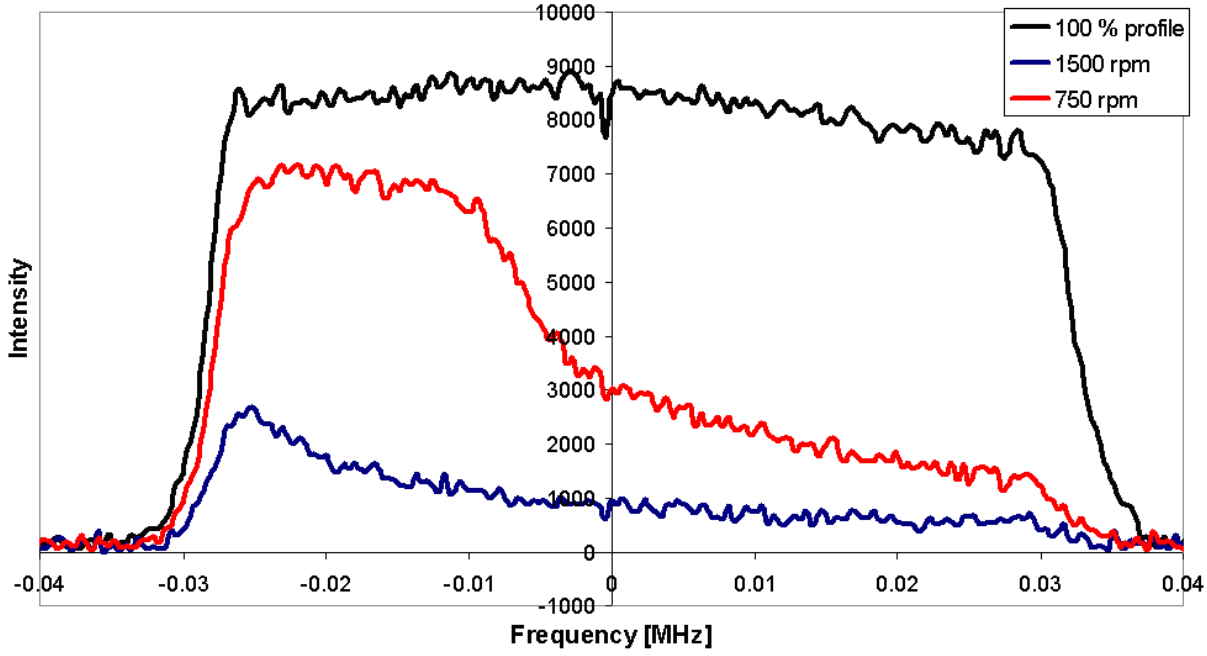


**Figure 6.11** *Measured saturation profiles in the Berea sandstone before (100 % profile) and after centrifugation at two rotational speeds.*

Figure 6.12 shows a comparison of the primary drainage capillary pressure curves obtained with the original and the alternative method. The curves from the 750 rpm centrifugations overlap fairly well, but there is a trend towards lower brine saturations. This trend proceeds into the new curve from the centrifugation at 1500 rpm. Overall, the total curve obtained with the alternative method yield lower brine saturation values than the original curve.

The alternative curves show a more varying nature due to a change in the NMR parameter settings. The alternative method was carried out with the same parameters as the carbonate rocks, i.e. not the same as the original Berea measurements. All parameters are shown in Table C-1 in Appendix C. Still, this change should not influence the capillary pressure curves.

The lower $S_{wi}$-value observed in the alternative method is in accordance with the results of Hassler and Brunner [3]. They stated that if the centrifuge is stopped and then brought back to its previous speed, more fluid is expelled from the core than before the interruption due to fluid redistribution. The subject of fluid redistribution is further investigated in subsection 6.7.6. It is found that the rate of redistribution is lower in oil-brine processes than in processes concerning air and brine. Based on this conclusion, it is suggested that stopping the centrifuge has a smaller effect on the $S_{wi}$-values in an oil-brine drainage process.

The fact that the new data generate a well-shaped capillary pressure curve with the same shape as the old data indicates that the measurements and calculations are correct. As mentioned above, the results from the centrifugations at 750 rpm should be equal. If so, the similarity of the $S_{wi}$-values obtained from the two methods would increase. It is feasible to assume that the change in brine saturation is a result of changes in the properties of the core rather than errors concerning the alternative method. By excluding the re-saturation process from the oil-brine experimental procedure, the total measurement time is dramatically decreased.

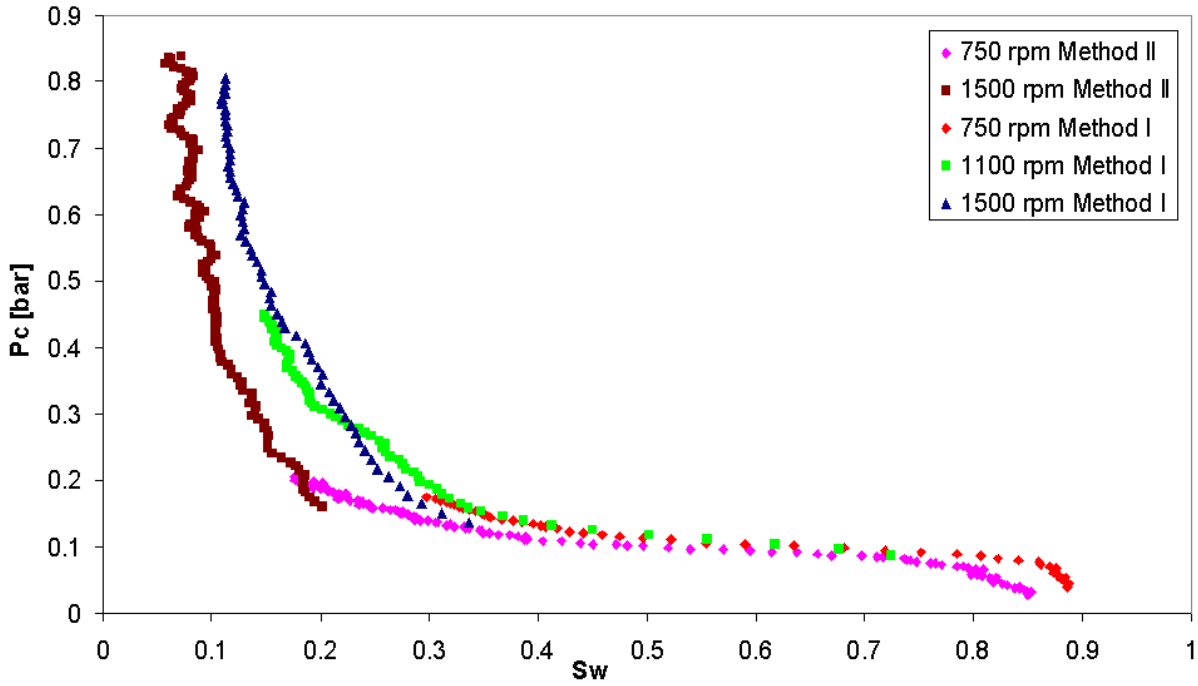


**Figure 6.12** *A comparison of the air-brine drainage capillary pressure curves for the Berea sandstone obtained with the original and the alternative method (I and II).*

## *6.4 Oil-brine drainage*

Studies have shown that capillary pressures for a gas-liquid system are not transposable to a liquid-liquid system [26]. Due to the differences in density, oil-brine measurements yield lower capillary pressure values than air-brine measurements. Hence, oil-brine capillary measurements are needed to study the interactions between oil and brine. By performing the procedure in subsection 5.1.3, a primary drainage capillary pressure curve was measured for the Berea sandstone and the two limestones L1 and L2. Note that the re-saturation process between each centrifuge speed was removed in the oil-brine procedures. In accordance with the measurements performed on the air-brine system, the Berea sandstone was studied first and then used as a reference for the limestone samples.

Subsection 5.2.1 explains how the brine intensity values presented in this section are calculated, as opposed to the air-brine process where the brine intensity was directly measured. Detailed information on centrifugation, transport and stoppage time is provided is Table B-2 in Appendix B.

### 6.4.1 Berea sandstone

As shown in Figure 6.3, the Berea sandstone yielded relatively smooth capillary pressure curves for an air-brine drainage process. It is expected that more fluctuating results are obtained when oil is introduced to the system and the diffusion-weighted spin echo sequence is used to differentiate the water signals from the oil signals in the NMR measurements.

Figure 6.13 shows the calculated brine saturation profiles in the Berea sandstone. The lack of a distinctive brine distribution after centrifugation at 750 rpm, i.e. only small amounts of oil entered the rock core, led to the conclusion that a higher rotational speed was necessary to create a fluid distribution in an oil-brine system. This conclusion is supported by theory, since the high viscosity of Marcol 82 leads to a high mobility ratio between the oil and brine [13]. Hence, a final centrifugation at 1800 rpm was added.

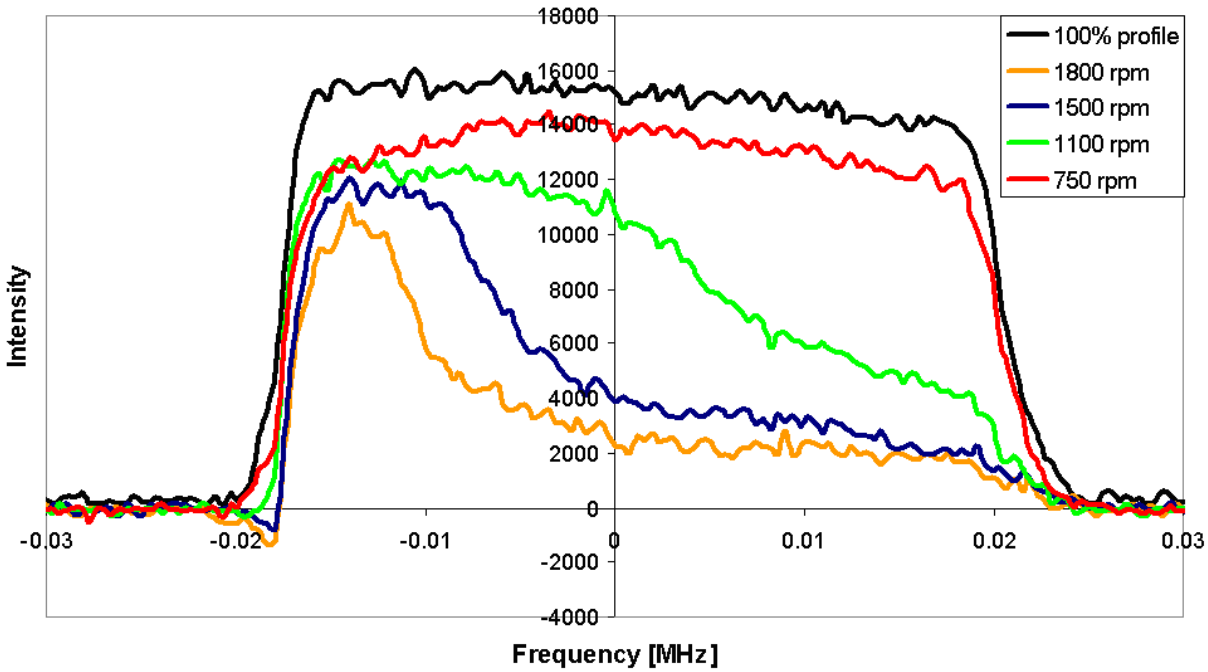


**Figure 6.13** *Calculated brine saturation profiles in the Berea sandstone before (100 % profile) and after centrifugation at four different rotational speeds.*

As already mentioned, it was expected that the oil-brine capillary pressure values was lower than the air-brine values due to differences in density and interfacial tensions. In the air-brine calculations, the density of air was neglected from Equation (3.7), i.e. only the density of water was used in capillary pressure calculations. The density of oil, on the other hand, cannot be neglected and must be included in the term $\Delta\rho$, causing a lower calculated capillary

pressure value. In addition, the interfacial tension $\sigma$ in Equation (2.13) is lower in an oil-brine process.

The oil-brine drainage capillary pressure curve for the Berea sandstone is shown in Figure 6.14. The expected irregularities and lower capillary pressures due to oil implementation are present, but an overall $P_c$-$S_w$ relationship is clear. Based on the shape of the curve, a higher centrifugation speed should be added in order to produce an accurate $S_{wi}$-value. Still, the method is proved to be applicable in oil-brine systems.

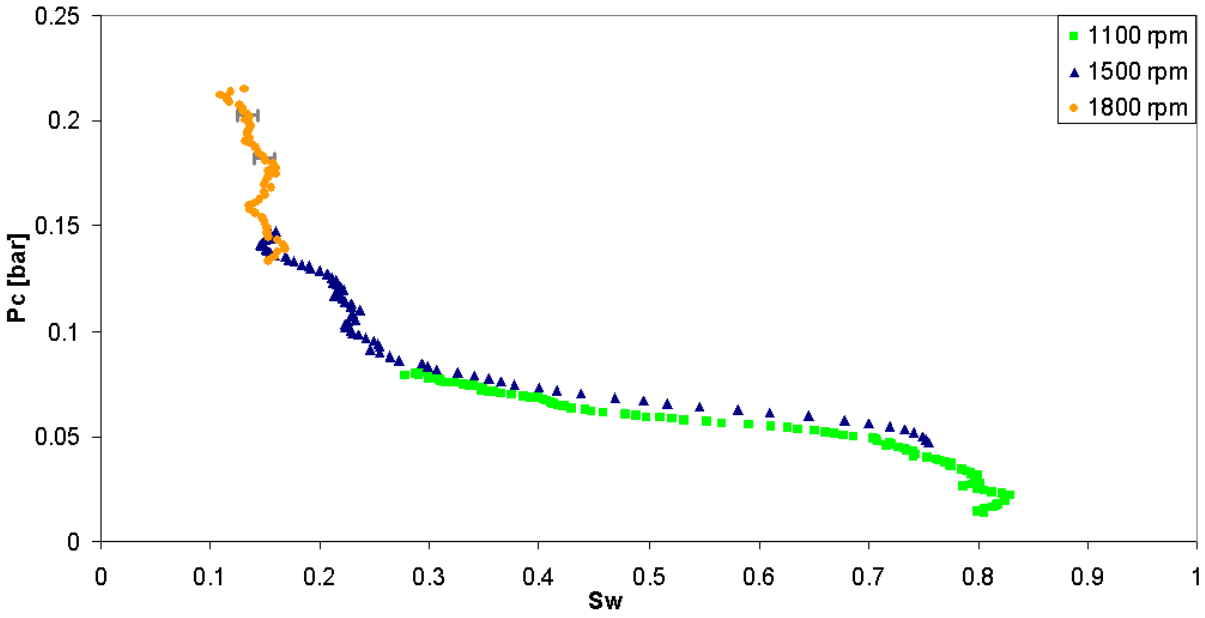


**Figure 6.14** *Oil-brine drainage capillary pressure curve for the Berea sandstone.*

### 6.4.2 Limestones L1 and L2

The heterogeneous specificity of L1 and L2 are evident in the brine saturation profiles in Figure 6.15 and 6.16. Both samples, especially L2, yield irregular oil flow patterns. This is considered to be a result of the inhomogeneous nature of the porous material, a subject to be further discussed in section 6.6.

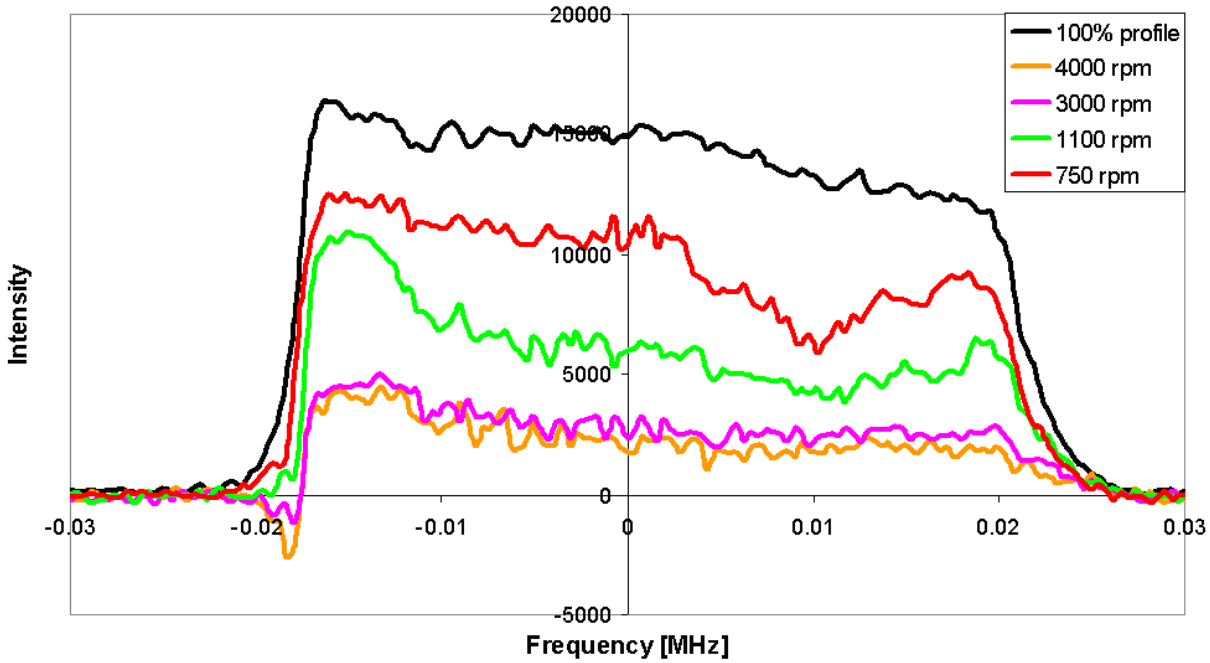


**Figure 6.15** *Calculated brine saturation profiles in L1 before (100 % profile) and after centrifugation at four different rotational speeds.*

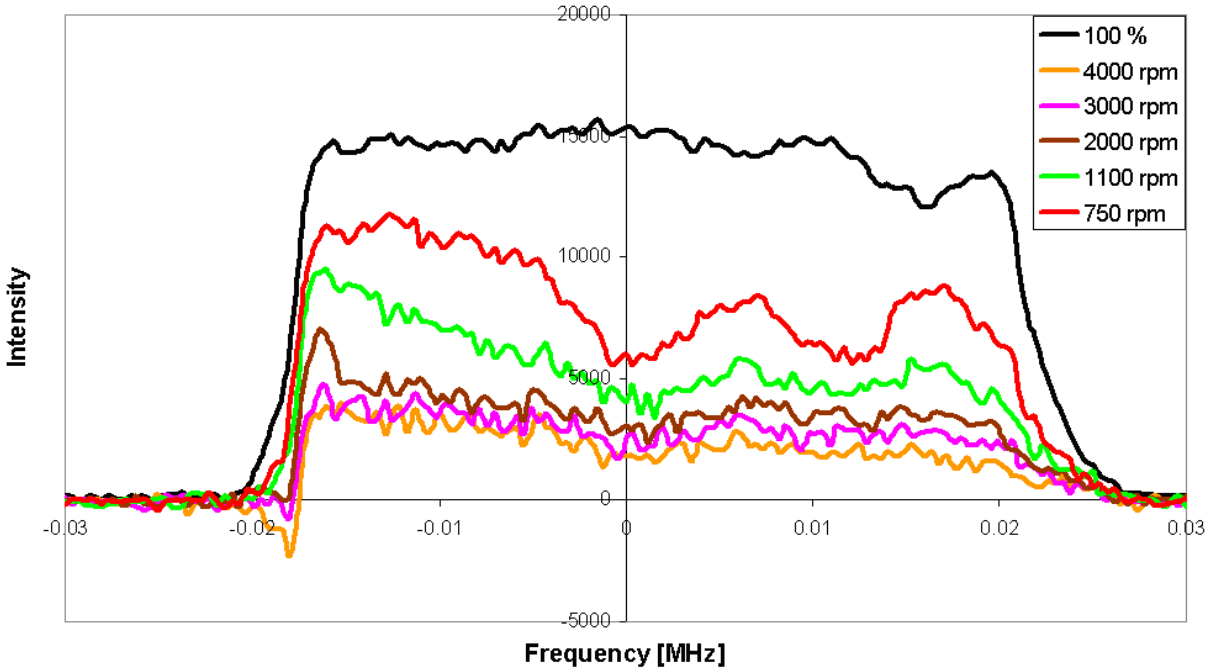


**Figure 6.16** *Calculated brine saturation profiles in L2 before (100 % profile) and after centrifugation at five different rotational speeds.*

The oil-brine primary drainage capillary pressure curves for L1 and L2 are shown in Figure 6.17 and Figure 6.18, respectively. As expected, the limestone cores yield higher $P_c$-values than the Berea core. The irregular oil flow patterns are reflected in the curves, indicating that there are heterogeneous differences between the two core samples. In particular, the highly

fluctuating saturation values obtained for L2 causes large uncertainties concerning the result, making it difficult to establish a $S_{wi}$-value for the core plug. However, the result obtained for L1 is considered to be a representative capillary pressure-saturation relationship for the limestone material.

These results demonstrate another advantage of the new method; the accuracy of its measurements. The heterogeneous features of L2 would not be accounted for if the water saturation of the core was represented by a mean value, as is the case for the original centrifuge method proposed by Hassler and Brunner [3].

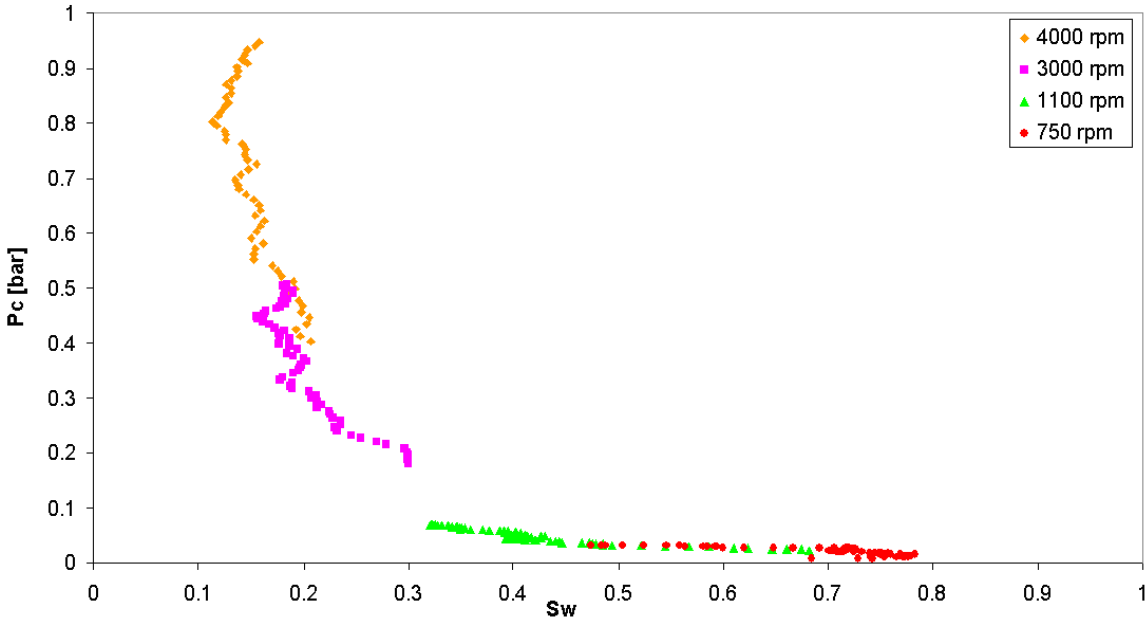


**Figure 6.17** *Oil-brine drainage capillary pressure curve for L1.*

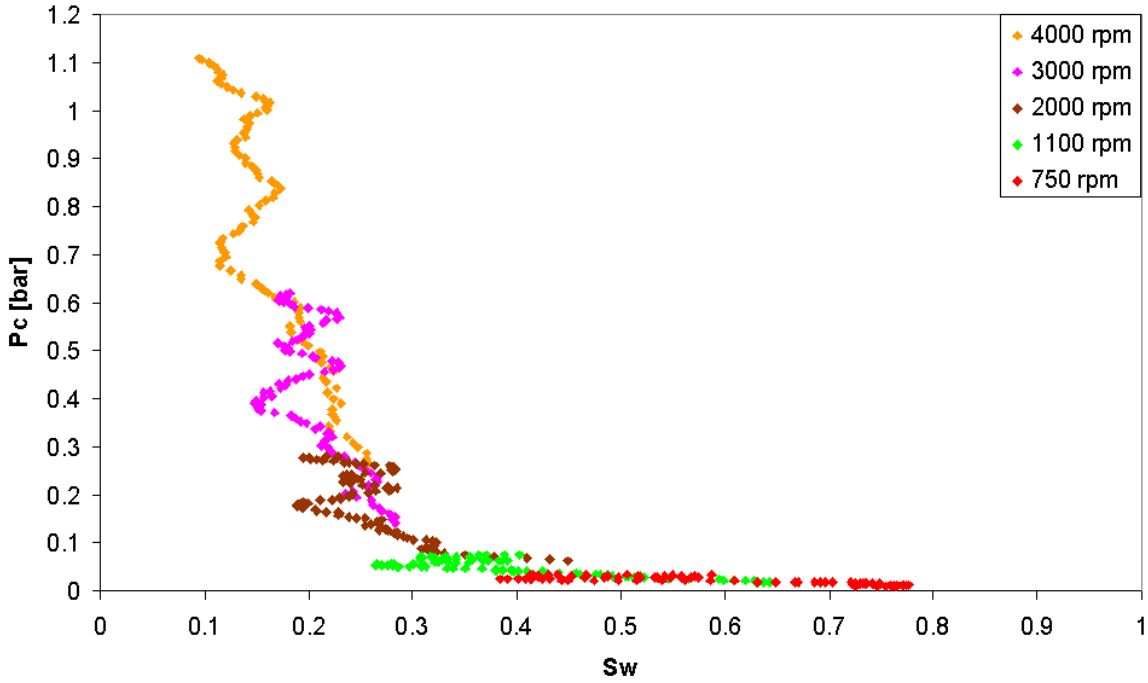


**Figure 6.18** *Oil-brine drainage capillary pressure curve for L2.*

## *6.5 CPMG experiments*

$T_2$ distributions were measured with the CPMG sequence, explained in subsection 4.3.2. The system parameters used are listed in Table C-1 in Appendix C. The measured data was inverted by the software WinDXP from Resonance Instruments. Note that the distributions themselves are approximations, as a result of the ill-fitted inversion problem.

The pore size distributions of all four core samples are presented in Figure 6.19. The Berea sandstone has a typical high amount of intergranular pores and a small contribution from the smaller pores. The limestones L1 and L2 yield similar distributions, with a relatively wide range of pore sizes, demonstrating the diversity of the material. The vuggy carbonate VC results are discussed in detail in section 6.6.

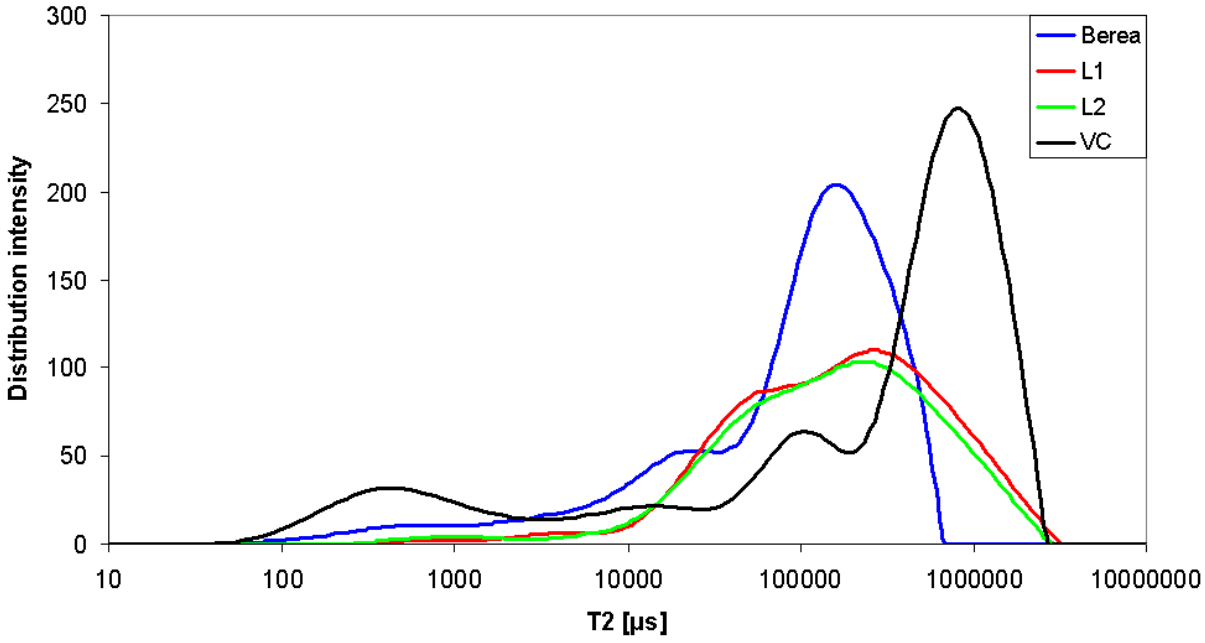


**Figure 6.19** *Pore size distributions for all 4 samples at $\tau$ = 100 $\mu$s.*

## *6.6 Effects of heterogeneities*

In reservoir characterization, heterogeneity specifically applies to the variability that affects fluid flow [73]. The permeability of a rock varies more than other properties that affect flow and displacement processes in a porous rock. Thus, it is essential to describe the variation of permeability for a heterogeneous material. Studies have shown that several difficulties arise when measuring permeability in very heterogeneous material [74].

However, a measure of variability can be applied for any petrophysical property. The heterogeneity of a rock influences other petrophysical properties, like porosity, capillary pressure and saturations. For instance, during a forced immiscible displacement heterogeneities may cause preferential pathways for the displacing fluid, influencing the residual saturations of the rock. Consequently, the total oil recovery is affected by the heterogeneity of the rock, demonstrating the importance of the subject.

Several studies investigate the effect of heterogeneities with mathematical descriptions and simulations [75-79]. In this thesis, the heterogeneity effects are examined using data obtained from laboratory core measurements on small plugs. Such measurements are considered as questionable and inaccurate, because small plugs are not representative and can not reveal the heterogeneous features within a large-scale reservoir rock. However, the results can provide

basis for further simulation work and give an indication on the reservoir properties through a process known as scaling, preferably performed with the dimensionless capillary J-function introduced by Leverett in 1941 [32]. The experiments show the variability of capillary pressure along a sample.

The studied core materials represent different degrees of heterogeneity, ranging from the relatively homogeneous Berea sandstone to the more heterogeneous vuggy carbonate VC. By comparing the fully brine saturated profiles of all four core plugs, i.e. the 100%-profiles in Figure 6.2, 6.4, 6.5 and 6.9, the differences caused by heterogeneity are evident. The profiles after centrifugation also yield the same trends, with smoother curves in the more homogeneous Berea rock. The measured proton intensity values reflect the differences in porosity, and hence water saturations, within the rock.

The effects of inhomogeneities are clear in the results. The resulting capillary pressure-saturation relationship for L2, depicted in Figure 6.18, yields large saturation variations due to the irregular flow pattern of the oil during centrifugation. Figure 6.20 shows the behaviour of the oil during the drainage process. The measured oil intensity shows large variations at the inlet end of the core. By comparing Figure 6.5 and Figure 6.16 it is feasible to conclude that this behaviour is also present in the air-brine measurements, although to a lesser degree. During their studies on chalk samples, Olsen et al. [80] used a 1D CSI spectroscopy pulse sequence to create saturation profiles on an inhomogeneous sample. They obtained similar irregularities and concluded that it was caused by stylolites, i.e. surfaces within the rock which are seen as complex, highly irregular fine lines in vertical sections [19]. Hence, it could be argued that the irregularities in oil saturation are due to internal structures, e.g. stylolites. The high mobility ratio in the oil-brine drainage process could cause these structures to become more visible than in the air-brine drainage.

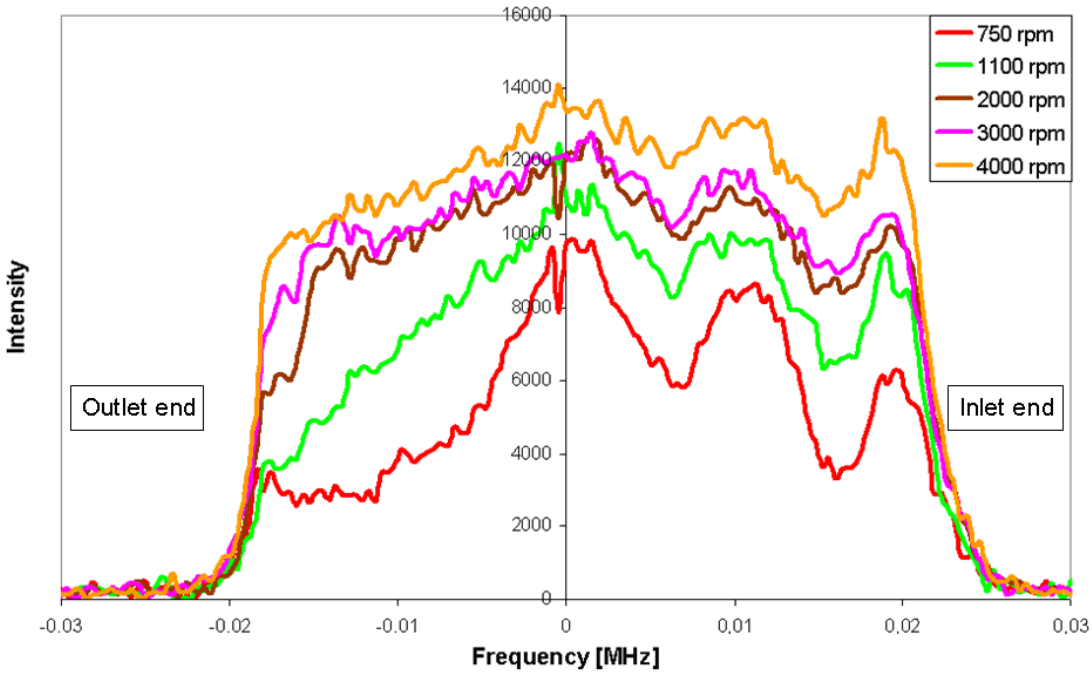


**Figure 6.20** *Measured oil saturation values for L2 at increasing centrifugation speeds.*

The measured permeability of L2 is lower than L1 (see Table 6-1), even though they originate from the same outcrop rock. This could be another indication of internal structures hindering fluid flow. By visual examination, some clear heterogeneous features are found at the inlet end of L2. These are shown in Figure 6.21.

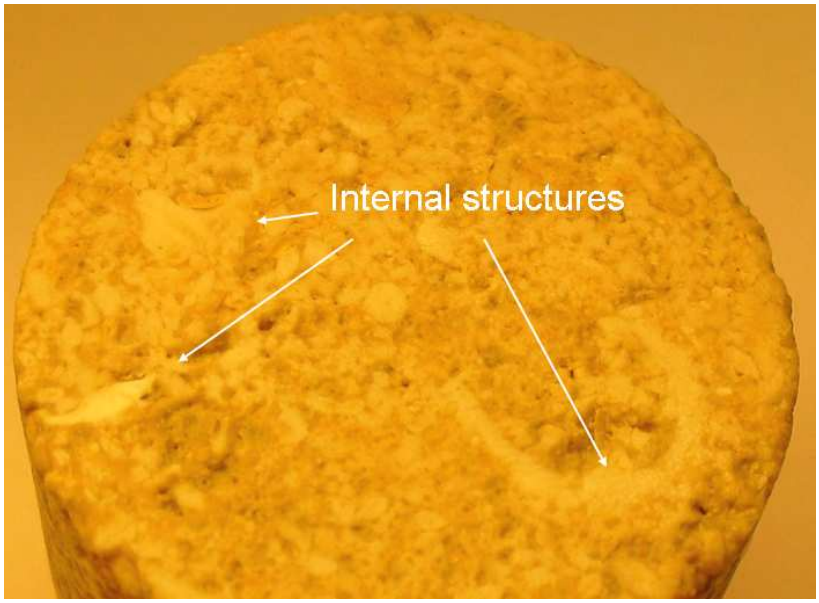


**Figure 6.21** *Structures observed at the inlet end of L2.*

Based on the observations discussed above, it is concluded that the variations found in the oil-brine $P_c$-curve for L2 are a result of internal heterogeneities. This demonstrates some of the difficulties that arise when heterogeneous porous materials are examined. It also shows how the new method is able to detect these irregularities.

Being the most heterogeneous rock in this thesis, the results from VC are also examined in closer detail. The primary drainage capillary pressure curve obtained with the current method in this thesis is based on saturation measurement throughout the full length of the core sample, i.e. the actual brine saturation in the rock is measured. This curve is compared to a capillary pressure curve obtained with the centrifuge method for a sample of the same type of material, hereby referred to as VC2, in Figure 6.22 [70]. The properties of VC and VC2 are compared in Table 6-2. The centrifuge method introduced by Hassler and Brunner, as described in detail in section 3.3, measures average values for both water saturation and the capillary pressure of the rock core. Thus, as opposed to the NMR method, it fails to produce the actual fluid distribution within the rock. The NMR method reveals fluctuations for the saturation profile caused by the heterogeneity along the sample. This is evident by comparing the saturation profiles obtained for the Berea core and VC in Figure 6.2 and Figure 6.9, respectively. It should be noted that a different centrifuge with a larger rotational axis was used in the VC2 measurements. The final result is that the heterogeneities of the core are not accounted for in the centrifuge method and higher $P_c$-values are obtained. Thus, the Hassler Brunner approach may provide wrong capillary pressure-saturation functions for heterogeneous samples. This is in accordance with the results found by other studies [27].

Wathab [36] found that the irreducible water saturation $S_{wi}$ is higher in large core samples than in smaller samples. Thus, it could be argued that VC yields a slightly lower $S_{wi}$-value due to the difference in the sample length between VC and VC2.

**Table 6-2** *Comparison of petrophysical properties*

| Core | VC | VC2 |
|---|---|---|
| Length [cm] | 4.38 | 6.45 |
| Pore volume [ml] | 14.49 | 20.10 |

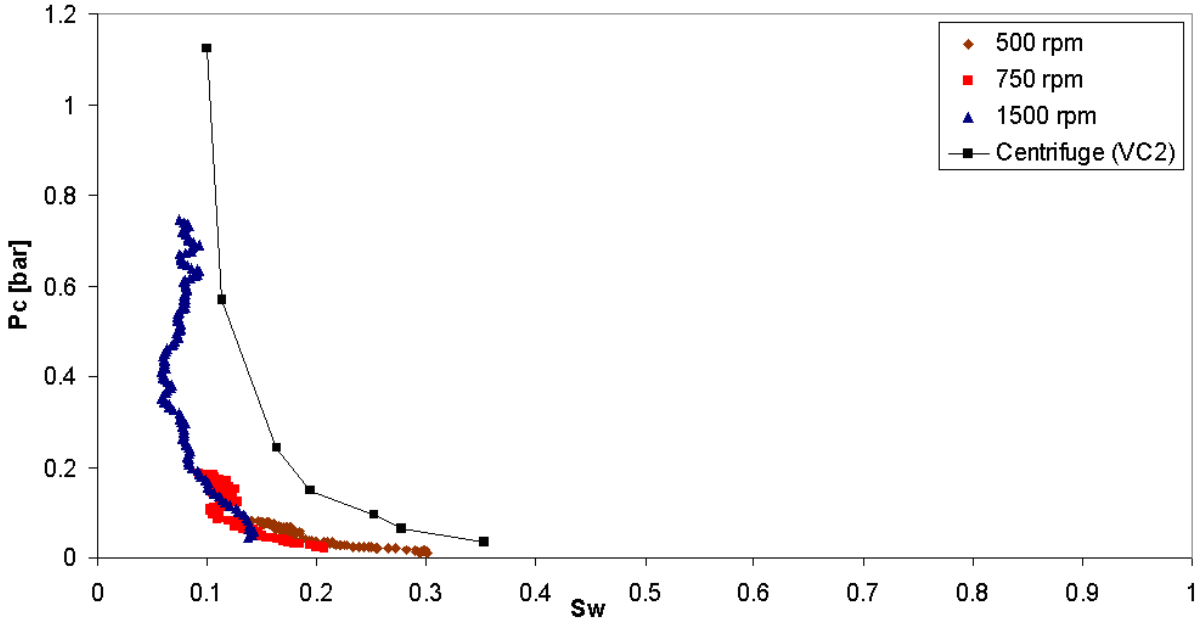


**Figure 6.22** *Comparison of the capillary pressure curves from VC and VC2 obtained with the current method (VC) and with the Hassler Brunner centrifuge method (VC2).*

As stated in subsection 4.3.6, the $T_2$ distribution in a porous media is a function of pore size, and a $T_2$ distribution plot can be divided into Bound Volume Irreducible (BVI) and Bulk Volume Movable (BVM). In a vuggy carbonate, the pore size distribution can be divided into matrix and vuggy porosity. In accordance with earlier studies [25, 39, 81-82], a threshold value, known as the cut-off value $T_{2co}$, dividing matrix and vuggy porosity is set between the two main pore size populations. The cut-off value $T_{2co}$ was chosen at 0.2 sec. By calculating the area under the main peak, the vuggy porosity is seen to contribute to 65.3 % of the total porosity of VC. This value is corresponding well with the results found by the studies referred to above.

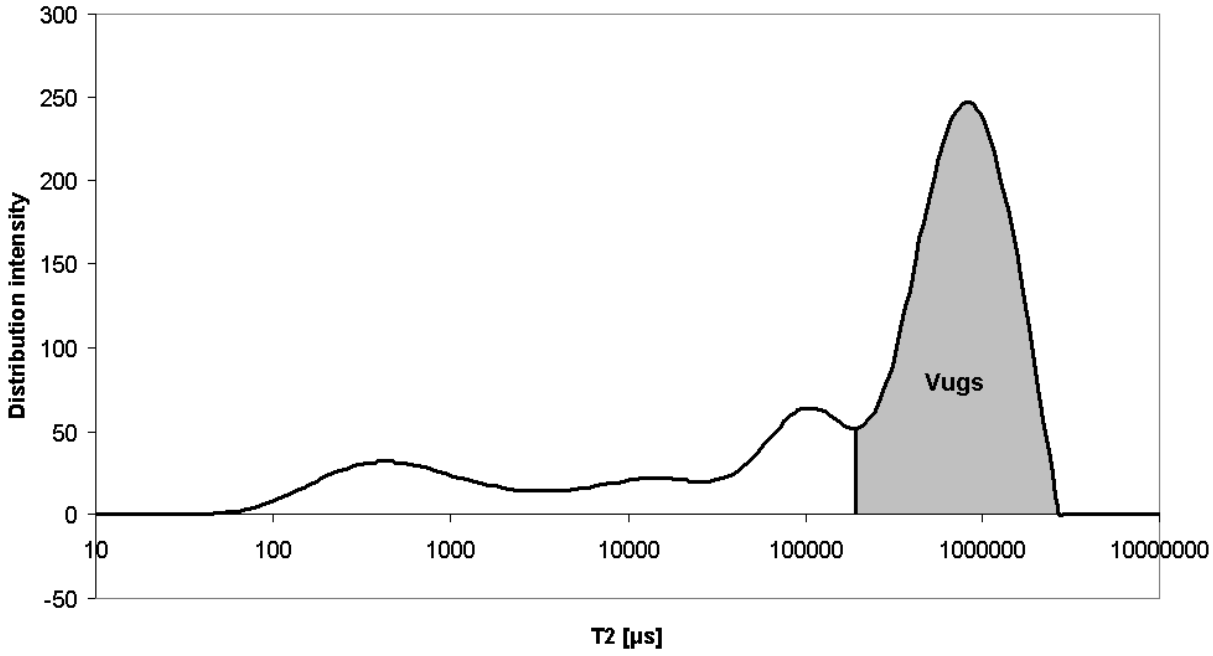


**Figure 6.23** *$T_2$ distribution for the vuggy carbonate VC. The grey area belongs to vuggy pore space, calculated to be* 65.3 *% of the total porosity.*

After the 100% brine saturated profile was obtained for VC, the sealing plastic plate was removed, causing brine to drain from the core due to gravity. The core was then measured again with the CPMG sequence, yielding a new $T_2$ distribution shown in Figure 6.24. $T_2$ distributions obtained after centrifugation at 500, 750 and 1500 rpm are also shown in the same figure. It is evident that with increasing centrifuge speeds the water in the vuggy pore space is progressively displaced by air. Two hypothesises can be suggested from the distribution results.

The first hypothesis is that water in the connected vugs is drained from the rock by gravity and the remaining water is contained in isolated vugs. In this case the vugs are disconnected between the in- and outlet of the core, i.e. there is no vuggy connectivity throughout the core. Hence, a total of 90.4 % of the vuggy porosity is present as isolated vugs. It should be mentioned that the shrink tube surrounding the core could have caused some connected vugs to become isolated. Such a high amount of isolated pores would result in a very low permeability, in contrast to the apparent high permeability of the VC plug. In addition, earlier studies have proved the high connectivity of the vuggy material [83]. Hence, this first hypothesis is considered as invalid.

The second hypothesis suggests that a certain force is needed in order to drain the water in the connected vugs. It is suggested that this force lies somewhere between the strength of the gravity force and the applied force during centrifugation at 500 rpm. Hence, the water in connected vugs is trapped by capillary forces during the gravity drainage process. This presence of capillary pressure in connected vugs violates assumptions made in some simulation studies, where $P_c = 0$ in vugs often is assumed [78, 84-85].

Earlier in this thesis, it was assumed that the brine distribution measured in VC after centrifugation represented the matrix porosity and a small amount of isolated vugs. The $T_2$ distributions confirm this hypothesis, since the water in the vuggy pore space is progressively drained after centrifugation. The small peak remaining in the right hand side after $\omega$ = 1500 rpm corresponds evidently to a small amount of isolated vugs [86]. Thus, the capillary pressure curve obtained for VC represents the capillary pressure – saturation relation in the matrix porosity. This is highly applicable in simulations with dual porosity models, where the capillary pressure curve can be assigned to the matrix portion of the model. Studies by Moctezuma et al. [86-87] propose the application of mercury injection capillary pressure curves for this purpose. The new method presented in this thesis is preferable in this case due to its rapid and non-destructive nature.

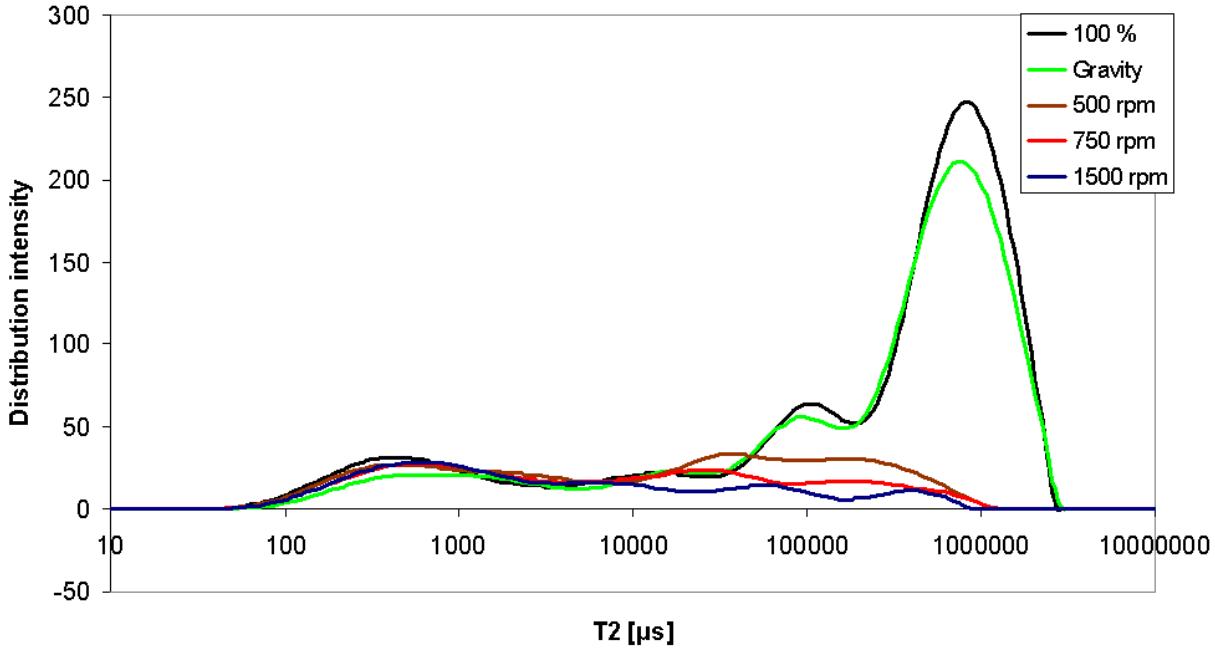


**Figure 6.24** *$T_2$ distribution for the vuggy carbonate VC at* 100% *brine saturation, after gravity drainage and after centrifugation at* 500, 750 *and* 1500 *rpm.*

Despite the high connectivity of the vugs in the studied material, the $T_2$ distribution in Figure 6.24 verifies that a certain force is needed in order to drain water in connected vugs with air. Thus, capillary pressure is also present in connected vugs. Since vugular carbonates and naturally fractured reservoirs are classified as dual-porosity reservoirs, dual-porosity models are used for simulation studies. In some of these models, vugular capillary pressure is assumed to be zero. The studies performed on a vuggy carbonate in this thesis questions the validity of this assumption. In addition, it is suggested that the matrix capillary pressure is measurable with the current NMR method.

## *6.7 Experimental errors*

### 6.7.1 Uncertainties concerning saturation profiles

For results to be widely accepted, the uncertainties of the measurements must be addressed. The signal to noise ratio (SNR) is used to quantify how much a signal has been corrupted by noise. It is favourable to have a high SNR value. All NMR measurements in this thesis contain some amount of noise. The part of the signal owing to noise is considered to be constant. Hence, a weaker signal yields a lower SNR and vice versa. This means that the measured proton intensities after centrifugation are more influenced by noise than intensities measured at high water saturations.

Errors in the measured NMR intensity values, referred to as a Type A uncertainty in subsection 5.2.5, were investigated by performing continuous measurements, 21 in total, with all pulse sequences. The 1D profile sequence measured a water saturated sand sample, while the diffusion-weighted pulse sequence measured a sand sample containing equal amounts of oil and water. A standard deviation *SD* was found for each intensity value from the equation

$$SD = \sqrt{\frac{1}{N-1}\sum_{i=1}^{N}(x_i - \bar{x})^2} \tag{6.1}$$

where $N$ is the number of measurements performed, i.e. 21, $x_i$ is the measured intensity value and $\bar{x}$ is the mean intensity.

In air-brine systems, one pulse sequence was used and hence one *SD*-value can pass for all measurements. However, for all oil-brine systems, both the total intensity $M_{tot}$ and the oil signal $M_{oil}$ were measured (see subsection 5.2.1). It was found that $M_{oil}$ had to be multiplied by a factor of 1.78 due to suppression of the oil signal. Hence, the *SD*-value has to be scaled accordingly. The mean standard deviation values obtained are listed in Table 6-3.

The standard deviations tend to cluster around the mean value in a Gaussian distribution. Figure 6.25 shows the distribution of standard deviations in the air-brine measurements, i.e. measurements with the 1D profile sequence. The figure shows the distribution calculated for the full bandwidth, the noise and the sand sample. Note that the sand yields the highest SD-values. The low standard deviation values demonstrate the accuracy of NMR, validating the current measurements. Similar distribution behaviours are observed for both oil-brine standard deviations.

Based on these observations, the overall uncertainties of the calculated water saturations in both air-brine and oil-brine systems could be estimated from Equation (5.5). The results are listed in Table 6-3. Since the SNR value is at its lowest after centrifugation at the highest speed, i.e. when the sample contains the least amount of water, this is where the greatest uncertainties of $S_w$ are located. Thus, the uncertainty of $S_w$ is marked in the air-brine $P_c$-curve obtained for the Berea core after centrifugation at 1500 rpm in Figure 6.3. For an oil-brine system, the uncertainties of the water saturation values are depicted in Figure 6.14.

**Table 6-3 Standard deviations and saturation uncertainties**

| Measurement | *SD* | $S_w$ uncertainty |
|---|---|---|
| Air-brine | ± 98.5 | ± 0.010 |
| Oil-brine, $M_{tot}$ | ± 95.9 | ± 0.012 |
| Oil-brine, $M_{oil}$ | ± 154.6 | |

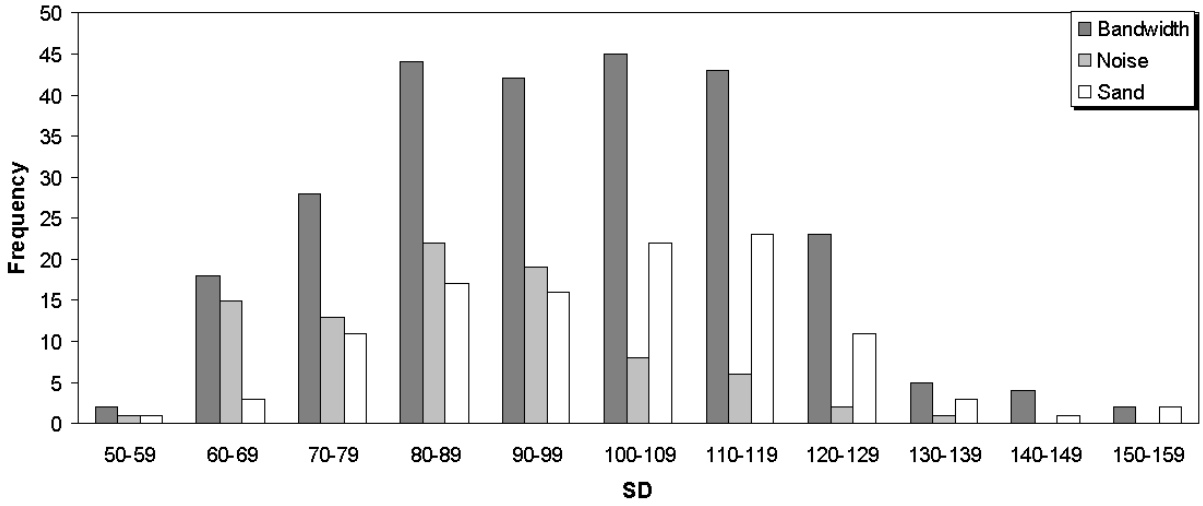


**Figure 6.25** *Standard deviations obtained for air-brine measurements yield a Gaussian distribution.*

### 6.7.2 Evaporation of fluids over time

Early measurements indicated that *water evaporation* could occur during NMR measurements. To investigate the prospect of evaporation, several NMR measurements were performed over longer periods of time at approx. 35 $^{o}$C, and the sample core weights before and after were registered. All surfaces of the core sample were covered with plastic foil when measurements were performed on the Berea sandstone core at two different conditions:

I : 100 % brine saturated

II : After air/brine centrifugation at 750 rpm

The sample core was measured in the NMR instrument with the 1D profile sequence, described in subsection 4.4.1, at both conditions. The weight of the Berea core was measured before and after NMR measurements, $m_{before}$ and $m_{after}$ respectively. The percentage weight loss and measurement times are shown in Table 6-4. A weight loss of 1.4 % is observed for measurements following air-brine centrifugation at 750 rpm, condition *II*. This loss is due to brine evaporation. In condition *I* the weight loss in the Berea sandstone is 0.6 %, despite a much longer measurement period (43 hours and 40 minutes). These results indicate that sample cores with lower brine saturation are exposed to a higher degree of evaporation. It becomes reasonably to expect that if the core is centrifuged at higher rotational speeds, causing lower brine saturations, it would be exposed to an even higher weight loss during NMR measurements.

**Table 6-4** *Water loss experiment data*

| Core condition | I | II |
|---|---|---|
| Time | 43 h 40 min | 23 h |
| $m_{before}$ [g] | 125.38 | 121.02 |
| $m_{after}$ [g] | 124.67 | 119.36 |
| $\Delta m$ [g] | 0.71 | 1.66 |
| Weight loss [%] | 0.57 | 1.37 |

The duration of a typical NMR measurement needed to obtain the primary drainage capillary pressure data is typically within a few minutes. Thus, the amount of evaporated water after 24 hours becomes less relevant for the results of this study.

To illustrate the level of evaporation the first hour of measurements, the area $A$ of the measured intensity profiles was calculated from

$$A = \frac{1}{N} \times \Delta x \sum_i y_i \tag{6.2}$$

where $N$ is the total number of measurements executed, $\Delta x$ is the profile resolution (see subsection 5.2.2) and $y_i$ is the measured intensity in the sample core range. The area $A$ correlates to the total amount of hydrogen present in the core. Figure 6.26 shows the percentage intensity deviation from the first measurement as a function of time for a fully brine-saturated Berea sandstone and the same core after air-brine centrifugation at different rotational speeds. The plot indicates that the sample core is most vulnerable to evaporation after being centrifuged at 1500 rpm, giving a deviation of approximately 3.5%. Consequently, the highest degree of fluid evaporation is when the core contains the least amount of brine. This is when the largest surface area of water is exposed to air due to the fluid distribution within the core.

Note that the plot also claims that there are positive deviation values, i.e. an increase in brine saturation. This is an error caused by noise in the intensity profile. However, it can be seen that the evaporation of brine is insignificant in the time required to acquire the NMR profile, i.e. approximately 2 minutes. The deviation within this time span is estimated to be within ± 1%.

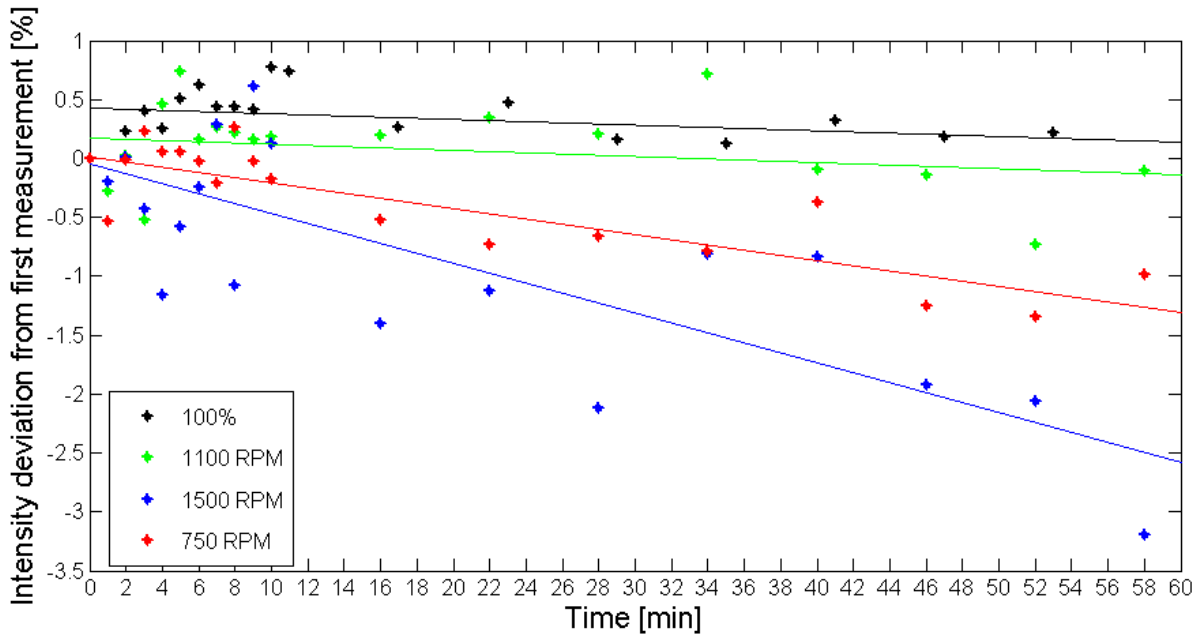


**Figure 6.26** *The intensity deviation from the first measurement as a function of time for a fully brine-saturated (100%) Berea sandstone and the same core after air/brine centrifugation at 750, 1100 and 1500 rpm.*

### 6.7.3 Consistency of fully saturated profiles

The $S_w$-values in this thesis are calculated from Equation (5.4). For each air-brine centrifugation speed, a fully brine saturated profile was measured, $M_0$. In theory, these profiles should remain constant, but experimental errors could influence this. Thus, it is important to place emphasis on *the consistency of the fully saturated measurements*. A change in $M_0$ would result in significant errors in the final capillary pressure curve. A collection of $M_0$ saturation profiles obtained for the L1 core is shown in Figure 6.27, illustrating the error. For a perfectly homogeneous sample core, the fully saturated profile should be flat, i.e. the brine distribution should be constant along the axis of the core. As seen in the figure below, this is not the case for the heterogeneous limestone L1. The $M_0$-profile measured prior to centrifugation at 3000 rpm contains lower signals, an inconsistency, compared to the other profiles. This indicates that the plug is not fully saturated due to experimental errors during the saturation process. Hence, the $M_0$-values are unsuited for calculations of $S_w$ and L1 must be re-saturated. This also indicates that the experimental uncertainties in air-brine procedure I are larger than those in procedure II due to the re-saturation of the core plugs.

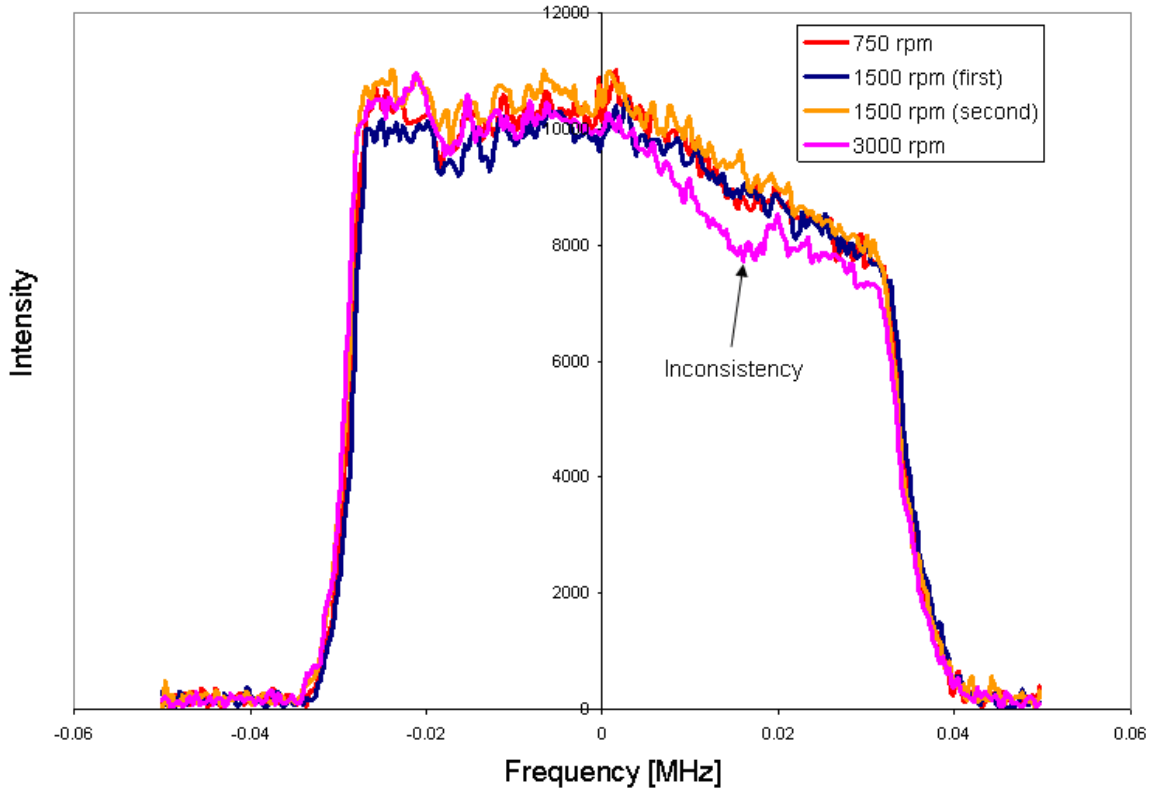


**Figure 6.27** *Comparison of fully brine saturated profiles for the L1 core. The $M_0$-values measured prior to centrifugation at 3000 rpm contains an inconsistency compared to the others.*

### 6.7.4 Consistency of profiles measured after centrifugation

Since L1 was centrifuged twice at 1500 rpm with air and brine, it is possible to do a comparison of the obtained data. This will give an indication of the repeatability of the method. Figure 6.28 shows the measured intensity profiles after each run. Note that the core was re-saturated with brine before each air-brine centrifugation. The profiles show good correlation, except at the left end of the core, the end with the highest brine saturation. Studies indicate that this is the area most vulnerable to fluid redistribution. Hence, the difference in brine saturation can be explained by the transport time. Table B-1 in Appendix B shows that it took close to 10 minutes to transport L1 from the centrifuge to the NMR instrument in the first run, while the transport time was reduced to less than 4 minutes in the second run. Based on the conclusion from subsection 6.7.6, i.e. that some degree of brine redistribution is present after centrifugation in air-brine systems; it is liable to assume that the intensity difference is due to brine redistribution.

As a result of the resemblance in the intensity profiles, the two runs yielded fairly equal capillary pressure curves (see Figure 6.6). Still, it could be argued that the second run is more accurate.

There is a clear consistency in the measured profiles after centrifugation. In accordance with this observation, the repeatability of the method is considered to be good. Nevertheless, it is important to place emphasis on transport time.

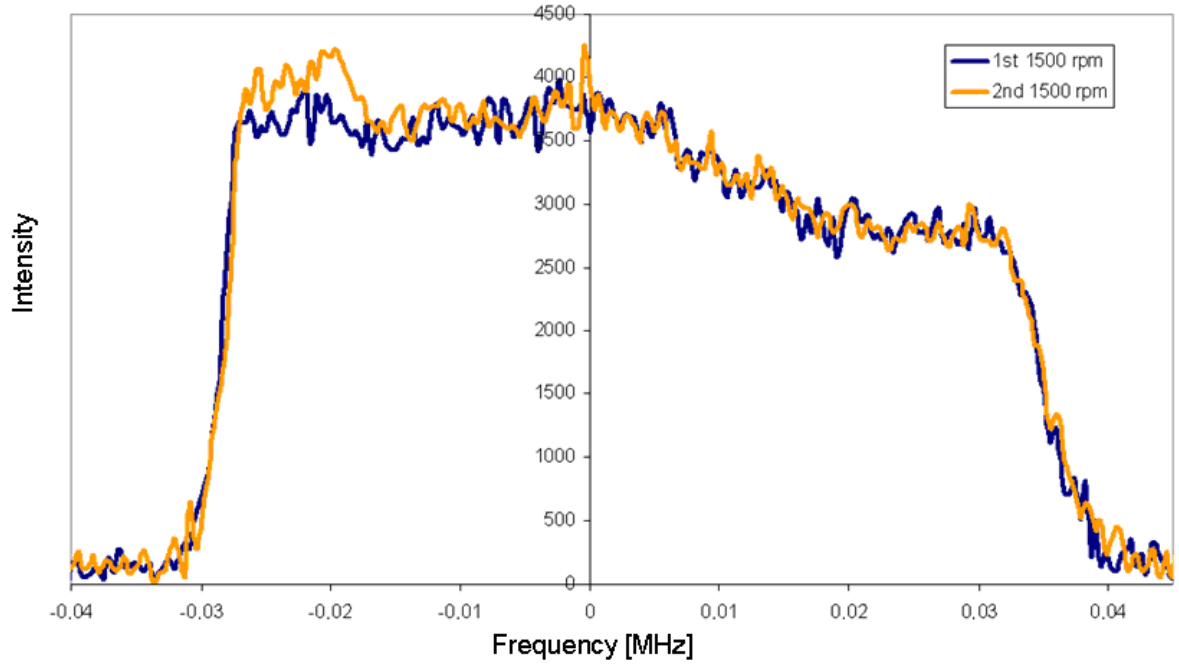


**Figure 6.28** *Comparison of the measured intensity profiles after two centrifugations at 1500 rpm, 1st and 2nd.*

### 6.7.5 Verification of intensity loss

The capillary end effect, as described in section 3.4, is the accumulation of the wetting phase at the outlet end of the core. Although some degree of fluid hold-up is observed, the assumption of 100 % brine saturation at the outlet end is apparently violated in these measurements since there is a reduction in brine saturation at the end of the core sample after centrifugation. In theory, the primary drainage curve starts at 100 % water saturation, i.e. at $S_w$ = 1. Due to the violation, it becomes evident that this is not obtained for any of the studied cores. By using a footbath during centrifugation, this error could have been avoided [8, 88]. However, this lack of upholding the Hassler-Brunner boundary condition has been observed by many authors who measure saturation profiles in connection with centrifuges, including

Wunderlich [29], Al-Omair et al. [89] and Fernø et al. [90], all questioning the validity of the assumption.

It could be argued that the absence of 100 % brine saturation at the outlet end is due to erroneous intensity measurements. Thus, the core sample weights were measured after each air-brine centrifugation speed. These data can be utilized to verify the corresponding intensities measured, $M_a$. The brine volume produced is easily found by subtracting the measured weight after centrifugation from the fully brine saturated core weight, $N_{weight} = m_{100\%} - m_{after}$. The unit of $N_{weight}$ is then changed to ml. In order to create a comparable value, the produced volume is divided by the total pore volume of the core plug, deduced from its dry and saturated weights, $Prod_{weight} = N_{weight} / V_p$.

The area under the intensity curves is the sum of all intensity values for each centrifugation speed. In accordance with the weight calculations, the produced intensity area is found by subtracting the area after centrifugation from the fully saturated intensity area, $N_{intensity} = A_{100\%} - A_{after}$. Then, the amount of produced brine is the ratio of the produced intensity area and the fully saturated area, $Prod_{intensity} = N_{intensity} / A_{100\%}$.

In theory $Prod_{weight} = Prod_{intensity}$, but the columns in Figure 6.29 shows that the difference increases with increasing heterogeneity. For the Berea core, the measured weights confirm the brine production observed in the intensity values. This is also the case for the other core plugs L1, L2 and VC, although small variations are observed. The weights of the sealing plastic plate and the shrink tube are subtracted from all weights measured for VC. The offsets between the amounts of produced fluids could indicate that the measured intensity levels are erroneous, but the difference is rather caused by errors in weight measurements. Overall, the core sample weights verify the measured intensities. Hence the saturation levels at the outlet end of the cores are correct, and the assumption of 100 % water saturation is violated.

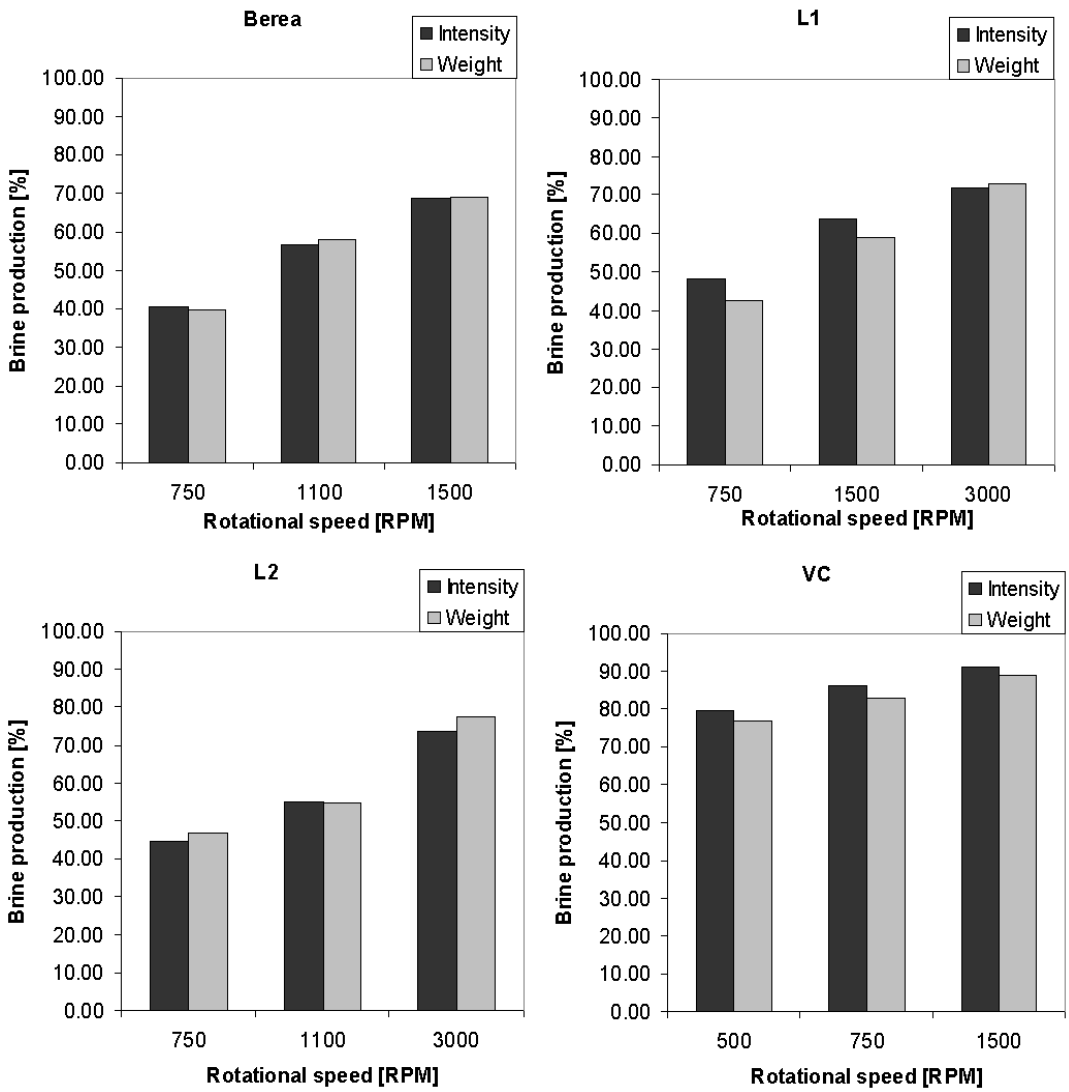


**Figure 6.29** *Comparison of brine production in all core plugs, calculated from intensity loss and weight loss, after centrifugation.*

### 6.7.6 Redistribution of fluids

*Redistribution of fluids* subsequent to centrifuging can affect the capillary pressure calculation if it occurred while the distribution is being measured or during transport. The rate of redistribution is dependent on the rock and the fluids used. Since brine is the wetting fluid, the redistribution process studied is a spontaneous imbibition process. Green et al. [8] found that a decrease in rock permeability showed a lower rate of distribution, i.e. the redistribution of fluids can represent a problem for high permeability rocks. During their studies, they found that redistribution did occur in a Berea sandstone with a permeability of 802.5 mD, while a lower permeability Berea core, similar to the one used in this thesis, showed a much lower rate of distribution. However, other studies claim that the errors introduced by redistribution are undetectable until 1 hour has passed [7]. This was examined for both air-brine and oil-

brine processes in this study. The times of interest in the two processes are the first 10 minutes and the first 20 minutes, respectively.

*Air-brine measurements*

The brine saturated Berea plug, with a permeability of 127.5 mD, was centrifuged with air at 1100 rpm before being measured with the 1D profile sequence. It was emphasized that the transport from the centrifuge to the NMR instrument should be carried out as fast as possible, within the range of 4 minutes. The first 10 minutes of intensity measurements are shown in Figure 6.30. This plot confirms that redistribution of brine takes place early in the measurements, making it likely that it is also present at the transport stage prior to the measurements.

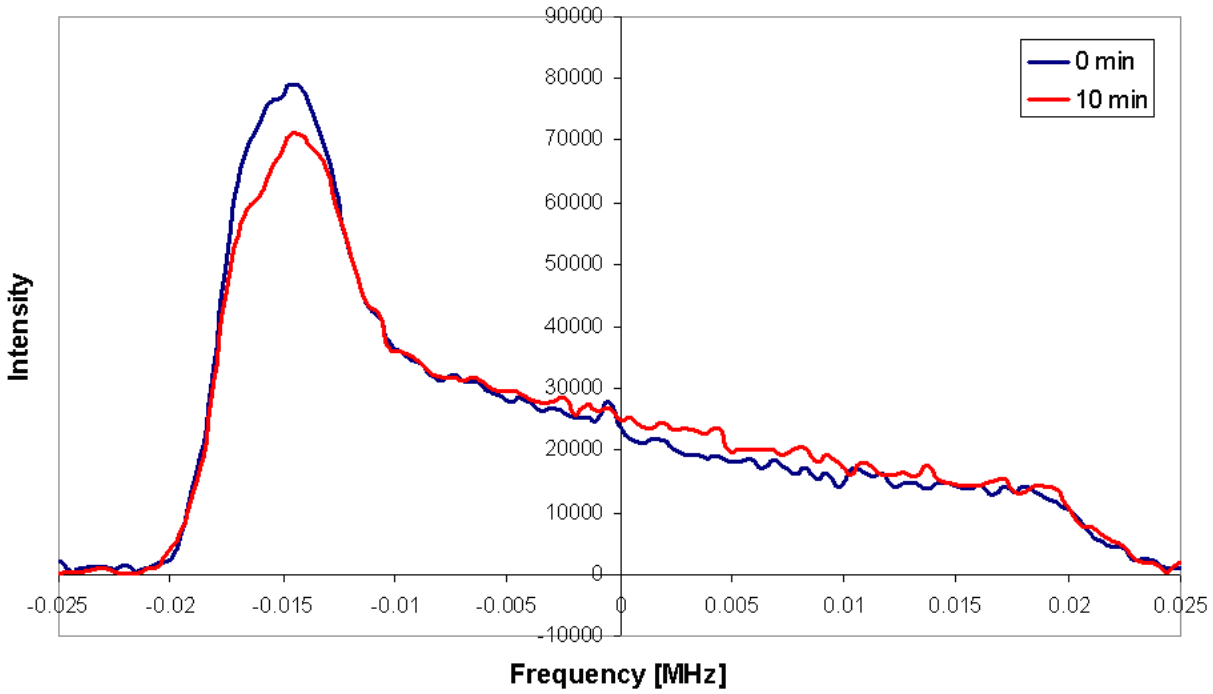


**Figure 6.30** *Brine redistribution in the Berea sandstone after air-brine centrifugation at 1100 rpm.*

To further investigate what effect this redistribution could add to the capillary pressure curve, primary drainage curves were calculated using the measured intensity data at 0 and 10 minutes. Note that this only represents the capillary pressure curve obtained after centrifugation at 1100 rpm. It has already been shown that redistribution is present within the first 10 minutes of measurements, and the capillary pressure curves presented in Figure 6.31 illustrate the effects of this. The main difference between the curves is that there is a decrease in maximum brine saturation with time, i.e. the initial brine saturation is lower after 10

minutes. Higher saturation values are also registered with increasing capillary pressure. This observation, together with the fact that the areas below the curves in Figure 6.30 are equal, confirms that the effect is due to brine redistribution rather than evaporation.

Considering it took 4 minutes to transport the sample core from the centrifuge to the NMR instrument, it is highly likely that the brine saturation distribution, and thus the capillary pressure curve, have changed during transport. It is feasible to conclude that the initial brine saturation decreased during transport, demonstrating the importance of performing this part of the experiment as fast as possible.

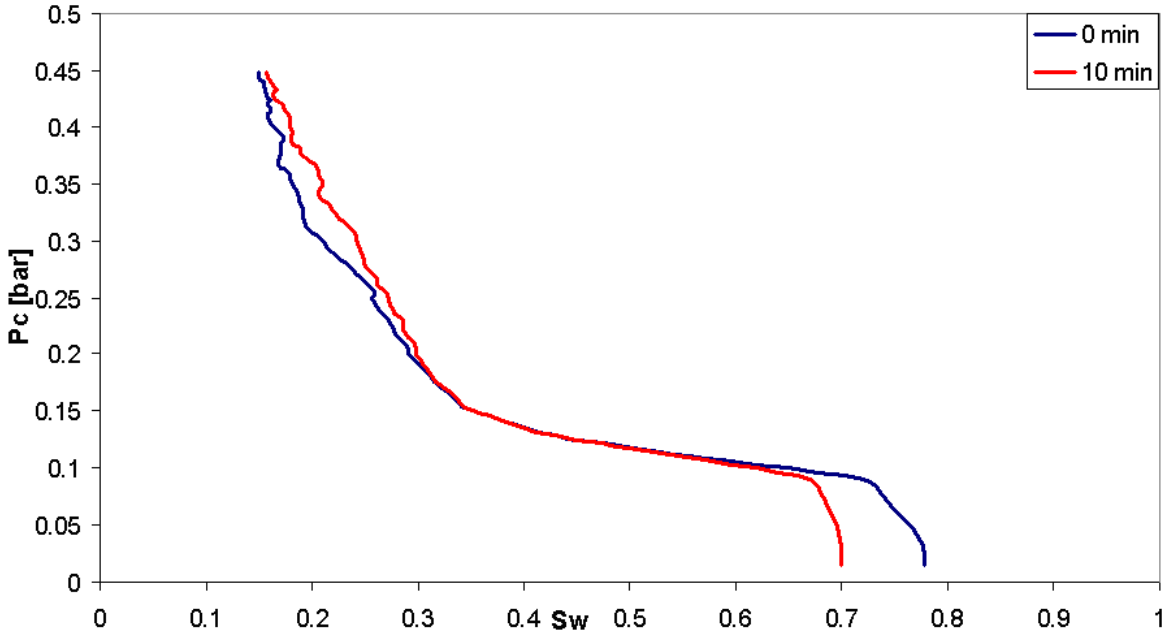


**Figure 6.31** *Capillary pressure curves calculated from intensity data after 0 and 10 minutes of NMR measurements on the centrifuged Berea core.*

In order to test the statement from Green et al. [8], i.e. that the rate of redistribution decreased with decreasing permeability, an analogous approach was used to determine the redistribution in the low permeable limestone L1 ($K$ = 22.0 mD). The brine distribution after centrifugation at 750 rpm is shown in Figure 6.32. Despite the heterogeneity of the curves, it is evident that some redistribution does occur in L1 after 10 minutes, but not to the same extent as in the Berea sandstone. The standard deviations found in subsection 6.7.1 are depicted in the saturation profile to indicate the accuracy of the measurements. As stated earlier in this thesis, the low permeable limestones yield higher capillary pressures than the Berea sandstone due to smaller pore throat radiuses. Despite the high $P_c$-values, the low permeability of the limestone

samples is hindering fluid redistribution [91]. Hence, a lower rate of redistribution is observed in L1 and L2. Although this confirms Greens statement, the effects of fluid redistribution in low permeable rock cores should not be ignored during measurements.

It should be noted that the results from the Berea and L1 used in this subsection are not directly comparable due to differences in NMR system parameters and centrifuge speeds. However, the results in this study indicate that the redistribution of brine is larger after centrifugation at high centrifuge speeds, i.e. when the core contains less brine. Since the L1 intensity data studied here is from centrifugation at 750 rpm, the lowest speed L1 is subjected to, it is most likely that the redistribution of L1 is larger at higher rotational speeds.

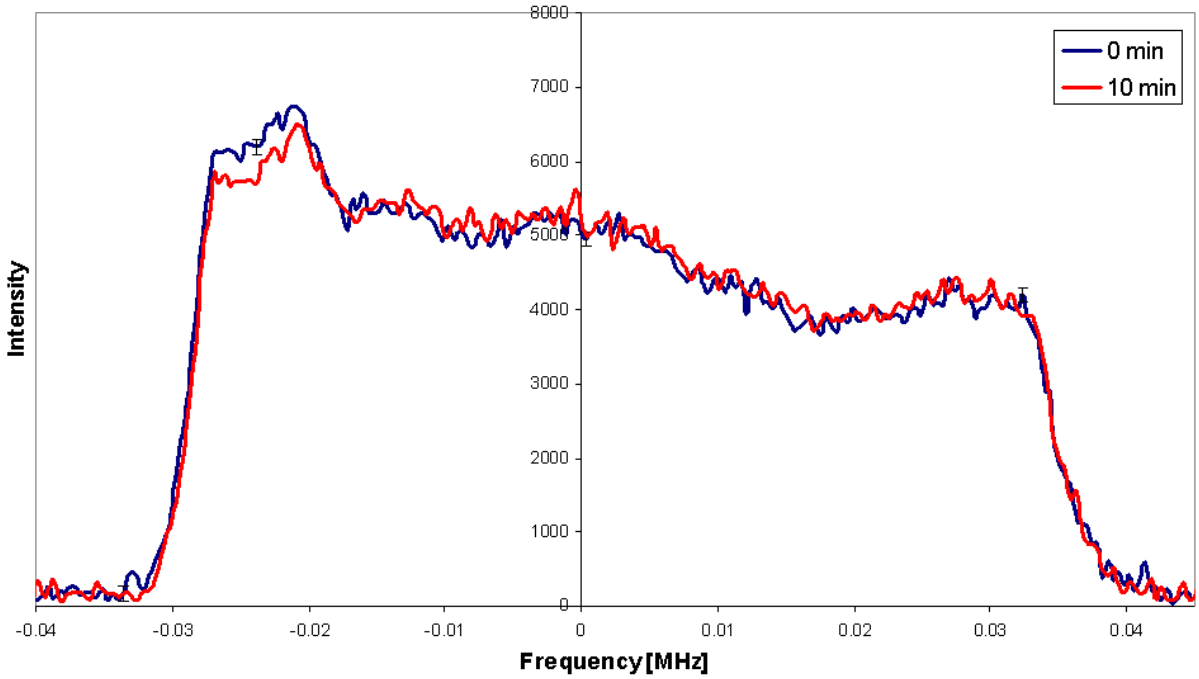


**Figure 6.32** *Brine redistribution in the limestone L1 after centrifugation at 750 rpm.*

*Oil-brine measurements*

In the oil-brine measurements, the stoppage time, i.e. the total amount of time elapsed between each centrifugation speed, is the time of interest. As shown in Table B-2 in Appendix B, this time was kept within a limit of 20 minutes. Hence, this is the amount of time where the fluid redistribution is examined for the oil-brine measurements.

The brine redistribution in the Berea sandstone after oil-brine centrifugation at 1800 rpm is plotted in Figure 6.33. It is evident that redistribution does occur in oil-brine systems, but to a lesser extent than in air-brine systems. This is explained by the low mobility of the oil used, i.e. the highly viscous Marcol 82 is hindering the spontaneous imbibition process [92]. Note that the Berea core yield slightly higher brine intensity values in its right end after 20 minutes, indicating that the brine is redistributed rather than evaporated.

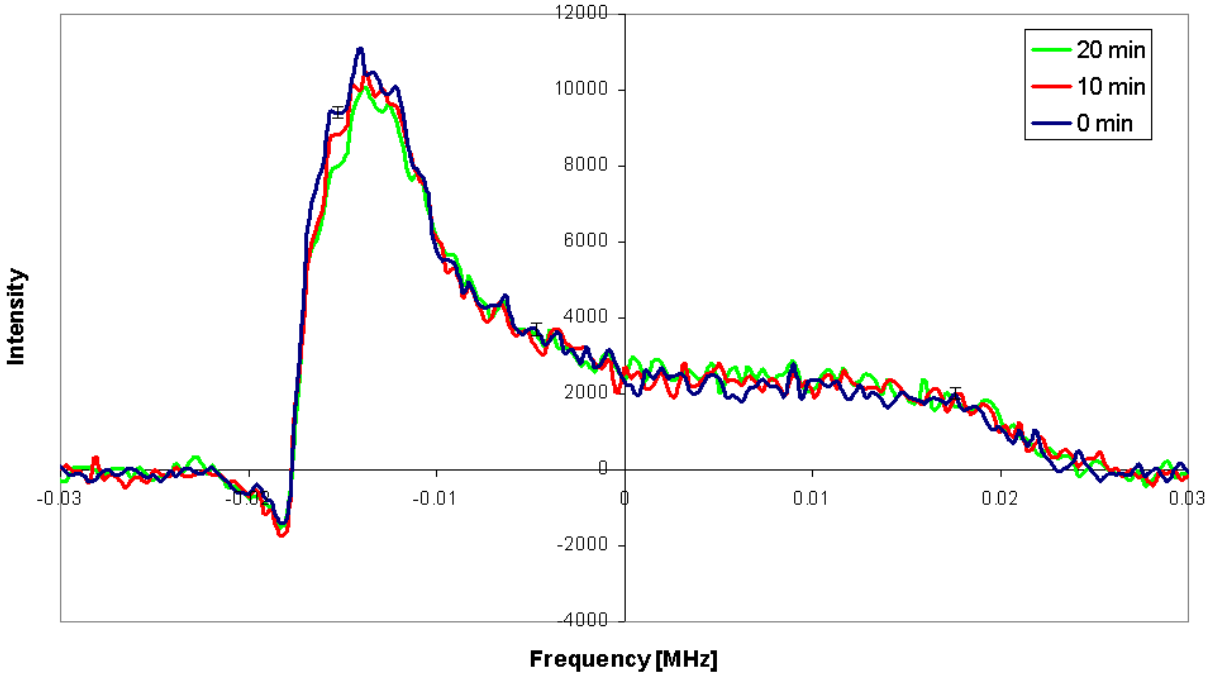


**Figure 6.33** *Brine redistribution in the Berea sandstone after oil-brine centrifugation at 1800 rpm.*

The rate of redistribution in air-brine systems was found to be smaller in cores with low permeability, e.g. L1 and L2. An analogous conclusion can be drawn for oil-brine systems. Figure 6.34 shows the brine redistribution in L1 after oil-brine centrifugation at 4000 rpm. Since the rate of redistribution is found to be low both in oil-brine processes and in limestones, it is considered as negligible in low permeable rocks during 20 minutes. Further studies, not shown, indicate that an effect of redistribution is not observed in the limestones even after 1 hour of measurements.

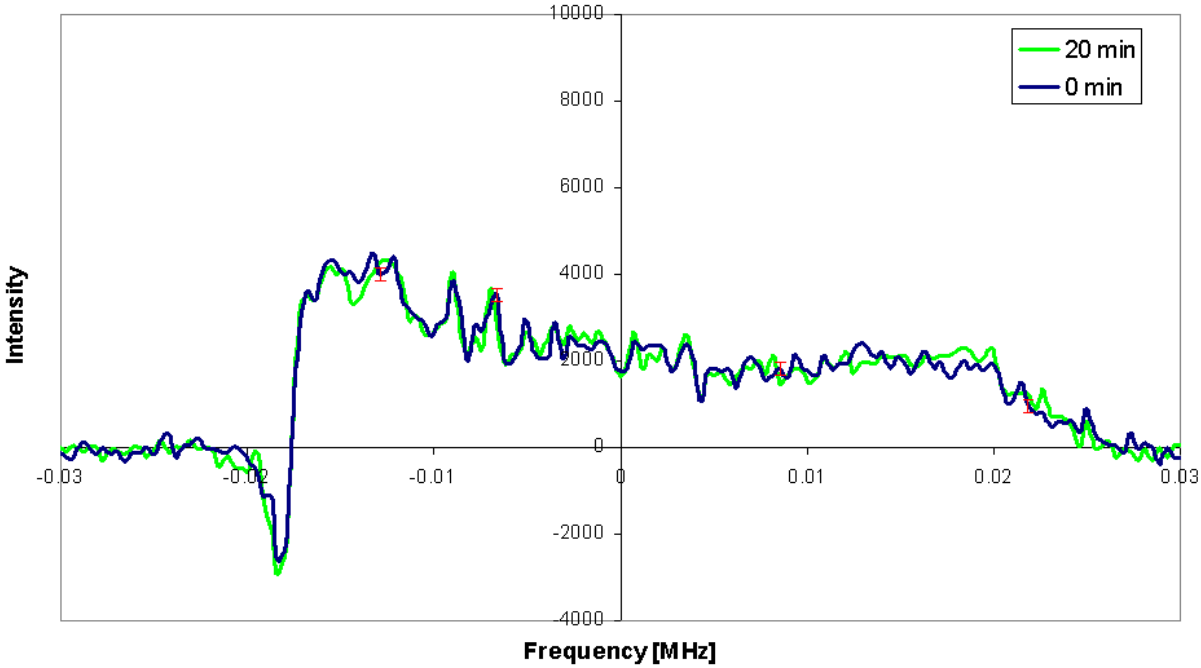


**Figure 6.34** *Brine redistribution in the limestone L1 after oil-brine centrifugation at 4000 rpm.*

After thorough investigation, the overall behaviour of the wetting fluid during redistribution is illustrated in Figure 6.35. The illustration shows the brine saturation at 1) an initial stage, 2) an intermediate stage and 3) a final stage. As indicated in the figure, the brine in the left part of the core sample tends to move towards lower brine saturations, causing an increase in the saturation at the right part of the core. After a significant time the final stage is reached, and the brine saturation is uniform throughout the full length of the core sample.

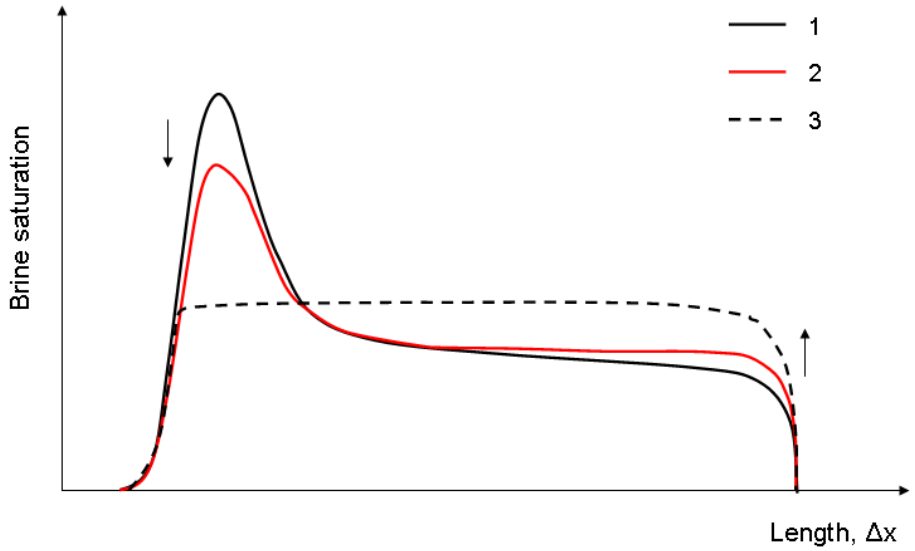


**Figure 6.35** *Illustration of the redistribution of the wetting fluid, i.e. brine, at 1) an initial stage, 2) an intermediate stage and 3) a final stage.*

Oil-brine processes yield lower rates of redistribution, or rates of spontaneous imbibition, than air-brine processes. In addition, it is found that low permeable rocks have lower rates of fluid redistribution than high permeable rocks. Based on these observations, it is concluded that fluid redistribution is present during all air-brine measurements. It is also present in the oil-brine measurements for the Berea core. However, for an oil-brine process, it is neglected in L1 and L2. Note that these results are only representative for the measurement times relevant for this study, i.e. 10 and 20 minutes.

# 7 Conclusions

The primary drainage capillary pressure curve has been measured with a novel method that combines the knowledge of centrifuge experiments and NMR measurements. As opposed to earlier studies, the application of this method has been thoroughly investigated by experimental studies on rock cores ranging in heterogeneity from the relatively homogeneous Berea sandstone to the very heterogeneous vuggy carbonate.

The results demonstrate that the new method is applicable in both air-brine and oil-brine systems. The work presented stands out from previous studies in that it utilizes a diffusion-weighted spin echo profile sequence to discriminate fluid signals from water and oil. By exploiting the significant diffusion coefficient difference between brine and oil, the water signal was suppressed by the use of sufficiently large applied gradients. It should be emphasized that fluids with significantly different diffusion coefficients are required to maintain the applicability of the diffusion-weighted sequence.

It has further been shown that the technique has the capability to establish the capillary pressure-saturation relationship more quickly than traditional techniques, with a total measurement time even below 3 days, depending on the amount of centrifugation speeds needed. Prior to the involvement of oil, an alternative method was tested for the air-brine system. Here, the core plugs were not re-saturated between each rotational speed. This procedure was later implemented for the oil-brine measurements, dramatically decreasing measurement time.

One of the main advantages of the new method is its ability to measure the actual fluid saturations within the sample core. Due to this in-situ measurement, it is unnecessary to perform inaccurate calculations based on the amount of expelled water during centrifugation. In addition, the heterogeneous features within a rock are accounted for, making it a favourable method for investigations of heterogeneous materials.

The resulting capillary pressure curves reflect the heterogeneous nature of the studied core material, providing valuable information for reservoir simulation studies. Accurate NMR measurements were employed to expose internal structures in the rock cores, explaining irregularities observed in the results. In particular, the primary drainage capillary pressure curve obtained for the vuggy material is applicable for dual porosity models since it is found

to represent the fluid distribution of the matrix porosity. $T_2$ distributions for the same material also indicate that the assumption of zero capillary pressure in vugs, as made by numerous studies, is wrong. These observations can provide important information in further studies on the transport properties of vuggy carbonates.

Finally, the method was found to be both reliable and accurate due to the low uncertainty of its measurements. By addressing the experimental errors concerning the new method, it was concluded that the rate of fluid redistribution is a function of the permeability of the studied porous material, i.e. low permeability rocks yield lower rates of redistribution. During the same studies it was observed that redistribution occurs to a lesser extent in oil-brine systems compared to air-brine systems. Thus, it was suggested that the prospect of fluid redistribution could be neglected during oil-brine measurements in low-permeability core samples. By performing NMR measurements over longer periods of time, it was also found that the rate of fluid evaporation is insignificant during all NMR measurements in this thesis work.

# 8 Further work

During the work on this thesis some issues have emerged that would benefit from further attention. For a new method to be widely accepted, it needs to be tested on a large number of samples. A weakness of the data presented here is the limited number of sample cores tested. Testing a larger number of heterogeneous samples would increase the reliability of the method.

The new method aims at providing the capillary pressure-saturation relationship as fast as possible. The main factor contributing to the experimental time is the centrifugation time. Thus, further studies on the equilibrium states during centrifugation are needed in order to reduce the experimental time.

The Hassler Brunner centrifuge method should be performed on the cores used in this thesis. It would be of great interest to compare the resulting capillary pressure curves obtained from the two methods, as this could add strength to the applicability of the new method.

Another potential area of improvement is to expand the application of the method in terms of measuring both imbibition and secondary drainage data.

Based on the results of this thesis, further investigation of the connectivity and capillarity of the vuggy porosity could be conducted. A study of the force needed to drain water situated in connected vugs, expected to be somewhere between the strength of the gravity force and the applied force during rotation at 500 rpm, would provide additional information on the capillarity of vugs.

# 9 References


1. Purcell, W.R., *Capillary Pressures - Their Measurement Using Mercury and the Calculation of Permeability Therefrom.* 1949.
2. McCullough, J.J., F.W. Albaugh, and P.H. Jones, *Determination Of The Interstitial-Water Content Of Oil And Gas Sand By Laboratory Tests Of Core Samples*, in *Drilling and Production Practice*. 1944, American Petroleum Institute.
3. Hassler, G.L. and E. Brunner, *Measurement of Capillary Pressures in Small Core Samples.* Trans. AIME 1945. **160**: p. 114-123.
4. Montaron, B., *Confronting Carbonates.* ADIPEC, 2008.
5. Baldwin, B.A. and W.S. Yamanashi, *Capillary-pressure Determinations From Nmr Images Of Centrifuged Core Plugs: Berea Sandstone.* 1991(LOGANAL).
6. Chen, Q. and B.J. Balcom, *Measurement of Rock-core Capillary Pressure Curves Using a Single-speed Centrifuge and One-dimensional Magnetic-Resonance Imaging.* The Journal of Chemical Physics, 2005. **122**(21): p. 214720.
7. Green, D., et al., *Oil/Water Imbibition and Drainage Capillary Pressure Determined by MRI on a Wide Sampling of Rocks.* SCA08, 2008.
8. Green, D., et al., *Sensitivity Study of Variables Associated with Magnetic Resonance Imaging Capillary Pressure Measurements in Porous Rocks.* 2009.
9. Green, D., et al., *Comparison Study of Capillary Pressure Curves Obtained Using Traditional Centrifuge and Magnetic Resonance Imaging Techniques*, in *SPE/DOE Symposium on Improved Oil Recovery*. 2008, Society of Petroleum Engineers: Tulsa, Oklahoma, USA.
10. Ursin, J.R. and A.B. Zolotukhin, *Introduction to Petroleum Reservoir Engineering*. 2000, Kristiansand: Norwegian Academic Press.
11. Murray, R.C., *Origin of Porosity in Carbonate Rocks.* Journal of Sedimentary Research, 1960. **30**(1): p. 59-84.
12. Lien, J.R., *Reservoarteknikk I*. 2007: University of Bergen.
13. Skarestad, M. and A. Skauge, *Reservoarteknikk II*. 2008: University of Bergen.
14. Anderson, W.G., *Wettability Literature Survey- Part 4: Effects of Wettability on Capillary Pressure.* SPE Journal of Petroleum Technology, 1987. **39**(10): p. 1283-1300.

15. Morrow, N.R., *Physics and Thermodynamics of Capillary Action in Porous Media.* Industrial & Engineering Chemistry, 1970. **62**(6): p. 32-56.
16. Anderson, W., *Wettability Literature Survey- Part 2: Wettability Measurement.* SPE Journal of Petroleum Technology, 1986. **38**(11): p. 1246-1262.
17. Donaldson, E.C., R.D. Thomas, and P.B. Lorenz, *Wettability Determination and Its Effect on Recovery Efficiency.* 1969. **9**(1): p. 13 - 20.
18. Amott, E., *Observations Relating to the Wettability of Porous Rocks.* Trans. AIME, 1959. **216**: p. 156-162.
19. Nichols, G., *Sedimentology and Stratigraphy*. 1999, London: Blackwell Publishing.
20. Churcher, P.L., et al., *Rock Properties of Berea Sandstone, Baker Dolomite, and Indiana Limestone,* in *SPE International Symposium on Oilfield Chemistry*. 1991, 1991 Copyright 1991, Society of Petroleum Engineers Inc.: Anaheim, California.
21. Selley, R.C., *Elements of Petroleum Geology*. Second edition ed. 1998: Academic Press.
22. Lin, C., *Microgeometry II: Testing for homogeneity in Berea sandstone.* Mathematical Geology, 1981. **14**(Number 4 / August, 1982): p. 361-370.
23. Lucia, F.J., *Rock-fabric/Petrophysical Classification of Carbonate Pore Space for Reservoir Characterization.* AAPG Bulletin, 1995. **79**(9): p. 1275-1300.
24. Lucia, F.J., *Petrophysical Parameters Estimated From Visual Descriptions of Carbonate Rocks: A Field Classification of Carbonate Pore Space.* SPE Journal of Petroleum Technology, 1983. **35**(3): p. 629-637.
25. Vik, B., et al., *Characterisation of Vuggy Carbonates,* in *SPE/EAGE Reservoir Characterization and Simulation Conference*. 2007, Society of Petroleum Engineers: Abu Dhabi, UAE.
26. Sabatier, L., *Comparative Study of Drainage Capillary Pressure Measurements Using Different Techniques and for Different Fluid Systems.* SCA-9424, 1994.
27. Sarwaruddin, M., *Modeling of Capillary Pressure Hysteresis Curves by Gamma Absorption Technique*. 2003, Trondheim: NTNU.
28. Chen, Z.A. and D.W. Ruth, *Measurement And Interpretation Of Centrifuge Capillary Pressure Curves-the Sca Survey Data.* 1995(LOGANAL).
29. Wunderlich, R.W., *Imaging of Wetting and Nonwetting Phase Distributions: Application to Centrifuge Capillary Pressure Measurements*, in *SPE Annual Technical Conference and Exhibition*. 1985: Las Vegas, Nevada.

30. Christiansen, R.L. and K.S. Cerise, *Geometric Concerns for Accurate Measurement of Capillary Pressure Relationships With Centrifuge Methods (includes associated paper 27739 ).* SPE Formation Evaluation, 1992. **7**(4): p. 311-314.
31. Forbes, P.L. and Z.A. Chen, *Quantitative Analysis of Radial Effects on Centrifuge Capillary Pressure Curves*. 1994, SPE.
32. Leverett, M.C., *Capillary Behavior in Porous Solids SPE-941152-G*. 1941.
33. Sinnokrot, A.A., H.J. Ramey Jr., and S.S. Marsden Jr., *Effect of Temperature Level upon Capillary Pressure Curves.* 1971. **11**(1): p. 13-22.
34. Søndenå, E., et al., *A Comparison Between Capillary Pressure Data and Saturation Exponent Obtained at Ambient Conditions and at Reservoir Conditions.* SPE Formation Evaluation, 1992. **7**(1): p. 34-40.
35. Ramey, J.H.J., J.S.S. Marsden, and S.K. Sanyal, *The Effect of Temperature on Capillary Pressure Properties of Rocks*, in *SPWLA 14 Annual Logging Symposium*. 1973, Society of Petrophysicists & Well Log Analysts.
36. Mohammad, W., *Effect of Scale on Capillary Pressure Curves of Carbonate Samples*, in *SPE/DOE Improved Oil Recovery Symposium*. 2002, SPE: Tulsa, Oklahoma.
37. Harris, R.K., *Nuclear Magnetic Resonance Spectroscopy*. 1986: Longman Group UK Ltd.
38. Lien, J.R., *En kort innføring i NMR logging.* 2004.
39. Djurhuus, K., *Dynamic NMR and Pore Scale Characteristics.* 2008.
40. Morriss, C., et al., *Core Analysis By Low-field Nmr.* 1997(LOGANAL).
41. Dunn, K.J., D.J. Bergman, and G.A. Latorraca, *NMR, Petrophysical and logging applications*. 2002: Pergamon.
42. Bloch, F., *Nuclear Induction.* Physical Review, 1946. **70**(7-8): p. 460.
43. Meiboom, S. and D. Gill, *Modified Spin-Echo Method for Measuring Nuclear Relaxation Times.* Review of Scientific Instruments, 1958. **29**(8): p. 688-691.
44. Young, H.D. and R.A. Freedman, *University Physics with Modern Physics*. 11 ed. 2004: Pearson Education Inc.
45. Watson, A.T. and C.T.P. Chang, *Characterizing Porous Media with NMR Methods.* Progress in Nuclear Magnetic Resonance Spectroscopy, 1997. **31**(4): p. 343-386.
46. Carr, H.Y. and E.M. Purcell, *Effects of Diffusion on Free Precession in Nuclear Magnetic Resonance Experiments.* Physical Review, 1954. **94**(3): p. 630.
47. Hahn, E.L., *Spin Echoes.* Physical Review, 1950. **80**(Copyright (C) 2009 The American Physical Society): p. 580.

48. Mills, R., *Self-diffusion in Normal and Heavy Water in the Range 1-45 deg.* The Journal of Physical Chemistry, 1973. **77**(5): p. 685-688.
49. Mitra, P.P., P.N. Sen, and L.M. Schwartz, *Short-time Behavior of the Diffusion Coefficient as a Geometrical Probe of Porous Media.* Physical Review B, 1993. **47**(14): p. 8565.
50. Price, W.S., *Pulsed-field Gradient Nuclear Magnetic Resonance As a Tool for Studying Translational Diffusion, Part 1: Basic Theory.* Magn. Reson.: Educ. J., 1997. **9**(5): p. 299-336.
51. Stejskal, E.O. and J.E. Tanner, *Spin Diffusion Measurements: Spin Echoes in the Presence of a Time-Dependent Field Gradient.* The Journal of Chemical Physics, 1965. **42**(1): p. 288-292.
52. Cotts, R.M., et al., *Pulsed Field Gradient Stimulated Echo Methods for Improved NMR Diffusion Measurements in Heterogeneous Systems.* Journal of Magnetic Resonance, 1989. **83**(2): p. 252-266.
53. Sørland, G.H., D. Aksnes, and L. Gjerdåker, *A Pulsed Field Gradient Spin-Echo Method for Diffusion Measurements in the Presence of Internal Gradients.* Journal of Magnetic Resonance, 1999. **137**(2): p. 397-401.
54. Baldwin, B.A. and W.S. Yamanashi, *Detecting Fluid Movement and Isolation in Reservoir Core With Medical NMR Imaging Techniques.* SPE Reservoir Engineering, 1989. **4**(2): p. 207-212.
55. Chen, J.-D., et al., *Magnetic Resonance Imaging of Immiscible-Fluid Displacement in Porous Media.* Physical Review Letters, 1988. **61**(The American Physical Society): p. 1489.
56. Kleinberg, R.L., W.E. Kenyon, and P.P. Mitra, *Mechanism of NMR Relaxation of Fluids in Rock.* Journal of Magnetic Resonance, Series A, 1994. **108**(2): p. 206-214.
57. Brownstein, K.R. and C.E. Tarr, *Importance of Classical Diffusion in NMR Studies of Water in Biological Cells.* Physical Review A, 1979. **19**(6): p. 2446.
58. Coates, G.R., et al., *The MRIL in Conocco 33-1 An Investigation of a New Magnetic Resonance Imaging Log* in *SPWLA 32 Annual Logging Symposium*. 1991, Society of Petrophysicists & Well Log Analysts.
59. Benson, T., *MARAN Ultra Non Expert User Manual*. Vol. 1.6.2. 2003: Resonance Instruments Ltd
60. Sørland, G., et al., *Exploring the Separate NMR Responses from Crude Oil and Water in Rock Cores.* Applied Magnetic Resonance, 2004. **26**(3): p. 417-425.

61. ExxonMobil. *Marcol 82 - Medicinal Grade White Oil*. 2006; Available from: http://www.exxonmobil.com/UK-English/Specialties/PDS/GLXXENSPCEMMarcol_82.asp#IndustrySpecsTitle.
62. Gant, P.L. and W.G. Anderson, *Core Cleaning for Restoration of Native Wettability.* SPE Formation Evaluation, 1988. **3**(1): p. 131-138.
63. Anderson, W.G., *Wettability Literature Survey- Part 1: Rock/Oil/Brine Interactions and the Effects of Core Handling on Wettability.* SPE Journal of Petroleum Technology, 1986. **38**(10): p. 1125-1144.
64. Masalmeh, S.K. and X. Jing, *Improved Characterisation and Modelling of Carbonate Reservoirs for Predicting Waterflood Performance*, in *International Petroleum Technology Conference*. 2007, International Petroleum Technology Conference: Dubai, U.A.E.
65. Khilar, K.C. and H.S. Fogler, *The Existence of a Critical Salt Concentration for Particle Release.* Journal of Colloid and Interface Science, 1984. **101**(1): p. 214-224.
66. *Centrifugation with Water/oil on 1.5" Samples in Ultracentrifuge*. Procedures for core analysis. 1990, Norsk Hydro.
67. Slobod, R.L., A. Chambers, and W.L.P. Jr., *Use of Centrifuge for Determining Connate Water, Residual Oil, and Capillary Pressure Curves of Small Core Samples.* 1951.
68. Omoregle, Z.S., *Factors Affecting the Equivalency of Different Capillary Pressure Measurement Techniques.* SPE Formation Evaluation, 1988. **3**(1): p. 146-155.
69. *Phys114 Kompendium: Grunnleggende målevitenskap*. 2007: University of Bergen, IFT.
70. Vik, B., *Unpublished Work.* 2010.
71. Morrow, N.R., *Irreducible Wetting-phase Saturations in Porous Media.* Chemical Engineering Science, 1970. **25**(11): p. 1799-1815.
72. O'Meara Jr., D.J., G.J. Hirasaki, and J.A. Rohan, *Centrifuge Measurements of Capillary Pressure: Part 1-Outflow Boundary Condition.* SPE Reservoir Engineering, 1992. **7**(1): p. 133-142.
73. Jensen J. L., L.L.W., Corbett W. M, Goggin D. J., *Statistics for Petroleum Engineers and Geoscientists*. 2nd ed. 2000, Amsterdam: Elsevier. 127-130.
74. Corbett P., A.S., Bowen D., *The Use of the Probe Permeameter in Carbonates - Addressing the Problems of Permeability Support and Stationarity.* The Log Analyst 1999. **40**(5).

75. Ferrand, L.A. and M.A. Celia, *The Effect of Heterogeneity on the Drainage Capillary Pressure-Saturation Relation.* Water Resour. Res., 1992. **28**(3): p. 859-870.
76. Sylte, A., et al., *Relative Permeability and Capillary Pressure: Effects of Rock Heterogeneity.* SCA-9808, 1998.
77. Ababou, R., et al., *Numerical Simulation of Three-dimensional Saturated Flow in Randomly Heterogeneous Porous Media.* Transport in Porous Media, 1989. **4**(6): p. 549-565.
78. Dehghani, K., K.A. Edwards, and P.M. Harris, *Modeling of Waterflood in a Vuggy Carbonate Reservoir*, in *SPE Annual Technical Conference and Exhibition*. 1997, SPE: San Antonio, Texas.
79. Ioannidis, M.A. and I. Chatzis, *A Dual-Network Model of Pore Structure for Vuggy Carbonates.* SCA, 2000.
80. Olsen, D., et al., *Quantitative 1D Saturation Profiles on Chalk by NMR.* Magnetic Resonance Imaging, 1996. **14**(7-8): p. 847-851.
81. Bye, A.L., et al., *Residual Gas Distribution in Vuggy Carbonate by use of X-ray CT, NMR and Cryo-esem.* SCA, 2008.
82. Hidajat, I., et al., *Study of Vuggy Carbonates Using NMR and X-Ray CT Scanning.* SPE Reservoir Evaluation & Engineering, 2004. **7**(5): p. 365-377.
83. Vik, B., et al., *Characterization of Vuggy Carbonate by Miscible Processes.* SCA, 2008.
84. Firoozabadi, A. and L.K. Thomas, *Sixth SPE Comparative Solution Project: Dual-Porosity Simulators.* SPE Journal of Petroleum Technology, 1990. **42**(6): p. 710-715, 762-763.
85. Gilman, J.R. and H. Kazemi, *Improvements in Simulation of Naturally Fractured Reservoirs.* 1983. **23**(4): p. 695-707.
86. Moctezuma, A., et al., *A Dual Network Model for Relative Permeability of Bimodal Rocks: Application in a Vuggy Carbonate.* SCA, 2003.
87. Moctezuma-Berthier, A., O. Vizika, and P. Adler, *Water-oil Relative Permeability in Vugular Porous Media: Experiments and Simulations.* SCA, 2002.
88. Bil, K.J., *The Use of Footbaths in Centrifuge Capillary Pressure Curve Measurements.* SCA, 1992.
89. Al-Omair, O.A. and R.L. Christiansen, *Measurement of Capillary Pressure by Direct Visualization of a Centrifuge Experiment.* SCA 9838, 1998.

90. Fernø, M., et al., *Capillary Pressures by Fluid Saturation Profile Measurements During Centrifuge Rotation.* Transport in Porous Media, 2009. **80**(2): p. 253-267.
91. Handy, L.L., *Determination of Effective Capillary Pressures for Porous Media from Imbibition Data.* 1960.
92. Morrow, N.R. and G. Mason, *Recovery of Oil by Spontaneous Imbibition.* Current Opinion in Colloid & Interface Science, 2001. **6**(4): p. 321-337.

# 10 Appendix A Fluid properties

**Table A-1** *Composition of synthetic salt water.*

| Component | Concentration [g/Kg] |
|---|---|
| NaCl | 24.89 |
| $CaCl_2 \cdot 2H_2O$ | 1.726 |
| $MgCl_2 \cdot 6H_2O$ | 11.124 |
| $NaHCO_3$ | 0.192 |
| $Na_2SO_4$ | 4.056 |
| KCl | 0.668 |
| Total | 42.656 |

**Table A-2** *Properties of Marcol 82.*

| Property | Min | Max |
|---|---|---|
| Appearance | Clear and bright | Clear and bright |
| Odour | Absent | Absent |
| Viscosity at 20 $^oC$ [cP] | 27 | 38 |
| Density at 20 $^oC$ [$Kg/m^3$] | 842 | 855 |

# 11 Appendix B Experimental durations

**Table B-1** *Experimental durations, air-brine measurements.*

| Core | Rotational speed ω [rpm] | Time in centrifuge | Transport time |
|---|---|---|---|
| Berea | 1500 | 27 h 45 min | 7 min 58 s |
| | 1100 | 22 h 00 min | 3 min 46 s |
| | 750 | 22 h 41 min | 5 min 22 s |
| Berea (Alternative method) | | | |
| | 1500 | 24 h 32 min | 3 min 19 s |
| | 750 | 24 h 08 min | 3 min 38 s |
| L1 | 3000 | 24 h 41 min | 3 min 51 s |
| | 1500 (first) | 27 h 10 min | 9 min 50 s |
| | 1500 (second) | 23 h 47 min | 3 min 30 s |
| | 750 | 26 h 48 min | 3 min 02 s |
| L2 | 3000 | 26 h 37 min | 2 min 59 s |
| | 1100 | 29 h 17 min | 2 min 50 s |
| | 750 | 43 h 06 min | 2 min 49 s |
| VC | 1500 | 25 h 03 min | 3 min 18 s |
| | 750 | 24 h 23 min | 4 min 05 s |
| | 500 | 25 h 11 min | 3 min 46 s |

**Table B-2** *Experimental durations, oil-brine measurements.*

| Core | Rotational speed ω [rpm] | Time in centrifuge | Transport time | Stoppage time |
|---|---|---|---|---|
| Berea | 1800 | 24 h 03 min | 4 min 46 s | |
| | 1500 | 24 h 12 min | 4 min 08 s | 18 min 25 s |
| | 1100 | 24 h 05 min | 4 min 05 s | 19 min 42 s |
| | 750 | 25 h 02 min | 4 min 15 s | 20 min 15 s |
| L1 | 4000 | 25 h 04 min | 4 min 10 s | |
| | 3000 | 42 h 04 min | 4 min 40 s | 19 min 05 s |
| | 1100 | 24 h 01 min | 4 min 20 s | 17 min 25 s |
| | 750 | 24 h 04 min | 4 min 50 s | 20 min 01 s |
| L2 | 4000 | 24 h 01 min | 4 min 04 s | |
| | 3000 | 24 h 13 min | 4 min 16 s | 17 min 45 s |
| | 2000 | 24 h 01 min | 4 min 15 s | 16 min 26 s |
| | 1100 | 24 h 25 min | 4 min 05 s | 17 min 15 s |
| | 750 | 24 h 15 min | 4 min 15 s | 16 min 26 s |

# 12 Appendix C NMR system parameters

**Table C-1** *NMR system parameters.*

| Parameter | ***Air-brine*** | | ***Oil-brine*** | | ***CPMG*** |
|---|---|---|---|---|---|
| | Berea | Carbonates | All | All | All |
| Measurements | $M_0$, $M_a$ | $M_0$, $M_a$ | $M_{tot}$ | $M_{oil}$ | |
| Frequency [Hz] | 12187091 | 12185475.6 | 12185347 | 12185514 | |
| P90 [µs] | 6.2E-06 | 6.1E-06 | 6.1E-06 | 6.1E-06 | |
| P180 [µs] | 1.24E-05 | 1.22E-05 | 1.22E-05 | 1.22E-05 | |
| RD [µs] | 5 | 5 | 5 | 5 | 5 |
| TAU [µs] | 0.0015 | 0.0029 | 0.0016 | 0.0016 | 0.0010 |
| SI | 2048 | 256 | 256 | 256 | 1 |
| NECH | 14 | 14 | 1 | 1 | 8192 |
| NS | 4 | 4 | 4 | 4 | 4 |
| GX | 32767 | 32767 | 16000 | 16000 | |
| GY | 32767 | 32767 | 32767 | 32767 | |
| GZ | 32767 | 32767 | 16000 | 16000 | |
| G1 | 500 | 550 | 1000 | 25000 | |
| G2 | 260 | 415 | -1000 | -25000 | |
| G3 | 0 | 0 | 50 | 50 | |
| G4 | -1000 | -1000 | 50 | 50 | |
| G5 | 1000 | 1000 | 720 | 635 | |
| G6 | 0 | 0 | 540 | 518 | |
| G7 | 0 | 0 | 0 | 0 | |
| G8 | 0 | 0 | 5000 | 5000 | |
| G9 | 0 | 0 | -8000 | -8000 | |

**Descriptions:**

| | |
|---|---|
| *P*90 | $90^o$ pulse length |
| *P*180 | $180^o$ pulse length |
| *RD* | Relaxation delay |
| *TAU* | Time between successive rephasing pulses |
| *SI* | Number of data points acquired following the pulse |
| *NECH* | Number of echoes |
| *NS* | Number of scans |
| G | Gradient input strength |